The NIR isophotal Tully-Fisher relation and its cosmological applications in the Zone of Avoidance

Khaled Said

Aug 2013

A dissertation submitted in partial fulfilment of the requirements for the degree M.Sc. in the Department of Astronomy, as part of the National Astrophysics and Space Science Programme
UNIVERSITY OF CAPE TOWN

Supervisors: Prof. R C Kraan-Korteweg and T H Jarrett

Abstract

This thesis presents the calibration of the Near-InfraRed (NIR) isophotal Tully – Fisher relation and its cosmological applications in the Zone of Avoidance. Dust extinction and stellar confusion by the Milky Way reduce the efficiency of detection of galaxies at low Galactic latitude, creating the so-called Zone of Avoidance (ZoA). This stands as a stumbling block to our understanding of the local dynamics, cosmic flow fields and the origin of the CMB dipole. The ZoA ($|b| \lesssim 5°$) is excluded from the whole-sky Two Micron All-Sky Survey (2MASS) Redshift Survey (2MRS) and 2MASS Tully-Fisher Survey (2MTF). Correspondingly, knowledge about the density distribution in the ZoA remains limited to statistical interpolations.

We present the recalibration of the isophotal Tully-Fisher relation in the (NIR) J, H, and K_s-bands for the same calibration sample as the 2MTF for the total TF relation. Both TF relations exhibit similar scatter because the calibration sample is not affected by foreground extinction closer to the plane of the Milky Way. However, the application of the isophotal TF relation to low surface brightness galaxies or dust-obscured galaxies results in a vast improvement in the scatter.

We simulate the effect of dust extinction on the geometrical properties of galaxies. Simulations show that galaxies appear rounder with increasing obscuration level. Preliminary correction models are derived based on simulated and real data.

The newly calibrated isophotal TF relations in the J, H, and K_s-bands are used to derive preliminary peculiar velocities of galaxies within the southern ZoA. A significant improvement in the scatter is obtained, compared to the application of the "total" TF relation. The large offset toward the positive peculiar velocity derived from the "total" TF relation disappears when the "isophotal" TF relation is applied. Our preliminary results of the local universe show clear infall into the Great Attractor (GA). The backside infall toward the GA and the infall into the much more remote Shapley Concentration (SC) cannot be quantified with the existing limit ($v_{hel} \leq 6000$ km/s) of our data set. To improve on this situation, we have started to extend our sample to $v_{obs} \leq 9000$ km/s.

Acknowledgments

I would like to acknowledge my supervisors, Prof. Renée C. Kraan-Korteweg and Prof. Tom Jarrett, for their help and support throughout my thesis. Actually, I am lucky to have had such generous supervisors that a few brief sentences do not do them justice. So here is my big **thanks**.

I would like also to acknowledge many collaborators for their help and guidance, including Dr. Maciej Bilicki and Tom Mutabazi at UCT; Wendy Williams at Leiden University; Mpati Ramatsoku at Groningen; Prof. Lister Stavely-Smith and Dr. Chris Springob at ICRAR. Special acknowledgement goes to Dr. Anja Schröder for reading my drafts and adding to the depth of this thesis. I would like also to thank Karen Masters for making the data for the 2MTF calibration available for us to use. I acknowledge the HIZOA survey team for early access to the data.

I am also grateful to my colleagues and astronomers and staff in the Astronomy Department at UCT for making this so great environment for work. In particular, to Louise Steward for her many hours of reading my final draft.

Finally, I would like to thank my family. A special thank to my parents for their constant encouragement and support. Thank you both for making it possible for me to live my childhood dreams and get to this point.

This work is based upon research supported by the South African National Research Foundation and Department of Science and Technology. This thesis makes use of data products from the Two Micron All Sky Survey, which is a joint project of the University of Massachusetts and the Infrared Processing and Analysis Center, funded by the National Aeronautics and Space Administration and the National Science Foundation.

Plagiarism Declaration

I, Khaled Said, know the meaning of plagiarism and declare that all of the work in the document, save for that which is properly acknowledged, is my own.

Contents

List of Figures

List of Tables

Chapter 1

Introduction

Galaxies are not uniformly distributed in space. They instead tend to accumulate along over dense regions such as clusters, walls and filaments, and surround low dense regions called voids. Because the only force that operates on this scale is gravity, gravitational instabilities progressively build up the Large-Scale Structure (LSS) under the influence of gravity. A proper census of this cosmic web of galaxies consists of the positions, luminosities and velocities of the individual galaxies. Velocities of galaxies can be decomposed into two components: (1) a recession velocity due to the uniform expansion of the universe and (2) a peculiar velocity caused by density inhomogeneities. The peculiar velocity (its radial component) is measured as the difference between the observed recession velocity of a galaxy and its Hubble velocity. Because they arise as a result of gravity, peculiar velocities can be used as tracers of the matter distribution, both luminous and dark.

The major stumbling block to mapping the cosmic web arises from the nearest galaxy itself, the Milky Way. The Milky Way obscures the background extragalactic sky through dust extinction (notably within ± 5 degrees of the Galactic Plane) and stellar confusion. This results in the so-called the "Zone of Avoidance" (ZoA), literally meaning that the region is devoid of galaxies, and accordingly, extragalactic astronomers avoid working in this region of the sky. This has led to a gap in our understanding of the dynamics of the Local Group (LG), cosmic flow fields, and the origin of the observed dipole in the Cosmic Microwave Background (CMB) (Lahav 1994; Kraan-Korteweg & Lahav 2000; Kraan-Korteweg 2005; Loeb & Narayan 2008). For cosmological applications, different methods have been employed to interpolate across this part of the sky (e.g. Lahav et al. 1994; Kolatt et al. 1995). This may be valid for the conspicuous features that cross the ZoA, such as the Great Attractor (GA), the Perseus-Pisces Supercluster (PP), the Puppis Cluster or the Local Void (LV). However, more recent ZoA surveys reveal large-scale structures that were not anticipated, highlighting the importance of the ZoA to our overall understanding of the dynamic cosmic web.

Systematic blind HI surveys in the southern ZoA (Henning et al. 2000; Kraan-Korteweg 2005) and recent pointed HI surveys in the northern ZoA (Ramatsoku 2012) have partly improved the situation. These radio surveys provide an elegant way to study the ZoA because at these wavelengths, the obscuring effects of gas and dust from the Milky Way are minimal.

In this thesis we derive the "isophotal" Tully-Fisher template relations in the NIR J, H, and K_s-bands. These relations are used with the available HI and NIR data to carry out a reliable peculiar velocity survey in the Zone of Avoidance.

This introductory chapter is organized as follows: Section 1.1 gives a general background about the ZoA and the effect of the foreground dust extinction and stellar density. Section 1.2 describes the extent of the Zone of Avoidance at different wavebands. In Section 1.3, I discuss the effect of the ZoA on cosmological studies. Section 1.4 describes two of the main redshift surveys in the ZoA so far. Section 1.5 demonstrates the advantages of applying the Tully-Fisher survey in the ZoA. Here I show the necessity of this approach in studying the ZoA, and how it will contribute to the whole-sky survey.

1.1 The Zone of Avoidance

Back in the 19th century, Proctor may well have been the first to notice the lack of nebulae at low Galactic latitude (Proctor 1878) in the distribution of nebulae in the General Catalogue of Nebulae by Herschel (1864). This Zone of few Nebulae is shown in starker contrast in the work by Charlier (1922) using the New General Catalogue by Dreyer (1888). At that time, due to the Great Debate between Harlow Shapley and Heber Curtis about the scale of the Universe (Shapley & Curtis 1921), no connection was made between the Zone of few nebulae and the Milky Way. Only after Hubble's discovery that these nebulae were extragalactic sources (Hubble 1925; 1929), and the discovery of the absorption of light by dust (Trumpler 1930), was it accepted that this lack of nebulae at low Galactic latitude was caused by the foreground dust in the Milky Way (Hubble 1936). Shapley (1961) defined the ZoA as the region limited by "the isopleth of five galaxies per square degree from the Lick and Harvard surveys". Either a lack of data or low-quality images for a few galaxies observed in the ZoA, create a large gap in the whole-sky maps of galaxy distribution.

The extent of the Zone of Avoidance is wavelength-dependent. Dust extinction is the main hindrance at optical wavelengths, rendering more than 20% of the sky incomplete. Stellar confusion is the primary limitation for infrared surveys, affecting some 10% of the sky, because at these wavelengths the dust is more transparent, while luminous giant stars from the Milky Way dominate the emission in these bands (Kraan-Korteweg & Lahav 2000). Systematic HI surveys do not suffer from these effects, and the Milky Way is completely transparent to the emission of the 21 cm line of the gas-rich galaxies (Kraan-Korteweg &

Lahav 2000). Because of the relevance of these effects to our study of galaxies in the ZoA, the physics behind the effects of dust extinction and stellar confusion is discussed in the following two sections (Sec. 1.1.1 & 1.1.2).

1.1.1 Galactic extinction

Interstellar dust in the Milky Way scatters and absorbs star light, causing galaxies behind it to appear smaller and fainter. This process of obscuration, referred to as foreground dust extinction, is wavelength-dependent and decreases towards longer wavelengths. Furthermore, since the extinction is more prominent at shorter wavelengths, objects lying behind the Milky Way appear redder than their intrinsic colour. Understanding the effect of this imposing selective extinction, thus minimizing the deleterious effects on galaxies seen through the Milky Way, is crucial for many cosmological applications.

Cameron (1990) used a sample of large elliptical and spiral galaxies at high Galactic latitude in the optical wavebands to quantify this effect by artificially obscuring those selected galaxies. A similar method was used in a later study by Riad, Kraan-Korteweg, & Woudt (2010) which focus on the Near-Infrared (NIR) J, H, and K_s-bands properties of galaxies viewed through the ZoA. The NIR is able to penetrate through more dust extinction and is thus a better tracer of extragalactic emission. Cardelli, Clayton, & Mathis (1989) quantify the extinction in the J, H, and K_s-bands to be 21%, 13%, and 9% of the extinction in the optical B-band, respectively.

The extinction at a given wavelength can be calculated as the ratio of total to selective extinction,

$$R_V = \frac{A_V}{E(B-V)} \tag{1.1}$$

where the value of R_λ depends on wavelength and the environment along the line-of-sight to the observed galaxy. According to Cardelli et al. (1989), the standard value of R_V for the diffuse interstellar medium is ~ 3.1, although higher values have been reported for colder and denser Galactic molecular clouds. Using the extinction law of Cardelli et al. (1989), Schlegel, Finkbeiner, & Davis (1998) calculate the extinction in the J, H, and K_s-bands to be:

$$A_J = 0.902E(B-V), \tag{1.2a}$$
$$A_H = 0.576E(B-V), \tag{1.2b}$$
$$A_K = 0.367E(B-V). \tag{1.2c}$$

Deriving Galactic extinction from Eqn. 1.2 requires knowledge of dust obscuration on fine enough angular scales to account for the patchy obscuration along the line of sight. The extinction maps by Burstein & Heiles (1982) on scales of ~ 30 arcmin were used for many years as the first indication of foreground dust for $|b| \gtrsim 10°$. More recent work from Schlegel et al. (1998) utilized far-infrared observations from IRAS and COBE to estimate the column of dust obscuration with a finer angular scales (a few arcminutes), including reaching further down into the thickest dust layers of the ZoA ($|b| \gtrsim 5°$). Figure 1.1 shows the Schlegel et al. (1998) all-sky reddening map in Galactic coordinates. $E(B-V)$ values are given on a logarithmic scale from $0.^{m}004$ to $6.^{m}3$. The red and yellow colours at low Galactic latitude indicate the region of high dust-extinction due to our Galaxy. According to Schlegel et al. (1998) themselves, their map at those low Galactic latitude regions is not well calibrated and may be subject to systematic errors.

Schröder et al. (2005; 2007) indeed found that the Schlegel et al. (1998) map overestimates the reddening at low latitudes by $\sim 13\% - 33\%$, depending on the longitudinal proximity to the Galactic Center. The recently published high-resolution $A(K_s)$ extinction maps of the highly obscured regions based on the Rayleigh-Jeans Color Excess (RJCE) method (Zasowski et al. 2009, Majewski et al. 2011, Nidever et al. 2012) improve our understanding of Galactic extinction. They develop this method for measuring the extinction along the line-of-sight by combining the near (2MASS) and mid-IR (IRAC) photometry to determine the stellar reddening. These highly obscured regions are known to have systematically over-estimated extinctions, which thus require a different method to accurately quantify it (e.g., RJCE; see Nidever et al. 2012).

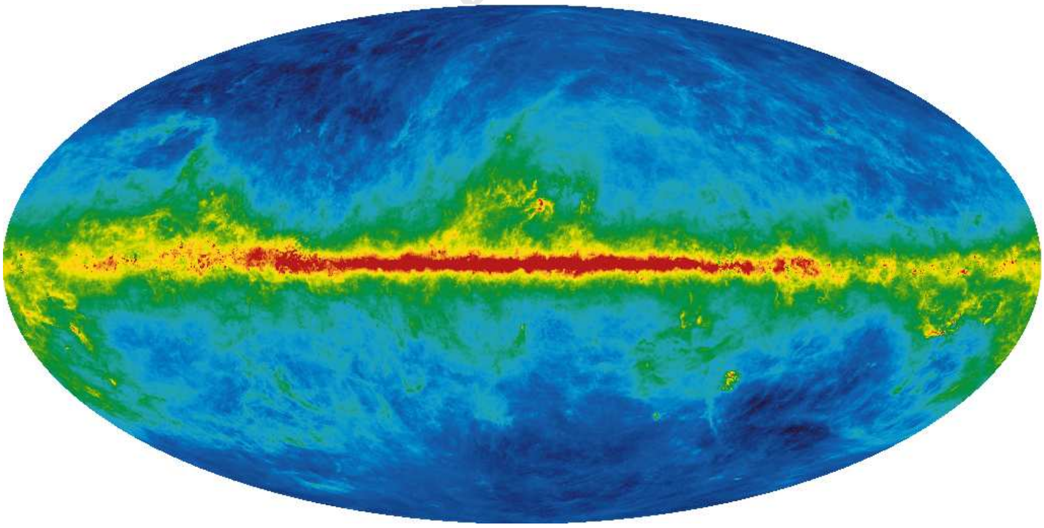

Figure 1.1: Aitoff projection of the Schlegel et al. (1998) reddening map $E(B-V)$ in Galactic coordinates. $E(B-V)$ values are shown on a logarithmic scale from $0.^{m}004$ to $6.^{m}3$. The blue regions represent the regions of low dust-extinction while red and yellow indicate regions with high dust extinction. This Figure is taken from the Legacy Archive for Microwave Background Data Analysis (LAMBDA) data products.

1.1.2 Stellar density

Although dust extinction is not too severe in the NIR, confusion from the stellar emission of the Milky Way itself can be formidable, notably around the Galactic Bulge region where the source counts increase exponentially. The problem of stellar confusion is threefold: (*a*) unresolved stars can be mis-classified as galaxies by automated routines, (*b*) the sky-background noise increases with the stellar density and faint galaxies cannot be detected and (*c*) the faint foreground stars superimposed on a galaxy can be mistakenly identified as part of the galaxy itself, thereby creating large errors in the photometry. Moreover, stars are blue in colour compared to galaxies, and thus stellar contamination imparts a colour bias on the photometry (Cambrésy, Jarrett, & Beichman 2005).

To get a handle on the expected confusion noise distribution for the ZoA, we employ the metric used in 2MASS. Figure 1.2 shows an Aitoff projection of the 2MASS Extended Source Catalog (2MASX) (Jarrett et al. 2000), colour-coded by the stellar density metric $\rho = \log(N_{K_s<14}/\mathrm{deg}^2)$ in the 2MASS Point Source Catalogue (2MPSC) (Skrutskie et al. 2006). $N_{K_s<14}$ represents the number of stars brighter than $14\overset{\mathrm{m}}{.}0$ in the NIR K_s-band. The map is taken from the Explanatory Supplement to the 2MASS All Sky Data Release and Extended Mission Products (Cutri et al. 2006)*. In Figure 1.2, light gray points show regions of $\rho < 3.2$ at $b > 25°$, gray points represent regions of $3.6 < \rho < 3.2$ at $10° < b < 25°$, dark gray points indicate regions of $4 < \rho < 3.6$ at $5° < b < 10°$, and black points corresponds to regions of $\rho > 4$ at $b < 5°$. Stellar confusion becomes important when ρ is greater than 3.6, and is significantly important for values greater than 4.0, where hardly any galaxies are recovered.

1.2 Multi-wavelength surveys of the ZoA

The extent of the ZoA is wavelength-dependent. In the last 20 years, the search for galaxies in the ZoA has become a research field on its own (e.g. "Unveiling large-scale structures behind the Milky Way", ASP Conf. Ser. 67, eds. Balkowski & Kraan-Korteweg 1994, "Mapping the Hidden Universe: The Universe behind the Milky Way - The Universe in HI", ASP Conf. Ser. 218, eds. Kraan-Korteweg, Henning, & Andernach 2000 and "Nearby Large-Scale Structures and the Zone of Avoidance", ASP Conf. Ser. 329, eds. Fairall & Woudt 2005). Various groups have initiated multi-wavelength studies of galaxies located in the ZoA. In the next subsections, I will give a brief description of the ZoA, and enumerate some of the projects undertaken in each waveband. A detailed overview can be found in Kraan-Korteweg & Lahav (2000) and its update in Kraan-Korteweg (2005).

*http://www.ipac.caltech.edu/2mass/releases/allsky/doc/

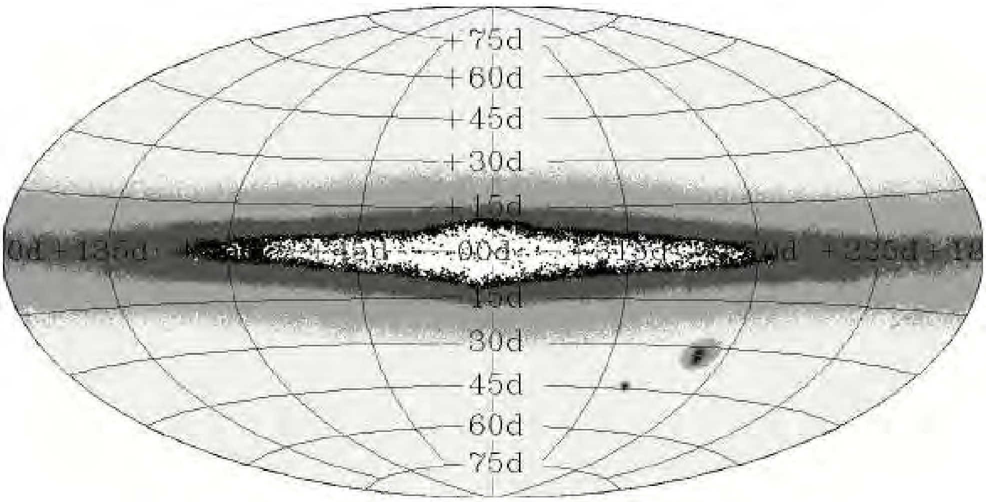

Figure 1.2: Aitoff projection of the 2MASX (Jarrett et al. 2000) colour-coded by the stellar density metric $\rho = \log(N_{K_s<14}/\mathrm{deg}^2)$ in the 2MASS Point Source Catalogue (2MPSC) (Skrutskie et al. 2006). The Galactic Center is mostly empty of XSC galaxies for $\rho > 4$, due to the high density . This Figure is adopted from the Explanatory Supplement to the 2MASS All Sky Data Release and Extended Mission Products

1.2.1 Optical surveys

Although optical surveys are sensitive to all morphological types, they are biased towards larger galaxies as extinction increases, dimming the magnitude, reducing the galaxy size, and changing the galaxy shape. The optical whole-sky galaxy catalogue (Fouque & Paturel 1983; 1985, Paturel et al. 1987), which includes data from the existing optical catalogues at that time, is complete to galaxies with typical diameters $D \gtrsim 1\farcm3$ (Hudson & Lynden-Bell 1991). Figure 1.3 shows an Aitoff distribution of the galaxies from this catalogue in Galactic coordinates. The Zone of Avoidance appears as an empty region at low Galactic latitude $|b| \lesssim 10°$. The red contour marks the extinction at $A_B \simeq 1\fm0$ as given in Schlegel et al. (1998). Excellent agreement exist between the empty region and the extinction contour as shown in Fig. 1.3 (Kraan-Korteweg & Lahav 2000, Kraan-Korteweg 2005).

Various deep optical surveys have reduced the ZoA from $|b| \lesssim 10°$ to $|b| \lesssim 5°$ (a detailed overview of these surveys can be found in Kraan-Korteweg & Lahav 2000 and its update, with focus on the Great Attractor region in Kraan-Korteweg 2005). The most complete view of the sky at optical wavelengths is demonstrated in Fig. 1.4, where all dedicated surveys have been merged into an all-sky catalog (Kraan-Korteweg & Lahav 2000). The ZoA has notably shrunk, and is now roughly complete up to extinction level of $A_B \simeq 3\fm0$.

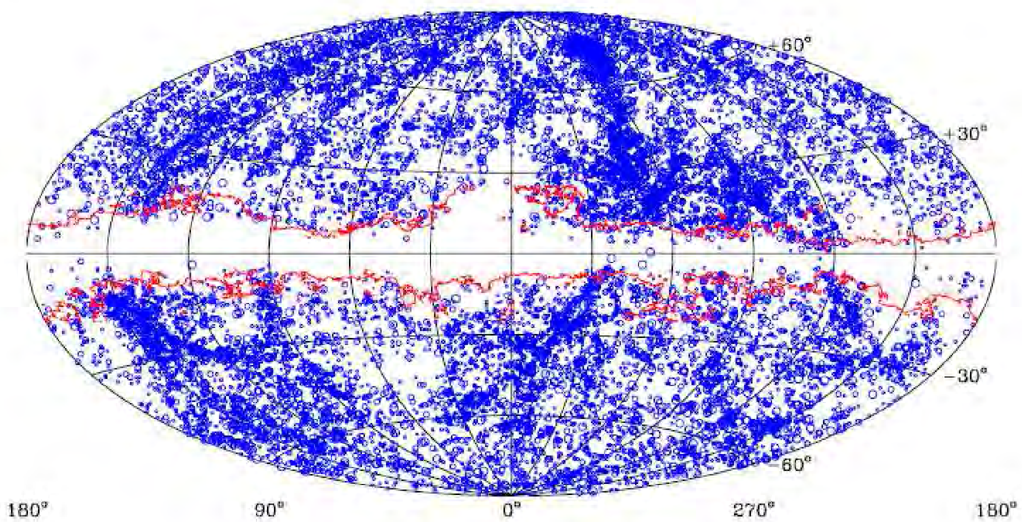

Figure 1.3: Aitoff projection of optical galaxies with $D^{\circ} \gtrsim 1'.3$. The galaxies are size-coded by its diameter. The red contour represents the extinction at $A_B \simeq 1^{\rm m}.0$ as given in Schlegel et al. (1998). Figure adopted from Kraan-Korteweg (2005).

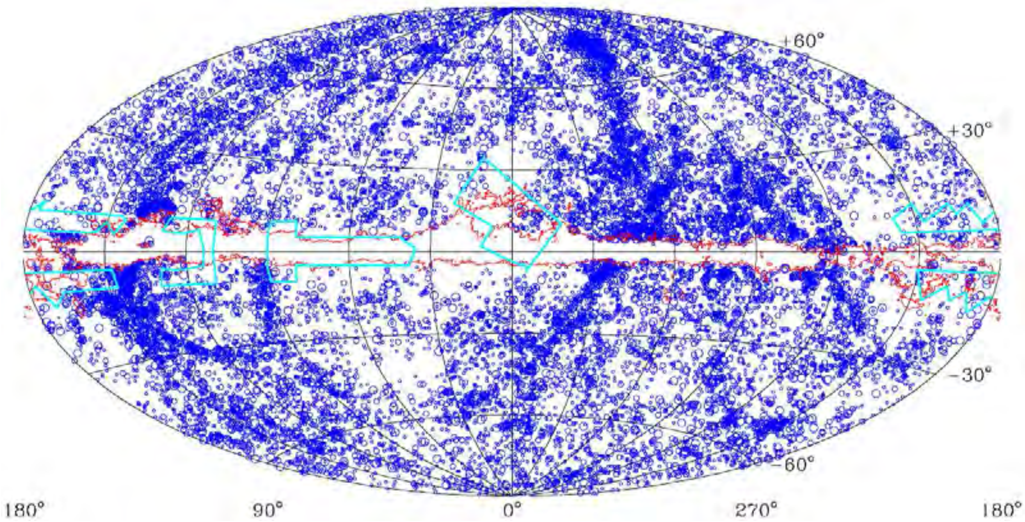

Figure 1.4: Aitoff projection of optical galaxies with $D^{\circ} \gtrsim 1'.3$ including the galaxies identified in deep optical surveys. Note the reduction of the optical ZoA. The galaxies are size-coded by its diameter. The red contour represents the extinction at $A_B \simeq 3^{\rm m}.0$ as determined from Schlegel et al. (1998). Figure adopted from Kraan-Korteweg & Lahav (2000).

1.2.2 Near-infrared surveys

The NIR band is an excellent window to provide complementary observations to optical surveys because it is less affected by extinction, and also sensitive to early-type galaxies that dominate massive clusters and high-density structures in the cosmic web. The largest two surveys in the NIR band presently in existence are: the DEep Near Infrared Southern Sky Survey (DENIS; Epchtein 1997) and the 2 Micron All Sky Survey (2MASS; Skrutskie et al. 2006).

The DENIS NIR-survey covers the southern sky ($-88° < \delta < +2°$) in the I (0.8μm), $J(1.25\mu$m) and $K_s(2.15\mu$m) bands, where the values in brackets correspond to the central wavelength of those respective bands. The completeness limit of the DENIS survey for stars is $18^{\rm m}_{.}5$, $16^{\rm m}_{.}5$, and $14^{\rm m}_{.}0$ for I, J, and K_s-band respectively, leading to 100 million stars (Epchtein 1997; 1998).

The 2MASS NIR survey is an all-sky survey in the $J(1.25\mu$m), $H(1.65\mu$m), and $K_s(2.15\mu$m) bands. The 2MASS observations were conducted between 1997 and 2001 using two 1.3 m telescopes at Mount Hopkins, Arizona, and Cerro Tololo, Chile. Their detection limit is deeper than $15^{\rm m}_{.}8$, $15^{\rm m}_{.}1$, and $14^{\rm m}_{.}3$ at J, H, and K_s-bands respectively, resulting in 471 million sources in the Point Source Catalog (PSC) and 1.6 million sources in the Extended Source Catalog (XSC) (Skrutskie et al. 2006). Figure 1.5 (adopted from Jarrett 2004) displays more than 1.5 million galaxies from the XSC and nearly half billion Milky Way stars from the PSC. Galaxies in Figure 1.5 are colour-coded by its redshift (a detailed description can be found in Jarrett 2004). It is shown that stellar confusion is the main problem in the 2MASX survey because of the relatively large beam, 2.5 arcsec, thus blending between galaxies and foreground stars is an important factor in the ZoA (Log Density > 3.6) (Kraan-Korteweg 2005, Kraan-Korteweg & Jarrett 2005).

1.2.3 HI surveys

While dust extinction and stellar confusion hinder the detection of galaxies in the ZoA in the optical and NIR wavelengths, the Milky Way is transparent to the HI surveys that are designed to detect the 21-cm emission from galaxies. Furthermore, the redshift can be detected directly from the HI signal with high accuracy. In the last few years systematic HI-surveys have revealed thousands of galaxies such as the HI Parkes All Sky Survey (HIPASS; Barnes et al. 2001, Meyer et al. 2004, Koribalski et al. 2004) in the southern sky and the recently launched Effelsberg Bonn HI Survey (EBHIS; Kerp et al. 2011) in the northern sky. Although these surveys penetrate the ZoA, they are spectrally shallow, extending only to a few thousand km/s. Deeper and wider HI surveys are needed to map the ZoA to depths comparable to that of 2MASS.

The HI Parkes Deep Zone of Avoidance Survey (HIZoA) in the southern ZoA ($|b| < 5°$;

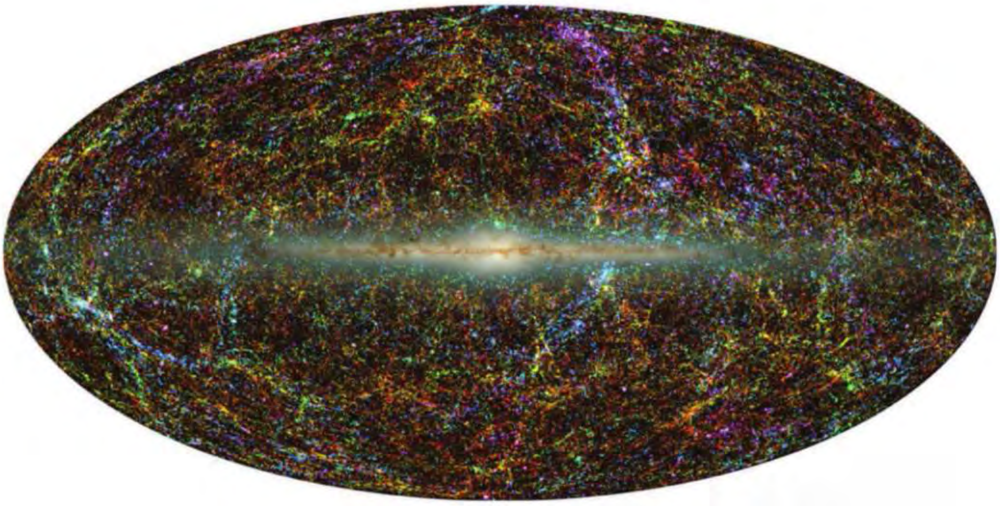

Figure 1.5: Aitoff projection of the 2MASX catalog. More than 1.5 million galaxies from the XSC and nearly half a billion Milky Way stars from the PSC are displayed. Galaxies from the XSC are colour-coded by its redshift. Figure adopted from Jarrett (2004).

Dec $< +15°$) was performed in parallel with the HIPASS survey, but has 5-times longer integration time, and resulted in more than a thousand detected galaxies with rms $\sim$ 6mJy/beam (Kraan-Korteweg et al. 2005, Henning et al. 2005, Donley et al. 2005, Henning et al. in prep). Unfortunately, no similar systematic survey is presently in existence in the northern sky. Selected regions of the northern ZoA have been observed with Arecibo (Henning et al. 2010; 2008). Subsequently, pointed HI observations of optical and bright 2MASX galaxies have been made in both southern and northern skies and revealed many structures hidden behind the Milky Way (Kraan-Korteweg et al. 1996; 2002, Schröder et al. 2009, van Driel et al. 2009, Ramatsoku 2012).

1.3 Cosmological applications and the ZoA

Our lack of knowledge due to the ZoA has implications with regard to the mapping of the local cosmic web and our understanding of its dynamics, including the motion of the LG and bulk flows due to gravitational attractors (Kraan-Korteweg & Lahav 2000, Loeb & Narayan 2008). Many attempts have been made to overcome this problem by artificially filling the ZoA. Bilicki & Chodorowski (2010) show that these methods are valid for the conspicuous features that cross the ZoA, by using the LV as an example. However, various more recent ZoA surveys reveal large-scale structures that were not anticipated. In the following paragraphs I will discuss some cosmological applications that have been affected by the lack of observations in the ZoA.

1.3.1 Large-scale structures

Galaxies are neither uniformly distributed in space nor do they exist in isolation (Fairall 1998). The formation of the cosmic web was described by Fairall (1998) as follows "*large-scale structures are formed by condensations of galaxies with galaxy-galaxy separations less than 200 km/s in redshift space*". Beautifully demonstrated by SDSS (York et al. 2000), the LSS of the cosmic web appears as clusters, walls and filaments of galaxies separated by voids. Tracing this LSS can be used to explain the formation and evolution of the universe. But many of these large-scale structures are bisected and cut-off by the ZoA, notably the Great Attractor, Perseus-Pisces Supercluster, Puppis Cluster and the Local Void. A full census of these important structures, both spatial and kinematic, is necessary in order to understand the evolving universe, and this requires the Zone of Avoidance to be unveiled.

1.3.2 Cosmic flow fields

The motion of a galaxy can be traced through its radial component. This radial component consists of: (a) the recessional velocity, which always points away from us due to the expansion of the universe, and (b) the peculiar velocity, which is the difference between the observed recession velocity of a galaxy and its Hubble velocity. Peculiar velocities arise as a direct result of density inhomogeneities, which cause the galaxies to pile up along overdensities. Of crucial importance here is that the peculiar velocities can be used as a tracer of matter distribution in the universe, both luminous and dark matter.

In the last few decades, the Tully-Fisher relation (Tully & Fisher 1977) for spirals and the Fundamental Plane (FP) relation (Djorgovski & Davis 1987) for elliptical galaxies have been used to carry out many peculiar velocity surveys. The Two Micron All-Sky Tully-Fisher Survey (2MTF; Masters et al. 2008, Hong et al. 2013a;b) is a peculiar velocity survey of all bright inclined spirals with $K_s^\circ \leq 11.^{\rm m}25$ in the 2MASS Redshift Survey (2MRS; Huchra et al. 2005; 2012), which only marginally probes the ZoA. To complement this work a deeper survey dedicated to the ZoA is needed.

1.3.3 The origin of the CMB dipole

The most accurately known peculiar velocity is the motion of the LG relative to the CMB which was measured to be $v_p = 627$ km/s towards $l = 276 \pm 3^\circ$, $b = 30 \pm 3^\circ$ (Kogut et al. 1993). This motion is caused by gravitational influence on the LG due to the density inhomogeneities. Determination of the direction of the peculiar motion of the LG requires a census of galaxies across the whole sky. Due to the lack of observations in the ZoA, current systematic redshift and peculiar velocity whole-sky surveys exclude the ZoA from their analysis (Huchra et al. 2005; 2012, Masters et al. 2008). Many attempts have been made to artificially fill or recreate the ZoA to measure the so-called *"clustering dipole"* (e.g. Erdoğdu et al. 2006a;b, Bilicki et al. 2011, Bilicki 2012). Erdoğdu et al. (2006a;b) for example, reconstructed the local Universe using a Wiener Filter method to repopulate the

ZoA, but the uncertainty in the resulting dipole remains due to the incomplete mapping of the ZoA (Loeb & Narayan 2008).

1.4 Tully-Fisher survey in the ZoA

As mentioned above, understanding of the dynamics of the LG, cosmic flow fields, and the origin of the observed dipole in the CMB require an all-sky peculiar velocity survey, that includes the ZoA. Two independent projects of data acquisition to determine the cosmic flow in the ZoA have been launched by Kraan-Korteweg and collaborators. These data will cover both northern and southern ZoA, hence providing the most complete survey in the ZoA.

1.4.1 Deep NIR follow-up survey of the HIZoA galaxies

In 2009 systematic deep NIR follow-up survey in the J, H, and K_s-bands of the HIZoA galaxies was started. These observations were conducted from the InfraRed Survey Facility (IRSF) on the 1.4m telescope at Sutherland, South Africa. The 10 min. of exposure time accumulated for each galaxy in the HIZoA catalog and the IRSF resolution of $0\farcs45$/pixel resulted in high quality images in the ZoA (Williams 2011; Williams et al. 2011; Said et al. in prep).

1.4.2 HI follow-up survey of the 2MASX galaxies

In 2009, Kraan-Korteweg and collaborators started an observing programme to obtain HI redshifts for all bright galaxies in the 2MASX (Jarrett et al. 2000) with $K_s^o < 11.25$ mag in the ZoA ($|b| < 10°$) which do not have any previous redshift determinations. The Nançay Radio Telescope (NRT) in France and the Parkes radio telescope in Australia have been used to cover the entire ZoA. Over a thousand galaxies without previous redshifts have been observed with the NRT (Dec $> -38°$), resulting in more than 250 detected galaxies (Ramatsoku 2012). Parkes observations started in 2013 and 74 galaxies without previous redshifts have been observed to date (Said et al. in prep).

1.5 Motivation of peculiar velocity survey in the ZoA

While the HI surveys revealed many structures hidden behind the Milky Way, peculiar velocity determinations in the ZoA have not been attempted so far. Given the success of the HIZoA survey, which results in more than a thousand galaxies in the ZoA, and its high fidelity NIR follow up survey, peculiar velocity surveys have become possible in the ZoA. In this thesis we aim to use the Tully-Fisher method and the available data to determine reliable peculiar velocities for the galaxies in the southern ZoA which are excluded from the 2MRS and the 2MTF. This will be expanded to include galaxies in the northern ZoA in the future. The combined data set will provide a peculiar velocity survey over the full 360°-circle of the ZOA. The 2MTF, thus supplemented with our data will result in a complete all-sky peculiar velocity survey.

1.6 Outline of this thesis

This thesis is organized as follows. Chapter 2 presents the derivation of the Tully-Fisher relation in the NIR J, H, and K_s-bands. This calibration closely follows the procedures of Masters et al. (2008) for total magnitudes, but uses isophotal magnitudes instead. In Chapter 3, I discuss changes in the inclination due to foreground extinction. Different methods used to test this effect and its influence on the final derived peculiar velocities are presented. Chapter 4 shows the derivation of the TF distance and peculiar velocities. Preliminary results of peculiar velocity and cosmic flow field are discussed. I finalize with the conclusion and an outline of future work in Chapter 5.

Chapter 2

The Absolute Calibration of the Tully-Fisher Relation

This chapter presents the derivation of the absolute calibration of the Tully-Fisher relation for isophotal magnitudes in the Near-InfraRed (NIR) J, H, and K_s-bands. This calibration closely follows the precepts of the 2MTF calibration elaborated in Masters et al. (2008) for "total" magnitudes. The isophotal magnitudes of the same calibration sample (888 galaxies) were extracted from the 2MASX, for the near-infrared J, H, and K_s-bands. There is hardly any change in the TF scatter compared to Masters et al. (2008) because the calibration sample is not affected by the Galactic Plane (GP). However, this is not true when galaxies are affected by foreground extinction closer to the plane of the Milky Way. Here application of the isophotal TF brings a vast improvement (see also Chapter 4).

2.1 Introduction

In the following, I will present an overview of the discovery, derivations and applications of the Tully-Fisher relation.

Balkowski et al. (1974) gave the first description of the correlation between the luminosity and the line-width of spiral galaxies but did not apply it as a distance indicator. Tully and Fisher were the first to propose its use as a distance indicator (Tully & Fisher 1977). Since then, the Tully-Fisher (TF) relation has been widely used to measure extragalactic distances and determine the Hubble constant.

The rotational velocities of spiral galaxies (distance-independent) can be determined from the HI line width. The absolute magnitudes (distance-dependent) can then be derived from a suitably calibrated sample once the photometry is obtained. As with any secondary distance indicator, the TF must be calibrated by the distance scale (template relation) based on a primary distance indicator. Raw data and applied corrections used in the measurement of TF distances should be consistent with these used in the derivation of the TF calibration.

In the last few decades, many TF template relations have been derived using either different samples or methods. Shortly after the inception of the TF relation, Aaronson et al. (1979) calibrated the TF relation in the NIR $H(1.6\mu m)$ for spiral galaxies in clusters. The NIR suffers less from dust extinction and is more sensitive to stellar mass. They found that in the infrared the scatter is lower than that in the B-band and that the slope is much steeper. Using a considerably larger sample of spirals to investigate several properties of the TF relation, Aaronson & Mould (1983) claimed that the TF is type-independent in the infrared (i.e. the slope and intercept does not change with the spiral type). This conclusion has been contradicted by subsequent larger surveys (Giovanelli et al. 1997a, Masters et al. 2008); Section 2.4

The effect of the Malmquist bias on the slope and zero-point of the TF relation has been discussed extensively (e.g., Kraan-Korteweg, Cameron, & Tammann 1986; Bottinelli et al. 1986; Kraan-Korteweg, Cameron, & Tammann 1988). To eliminate this effect, the application of the inverse fit of the TF relation (where only errors in x are taken into consideration) was suggested by Kraan-Korteweg et al. (1986). On the other hand, Pierce & Tully (1988; 1992) claim that the systematic effects are limited.

Freedman (1990) used Cepheid distances to five nearby late-type galaxies to calibrate the infrared (H-band) TF relation. The dispersion in this relation was remarkably small (0.15 mag). Peletier & Willner (1991; 1993) used a larger sample in the Virgo cluster and Ursa Major cluster to derive TF relations. The intrinsic dispersion among Virgo cluster galaxies amounts to 0.5 mag and 0.4 mag in the blue and infrared respectively. For Ursa Major cluster spirals, the intrinsic dispersion was smaller than for Virgo, but still larger than that claimed in Freedman (1990).

Willick et al. (1995; 1996) calibrated the direct and inverse I-band TF relation for six samples: two TF cluster samples and four TF field samples. They studied the slope and scatter for each sample. They found an observed scatter of $0.^{m}38$ - $0.^{m}43$ for their samples, and an intrinsic scatter of $0.^{m}3$.

NIR fluxes in the J-$(1.25\mu m)$, K-$(2.2\mu m)$, and L-$(3.5\mu m)$ bands of nearby bright spiral galaxies derived from Cosmic Background Explorer (COBE)/Diffuse Infrared Background Experiment (DIRBE) have been used with Cepheid distances to construct TF relations (Malhotra et al. 1996). The scatter in these relations was very small compared to the I-band relations: $0.^{m}09$, $0.^{m}13$, and $0.^{m}20$ in the J-, K-, and L-bands respectively. The authors also tried to extend the TF relation to longer wavelengths, but no evidence for the TF relation has been seen for wavelengths larger than $10\mu m$ because the fluxes at these wavelengths are not related to the stellar mass.

A detailed absolute calibration of the I-band TF relation was performed by Giovanelli et al. (1997a;b) who used infrared photometry and velocity-widths of 782 spiral galaxies in 24 clusters. They divided their sample in two groups: the "*in*" sample which included cluster member galaxies and the "*in+*" sample which included cluster galaxies plus neighboring galaxies. They analyzed bias and scatter in the TF relation and concluded that the scatter is lowest among galaxies with largest line-widths (larger dynamical mass) and largest among galaxies with narrow line-widths (lower dynamical mass).

Based on Cepheid distances to 21 galaxies, Sakai et al. (2000) derived TF relation in the B, V, R, I, and H-bands. These relations were used to derive a value of H_0. At the same time, Tully & Pierce (2000), Rothberg et al. (2000) performed a calibration of the B, R, I, and K relations. To avoid the Malmquist bias, they used the inverse method to fit the TF relation. Bouché & Schneider (2000) used 2MASS J, H, and K_s-bands to derive TF relations in the Zone of Avoidance. They used five different types of magnitudes from 2MASS (Jarrett et al. 2000). They conclude that the scatter was lowest for the isophotal K_s-fiducial 20 mag/arcsec^2 TF relation.

Macri (2001) derived R, I, H, and K_s-band TF relations based on Cepheid distances. He used both total and isophotal magnitudes with the 20% HI-line-width (the width measured at 20% of the peak flux). His results indicate that isophotal H, K_s magnitudes and total I magnitudes relations yield comparable distances. These relations have a scatter of $\sim 0\overset{\rm m}{.}2$.

Karachentsev et al. (2002) used a sample of the most edge-on field galaxies in the B, I, J, H, and K_s-bands to derive TF relations. They claimed that due to internal extinction in galaxies, the derived slope increases from 4.9 in the B-band to 9.3 in the K_s-band. The scatter is lowest in the I-band and highest in the H-band.

Masters et al. (2006) followed the same procedure described by Giovanelli et al. (1997b) but with a larger sample to derive a new I-band TF relation. Their sample consists of 807 galaxies in the vicinity of 31 clusters and groups. This template relation has been used by Springob et al. (2007) to derive peculiar velocities of galaxies in the SFI++ catalog, which contains 4861 field and cluster spiral galaxies. Later, Masters et al. (2008) used similar procedures with a slightly larger sample to derive the absolute calibration of the J, H, and K_s-bands relations. These relations are the first step towards the 2MASS Tully-Fisher Survey (2MTF) which intends to provide a complete TF analysis (i.e. distance and peculiar velocity) to all bright inclined spirals in the 2MASS Redshift Survey (2MRS; Huchra et al. 2005; 2012).

Recently, two independent groups started to use the mid-infrared to derive the TF relation. Sorce et al. (2013) use Spitzer ($3.6\mu m$) photometry for 213 cluster galaxies to derive the TF relation. Lagattuta et al. (2013) use the mid-infrared ($3.4\mu m$) $W1$-band of the Wide-field Infrared Survey Explorer (WISE) satellite with a larger sample of 568 field and cluster galaxies drawn from the 2MTF catalog to derive the TF relation. While Sorce et al. (2013) adopted the inverse fitting scheme, Lagattuta et al. (2013) used a bivariate scheme, where errors in both x and y are taken into consideration. Using different fitting schemes and different bias corrections makes it difficult to compare both relations.

Following all these derivations, I will present in this chapter a further calibration of the J, H, and K_s-bands TF relations, based on the "isophotal" magnitude of 888 2MASS galaxies. In agreement with the early work done by Bouché & Schneider (2000) I will show that the "isophotal" NIR TF is equally good as the NIR TF based on total magnitudes, but better suited to galaxies affected by extinction. This Chapter is organized as follows. In Section 2.2, I discuss the advantages of using the isophotal magnitude. Section 2.3 describes the data used for the calibration of the TF relation. Section 2.4 provides the corrections applied to the TF parameters. The resulting TF relations and associated scatter is presented in Section 2.5.

2.2 Zone of Avoidance and the isophotal magnitude

Although the total magnitude gives the best estimate of the total luminosity (correlated to the total stellar mass of the galaxy), it is difficult to determine reliable total magnitudes for (a) low surface brightness galaxies for which these values can be severely underestimated, or (b) galaxies close to or in the Zone of Avoidance. Due to the foreground dust extinction and high stellar density in the ZoA, the fainter outer parts of a galaxy are usually not recovered in the extrapolation of the surface brightness profile to yield total magnitudes.

Therefore, the advantage of using isophotal magnitudes over total is twofold. While the Galactic obscuration is not the main problem in the NIR J, H, and K_s-bands, the short exposures (8 sec.) of the 2MASS survey limit the determination of total magnitude. In the ZoA the situation is more difficult because of the foreground extinction.

To quantitatively determine the loss in total magnitudes in the 2MASX, I compare the magnitudes of the shallow 2MASX survey with a deeper and more spatially resolved survey. I select a sample of 66 galaxies, observed both in 2MASX (Jarrett et al. 2000) and the IRSF Catalog* (Williams et al. 2011). The latter is approximately 2 magnitudes deeper in the K_s-band, given its exposure time (10 min.) compared to 2MASX (8 sec.) and a resolution of $0\farcs45$/pix compared to the 2MASX resolution of $2''$/pix. I used the "total" extrapolated magnitudes and fiducial "isophotal" magnitudes measured in an elliptical aperture defined at the $K_s = 20$ mag arcsec^{-2} to construct a comparison between 2MASX and IRSF. The

*The IRSF survey is discussed in more detail in Chapter 4 metric used to calculate the offset between 2MASS and IRSF magnitudes is

$$\Delta m = m(\text{2MASS}) - m(\text{IRSF}). \tag{2.1}$$

Figure 2.1 shows the offsets between the 2MASS and IRSF for both total (left panel) and isophotal (right panel) magnitudes in the J, H, and K_s-bands (top to bottom). It clearly shows that the offsets between 2MASX and IRSF for the "isophotal" magnitudes are insignificant while, the offsets are very high for the total magnitude. High offsets will produce systematic errors in the measurement of peculiar velocities. The mean offsets for each band is printed in the bottom left corner of each plot. Furthermore, the scatter in the offsets of the "isophotal" magnitudes is far smaller than that in the "total" magnitudes, it is reduced by more than a factor of two. Table 2.1 summarizes the mean offsets and the scatter values for each band.

Band	Total		Isophotal	
	Δm	σ	Δm	σ
J	0.228	0.363	−0.020	0.155
H	0.252	0.293	−0.039	0.139
K	0.263	0.308	−0.033	0.159

Table 2.1: Comparison between 2MASS and IRSF magnitudes using the total extrapolated magnitudes and fiducial isophotal magnitudes measured in an elliptical aperture defined at the $K_s = 20$ mag arcsec^{-2}

While total 2MASS magnitudes are fainter than total IRSF magnitudes, isophotal 2MASS magnitudes are brighter than isophotal IRSF magnitudes. This positive offset in total magnitude is due to the improved sensitivity and higher resolution ($0\farcs45$/pix) of the IRSF/SIRIUS data, which allows measurement of the surface brightness profile further along the disk compared to 2MASS. On the other hand, the insignificant negative offset in isophotal magnitude can be explained by the lower resolution of 2MASS ($2''$/pix), which does not resolve stars superimposed on the galaxy.

In conclusion, when working with low surface brightness galaxies or galaxies affected by dust, "isophotal" magnitudes should preferentially be used over "total" magnitudes.

2.3 The TF parameters

Two observational parameters describe the TF relation. The distance-independent rotation width is obtained from spectral data, and the imaging data provides all photometric quantities of interest. Different authors prefer different quantities, such as, the 20% line-width versus the 50% line-width, and isophotal versus total magnitudes. Throughout this thesis, I will work with w_{50}, which is the width measured at 50% of the peak flux of the HI profile

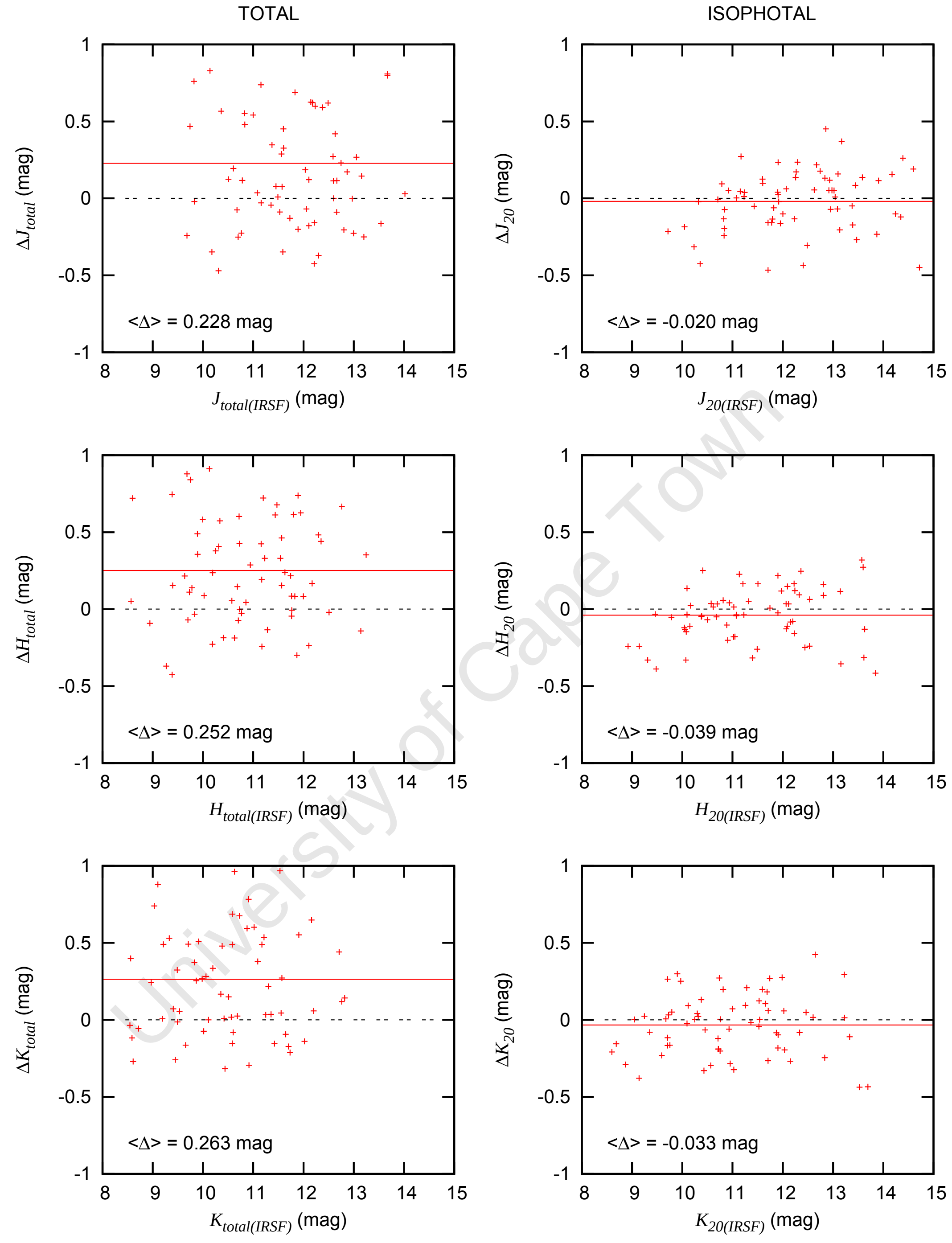

Figure 2.1: Comparison of 2MASS and IRSF photometry of ZoA galaxies. The left panels display the total magnitudes and the right panels display the isophotal magnitudes with J, H, and K_s-band arranged from top to bottom. In all panels, solid red lines mark the mean of the difference, and the dashed black lines represent the zero-line. The mean difference is given in the bottom left corner of each plot.

and the isophotal magnitude in the J, H, and K_s-bands. Many different algorithms have been used over the years to derive w_{50} (Koribalski et al. 2004, Springob et al. 2005, Hong et al. 2013b). These different algorithms can have a serious effect on the accuracy of the value of w_{50} if the S/N of the spectra are low. Hong et al. (2013b) calculated w_{50} using different methods and found no significant differences. Figure 2.2 shows the data from Table 2 in Hong et al. (2013b), which can be also found online[†]. Most TF samples including the two samples we use here and in Chapter 4, contain galaxies with high S/N spectra, so the noise does not affect the width measurement and the difference between different algorithms becomes negligible as seen in Fig. 2.2.

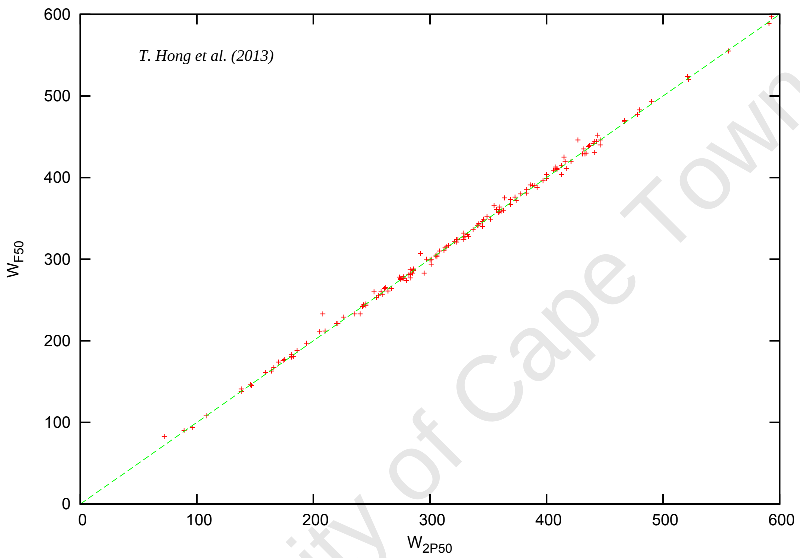

Figure 2.2: Comparison between two different methods of calculating w_{50}. Data are taken from Hong et al. (2013b)

The calibration sample of galaxies is the same as that used in Masters et al. (2008)[‡]. The rotation-widths were obtained from either the Cornell HI digital archive (Springob et al. 2005) or optical rotation curves (Catinella et al. 2005). The photometric quantities of the calibration sample are a mix of J, H, and K_s-bands quantities from 2MASX and I-band quantities from Masters et al. (2006). I cross-match the Masters et al. (2008) calibration sample with the 2MASX catalog to extract their "isophotal" magnitudes.

2.3.1 Rotation widths

The rotation widths are drawn completely from the Masters et al. (2008) calibration sample which is available online[§], see Springob et al. 2005 for details.

[†] http://ict.icrar.org/2MTF

[‡] We thank Karen Masters for making that available to use

[§] http://www.icg.port.ac.uk/∼mastersk/TFdata.html

2.3.2 Photometry

All photometric quantities are derived from the 2MASX catalog. Their properties are described online in Cutri et al. (2006)[¶]. The photometric quantities of the TF calibration are:

1. Isophotal magnitude: We use the J, H, and K_s-bands fiducial isophotal magnitudes measured at 1 σ background noise of typically 21.4, 20.6, and 20.0 mag arcsec^{-2} respectively (Jarrett et al. 2003).
2. J-band axial ratio: The J-band axial ratio $(a/b)_J$ fit to the 3 σ isophote is used (the isophote corresponds to a surface brightness $\sim$ 3 times the background noise). The values for the surface brightness $\sim$ 3 σ are 20.09 mag arcsec^{-2} at J, 19.34 mag arcsec^{-2} at H, and 18.55 mag arcsec^{-2} at K_s-band (Jarrett et al. 2000).
3. Central surface brightness μ_c: The central surface brightness μ_c in the J, H, and K_s-bands obtained from the 2MASS XSC. This parameter is necessary for the derivation of the Galactic extinction corrections (Section 2.4).
4. The colour reddening $E(B-V)$: Galactic extinction A_J, A_H, and A_{K_s} are approximated by the colour reddening $E(B-V)$ from the DIRBE dust map (Schlegel et al. 1998).

2.4 Corrections

To construct a global TF relation, the photometric quantities from the 2MASX must be corrected for the cosmological redshift, internal extinction, and Galactic extinction. Due to the broad range in surface brightness and colour of the galaxy sample, further bias corrections have to be applied. We follow the method for bias correction by Masters et al. (2008), which is described below.

2.4.1 Photometric corrections

The corrected absolute magnitude, derived from the observed apparent magnitude is calculated as follows:

$$M_{corr} - 5\log h = m_{obs} - A_X - I_X - k_X - 5\log v_{CMB} - 15, \tag{2.2}$$

where A_X, I_X, and k_X are a correction for foreground extinction due to the dust in the Milky Way, a correction for extinction internal to the galaxy itself, and a cosmological k-correction respectively. Because these three corrections are wavelength-dependent, the index X refers to the wavelength band.

k-correction

A compensating term known as k-correction needs to be applied to the observed magnitude in each band because of redshift. k-corrections become smaller as one observes further in

[¶] http://www.ipac.caltech.edu/2mass/releases/allsky/doc/

the red and are negative in J, H, and K_s-bands, (see Figures 5-15 in Poggianti 1997).

I apply the k-correction as described in Masters et al. (2003) which is derived from applying a linear fit to the low redshift end of the models of Poggianti (1997).

$$k_J = -0.68z, \tag{2.3a}$$

$$k_H = -0.40z, \tag{2.3b}$$

$$k_{K_s} = -1.52z. \tag{2.3c}$$

The galaxies in the calibration sample lie within the range of 500 to 10000 km s^{-1}, which means that the highest values of k-corrections are $0\overset{\rm m}{.}02$ for the J-band, $0\overset{\rm m}{.}01$ for the H-band, and $0\overset{\rm m}{.}05$ for the K_s-band; as such, these values are insignificant compared to the values from extinction corrections.

Internal extinction

Dust extinction internal to galaxies themselves is a challenging quantity to estimate. Since the early work of Holmberg (1958) it has been widely assumed that spiral galaxies are mostly transparent. But later studies suggest that spiral galaxies are optically thick (Valentijn 1990). Again, this study received some criticism (e.g. Burstein et al. 1991). The best study to date (Holwerda et al. 2009), uses occulting galaxy pairs to show that dust distributions vary in a given galaxy, creating both optically thin and thick regions.

This problem has been investigated by several authors from different aspects. Most correction models for the internal extinction have been constructed as a function of inclination. In the TF relation, inclined galaxies are preferentially used, but the magnitudes of inclined galaxies are more affected by dust. In our analysis I adopt the empirical relation of internal extinction, which is in agreement with various other authors (Giovanelli et al. 1994, Tully et al. 1998, Masters et al. 2003), which is dependent on axial ratio and waveband, as follows:

$$I_\lambda = \gamma \log(a/b). \tag{2.4}$$

The J-band axial ratio $(b/a)_J$ is the best tracer of the inclination, as it suffers less than the H, and K_s-bands from the effect of the bulge if the 3 σ isophote is near to the central regions (Masters et al. 2003). The axial ratio needs to be corrected for seeing, which is parameterized as

$$(a/b)_{corr} = (a/b)_{obs}(1 - 0.02x + 0.21x^2 - 0.01x^3), \tag{2.5}$$

where x = FWHM($\frac{a/b}{r_{20}}$), and FWHM = $2''\!.5$ (the full-width half-maximum of the seeing disc). Masters et al. (2003) provide different values of γ in J, H, and K_s-bands from different statistical tests, I adopt their values of γ derived from the sample with $\log(a/b) \leq 0.5$ for all galaxies:

$$\gamma_J = 0.48 \pm 0.15, \tag{2.6a}$$
$$\gamma_H = 0.39 \pm 0.15, \tag{2.6b}$$
$$\gamma_{K_s} = 0.26 \pm 0.15. \tag{2.6c}$$

Galactic foreground extinction

Galaxies appear smaller and fainter due to the dust extinction in the Milky Way. Therefore a correction to the isophotal magnitude is needed to account for the loss of light due to this dimming. Cameron (1990) uses a clean sample of 23 large elliptical and spirals galaxies with known surface photometry to simulate this effect in the optical B-band. A recent study by Riad, Kraan-Korteweg, & Woudt (2010) used a larger sample of 25 elliptical and lenticular, and 39 spiral galaxies from the 2MASS Large Galaxy Atlas (LGA) (Jarrett et al. 2003), to study this effect in more detail for the NIR J, H, and K_s-bands. They present two methods (which we adopt in this study) to apply the isophotal correction: (i) the average correction method which is a very direct application, and (ii) the more optimized correction methods which are more accurate than the average correction but require a fit to the light profile of the galaxy to determine either the disc central surface brightness, μ_0, or the combined disc plus bulge central surface brightness, μ_c. While we were able to use the optimized correction, because the central surface brightness is available in the 2MASX, both correction methods are presented here because the central surface brightness is not always available.

Average isophotal correction

The average correction method to the isophotal radius and magnitude uses the standard formalism proposed by Cameron (1990):

$$f(R) = 10^{a(A_\lambda)^b}, \tag{2.7a}$$
$$\Delta m_{iso} = F(A_\lambda)^v, \tag{2.7b}$$

where

$$f(R) = \frac{R^\circ}{R}, \tag{2.8a}$$
$$\Delta m_{iso} = m_{iso} - m^\circ_{iso}, \tag{2.8b}$$

and m°_{iso}, m_{iso}, R°, and R are the intrinsic and absorbed magnitudes and radii.

A_λ can be expressed in terms of the reddening, e.g. Schlegel et al. (1998)

$$A_J = 0.902E(B-V), \quad (2.9a)$$
$$A_H = 0.576E(B-V), \quad (2.9b)$$
$$A_K = 0.367E(B-V), \quad (2.9c)$$

where $E(B-V)$ is the optical colour-reddening. The values of the fitting parameters F, v, a, and b are taken from Riad et al. (2010). They are given in Table 2.2.

Param.	J	H	K_s
a	0.1169±0.0007	0.1185±0.0006	0.1453±0.0005
b	1.5650±0.0056	1.5718±0.0047	1.4778±0.0032
F	0.1346±0.0008	0.1442±0.0007	0.1982±0.0009
v	1.9080±0.0064	1.8755±0.0053	1.7093±0.0049

Table 2.2: Average fitting parameters a, b, F, and v for spiral galaxies

Optimized isophotal correction based on μ_c

The optimized correction method using μ_c, the central surface brightness, is more accurate than the average correction because it correlates with the morphological type. When incorporating μ_c, Riad et al. (2010) determine the correction to be of the form:

$$f(R, \mu_c) = 10^{a(\mu_c)\cdot(A_\lambda)^{b(\mu_c)}}, \quad (2.10a)$$
$$\Delta m_{iso}(\mu_c) = F(\mu_c)\cdot(A_\lambda)^{v(\mu_c)}, \quad (2.10b)$$

where

$$a(\mu_c) = a_\circ \exp(\mu_c \cdot a_1), \quad (2.11a)$$
$$b(\mu_c) = b_\circ \exp(\mu_c \cdot b_1), \quad (2.11b)$$
$$F(\mu_c) = F_\circ \exp(\mu_c \cdot F_1), \quad (2.11c)$$
$$v(\mu_c) = v_\circ \exp(\mu_c \cdot v_1). \quad (2.11d)$$

The values of these parameters are given in Table 2.3.

I compare the optimized correction based on μ_c and the average correction. Figure 2.3 shows the difference of the isophotal correction methods as a function of the foreground extinction. Figure 2.3 shows that the difference between the two methods is negligible in the K_s-band while it is significant in the J, and H-bands for $A_\lambda > 0.1$ mag.

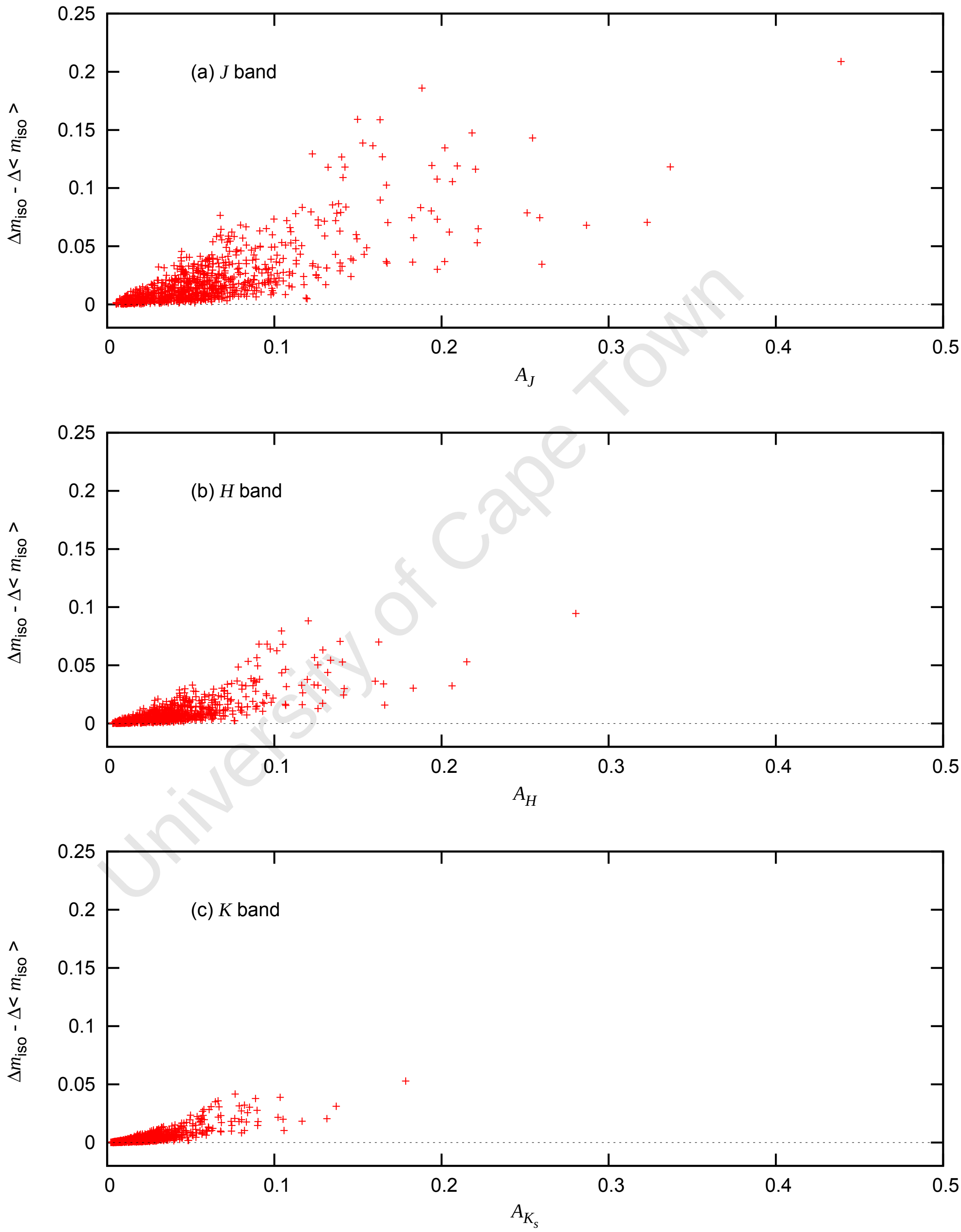

Figure 2.3: Comparison between the optimized correction based on μ_c (Δm_{iso}) and the average correction ($\Delta < m_{iso} >$)

Param.	J-band	H-band	K_s-band
$a_\circ$	0.0068	0.0095	0.0157
a_1	0.1953	0.1824	0.1641
$b_\circ$	2.7721	2.5213	1.3653
b_1	−0.0455	−0.0397	0.0009
$F_\circ$	0.0003	0.0007	0.0012
F_1	0.4136	0.3833	0.3751
$v_\circ$	6.4910	4.6215	2.3296
v_1	−0.0866	−0.0674	−0.0267

Table 2.3: Parameters $a_\circ, b_\circ, F_\circ, v_\circ, a_1, b_1, F_1$ and v_1 for the μ_c optimization equation.

2.4.2 Bias corrections

Morphological correction

Many TF samples including the one we use here, contain a broad range of spiral types. A single relation may not be appropriate for all spiral types as expressed already by Tully & Fisher themselves. Masters et al. (2008) found type dependences with their sample, and my analysis of this effect based on the "isophotal" magnitude yields similar trends. Figures 2.4, 2.5 and 2.6 show TF diagrams in the J, H, and K_s-bands of galaxies in our sample divided according to their morphological type. The earlier types have a shallower slope than later types. We correct to an Sc type (less bulge, more disk component) relation.

In the J-band we use

$$\Delta M_{Sa} = 0.27 - 2.46(\log W - 2.5),$$
$$\Delta M_{Sb} = 0.15 - 1.14(\log W - 2.5).$$

In the H-band we use

$$\Delta M_{Sa} = 0.22 - 2.81(\log W - 2.5),$$
$$\Delta M_{Sb} = 0.15 - 1.16(\log W - 2.5).$$

In the K_s-band we use

$$\Delta M_{Sa} = 0.11 - 3.51(\log W - 2.5),$$
$$\Delta M_{Sb} = 0.13 - 1.44(\log W - 2.5).$$

These values are derived using the data for each sample before any bias corrections.

Incompleteness bias

Brighter galaxies in a given cluster are more likely to enter the sample. This affects the derived TF relation in three ways: (a) shallowing the TF slope, because galaxies with low line-width will preferentially lie above the linear relation, (b) brightening the zero point, because of the same reason, (c) underestimating the scatter, because galaxies with low line-width lying below the linear TF relation, which are associated with high scatter, are missing

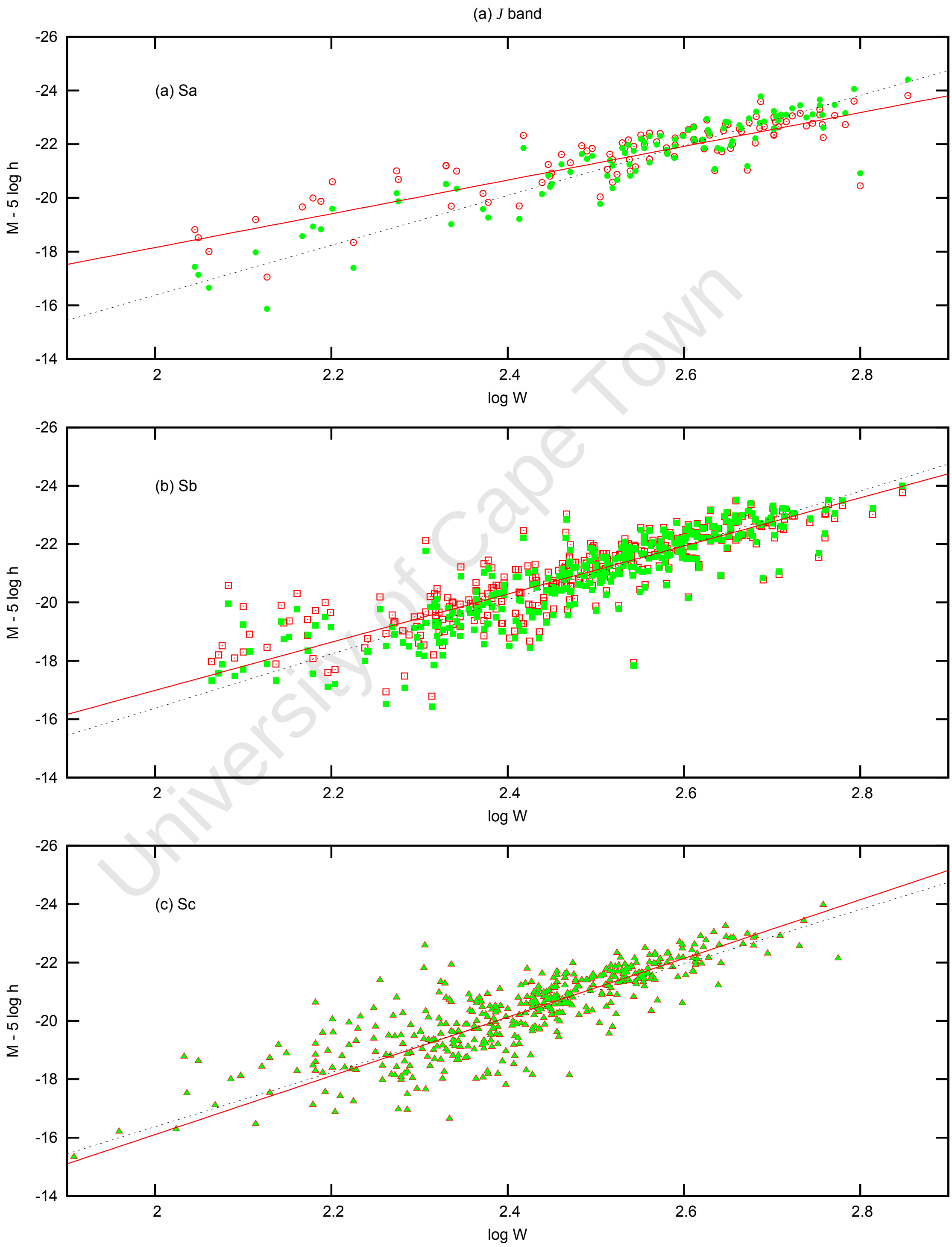

Figure 2.4: *J*-band TF relation for the *in+* sample separated by morphological type (a) Sa and earlier; (b) Sb; (c) Sc and later. Open symbols show the magnitudes corrected for all biases except morphological type. The solid line shows the fits to these points. The filled symbols are the magnitudes after the morphological type correction is applied and the dashed line in all panels shows the final fit to the whole sample.

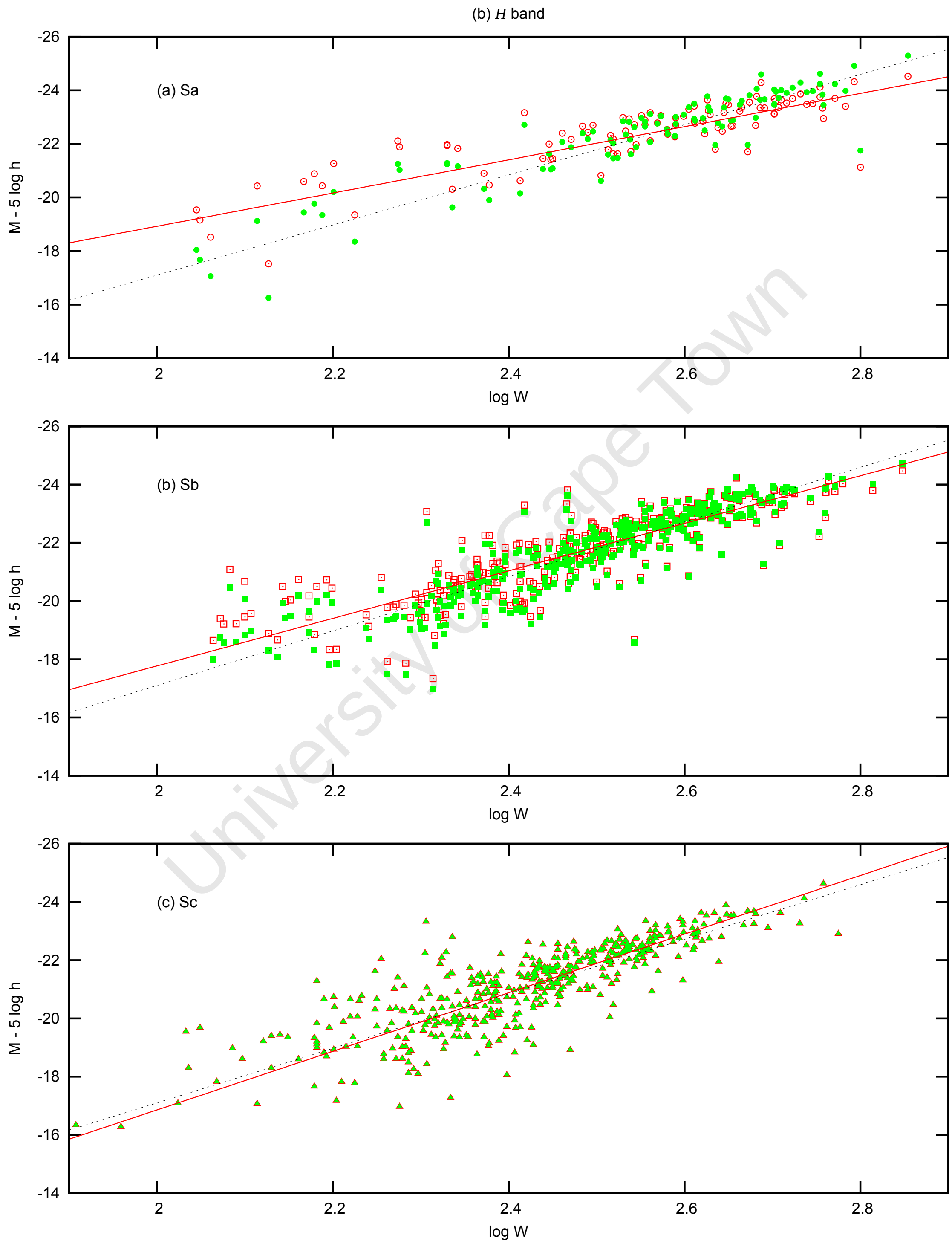

Figure 2.5: H-band TF relation for the *in+* sample separated by morphological type (a) Sa and earlier; (b) Sb; (c) Sc and later. Open symbols show the magnitudes corrected for all biases except morphological type. The solid line shows the fits to these points. The filled symbols are the magnitudes after the morphological type correction is applied and the dashed line in all panels shows the final fit to the whole sample.

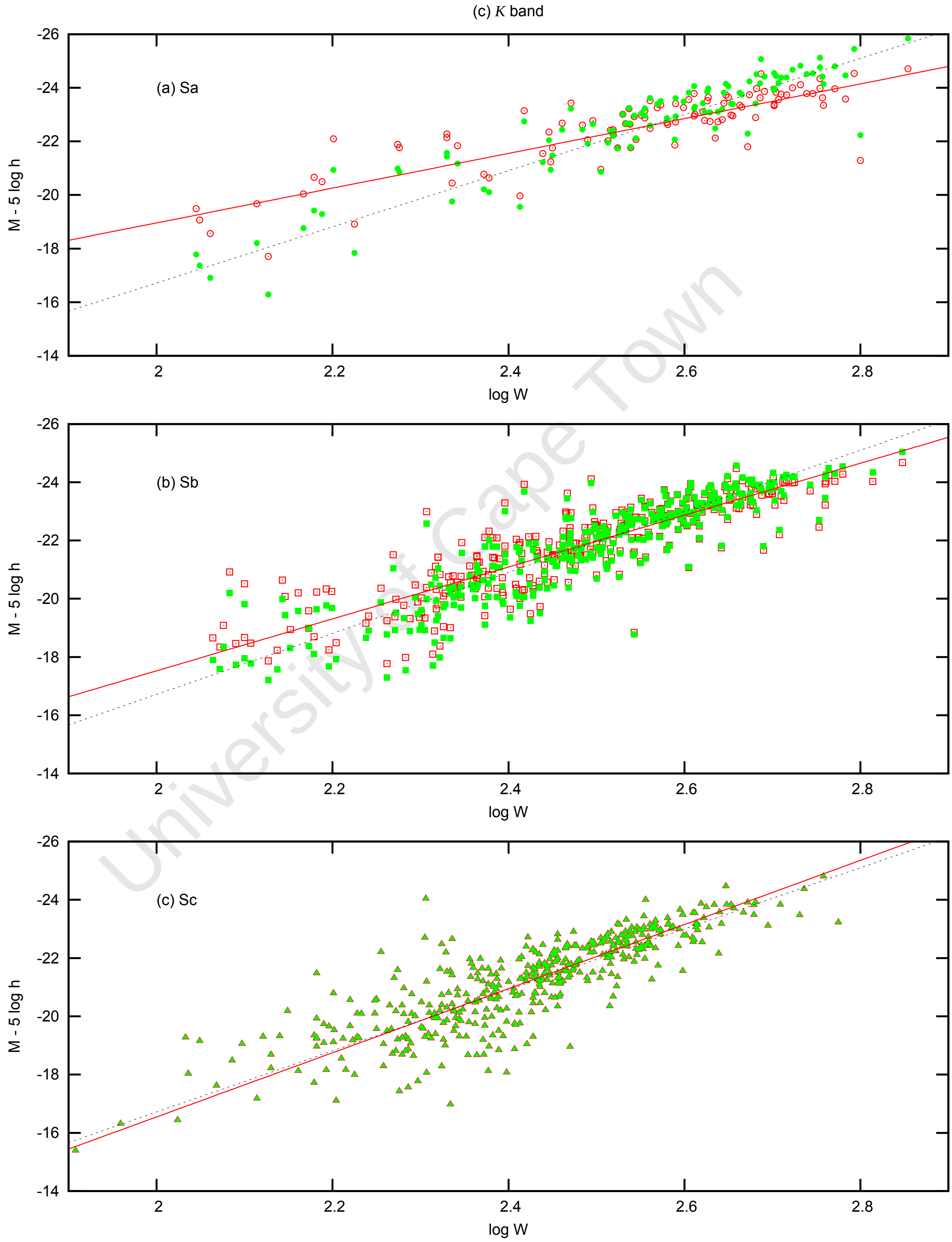

Figure 2.6: K-band TF relation for the *in+* sample separated by morphological type (a) Sa and earlier; (b) Sb; (c) Sc and later. Open symbols show the magnitudes corrected for all biases except morphological type. The solid line shows the fits to these points. The filled symbols are the magnitudes after the morphological type correction is applied and the dashed line in all panels shows the final fit to the whole sample.

from the sample.

To correct for this incompleteness bias, we have used the same correction as given in Masters et al. (2008). They derived it from Monte Carlo simulations of the difference between the expected and observed magnitudes.

Cluster size bias

Two further corrections need to be applied to deal with the assumption that all galaxies in the cluster are at the same distance. This is appropriate only when the diameter of the cluster is negligible compared to its distance. These two corrections are very small compared to the other corrections.

Mean distance to a cluster

Since we are dealing with the distance modulus rather than linear distance, a small fixed bias arises from the fact that the log of the average of the distance is not equal to the average of the log of the distance. Table 1 in Masters et al. (2008) provides the correction values using the assumption of a line-of-sight extent of one Abell radius for the *in* sample and two Abell radius for the *in*+ sample.

Sample incompleteness

Dimmer galaxies are preferentially observed on the near side of the cluster. The magnitude of these galaxies will be overestimated due to the assumption that all galaxies in any given cluster are at the same distance (mean distance to the cluster). It depends mainly on the incompleteness bias-correction, so we also used the same values as in Masters et al. (2008).

Cluster peculiar velocity

The peculiar velocity needs to be estimated for each cluster before combining these clusters into a global TF relation. We use the same offset (due to the cluster peculiar velocity) as Masters et al. (2006; 2008).

Malmquist bias

Following Giovanelli et al. (1997a) and Masters et al. (2008) I adopt no correction for this effect as it is negligible for this sample.

2.5 Fitting and scatter

Different authors have used different fitting procedures to derive the final parameters of the TF relation. The inverse TF was suggested by Kraan-Korteweg et al. (1986) to overcome the Malmquist bias. Giovanelli et al. (1997a) used the minimization of χ^2 method to determine the direct, inverse, and bivariate forms of the linear TF relation. In Pizagno et al. (2007), the maximum likelihood method was used to estimate the slope a, intercept b, and intrinsic scatter ϵ_{int} of the TF relation. Here we are interested in the bivariate fit case, where errors in both x and y are taken into consideration. We therefore use the linear form:

$$y(x) = a_{bi} + b_{bi}x, \tag{2.12}$$

via minimization of χ^2

$$\chi^2 = \sum_{i=1}^{N} [\frac{y_i - y(x_i; a_{bi}, b_{bi})}{\epsilon_i}]^2. \tag{2.13}$$

The error used in the computation is defined as $\epsilon_i = [(\epsilon_{x,i}b_{bi})^2 + \epsilon_{y,i}^2 + \epsilon_{int}^2 + \mathrm{cov}_{xy}]^{1/2}$, where cov_{xy} represents the covariance between the errors in x and y which is not significant in our case.

2.5.1 The isophotal NIR TF relation

After applying all of the above detailed bias corrections, and applying the bivariate fitting mechanism to the 888 calibrator galaxies, the final TF relations have the form:

$$M_J - 5\log h = -21.059 - 9.268(\log W - 2.5), \tag{2.14a}$$
$$M_H - 5\log h = -21.805 - 9.296(\log W - 2.5), \tag{2.14b}$$
$$M_{K_s} - 5\log h = -21.966 - 10.376(\log W - 2.5). \tag{2.14c}$$

Table 2.4 presents the fitting parameters derived from both isophotal magnitude (this work) and total magnitude from Masters et al. (2008). Figure 2.7 shows the final global TF data in the J, H, and K_s-bands for both the direct and the bivariate forms. In this figure, the direct fit is shallower than the bivariate fit.

Band	This thesis				Masters et al. (2008)			
	a_{iso}	b_{iso}	ϵ_a	ϵ_b	a_{tot}	b_{tot}	ϵ_a	ϵ_b
J-band	−21.047	−9.387	0.018	0.114	−20.999	−9.070	0.017	0.116
H-band	−21.793	−9.433	0.018	0.115	−21.833	−9.016	0.016	0.106
K_s-band	−21.959	−10.523	0.018	0.120	−22.030	−10.017	0.015	0.098

Table 2.4: Parameters of bivariate fit after all corrections derived from both isophotal (this work) and total magnitude (Masters et al. 2008).

Figure 2.7 also shows that the scatter in the TF relation increases with decreasing rotation width. The relation used in Giovanelli et al. (1997a), Masters et al. (2008) to parameterize the scatter is adopted

$$\sigma = a + b(\log W - 2.5) \tag{2.15}$$

The total scatter is calculated and shown for the J, H, and K_s-bands in Figure 2.8 as a

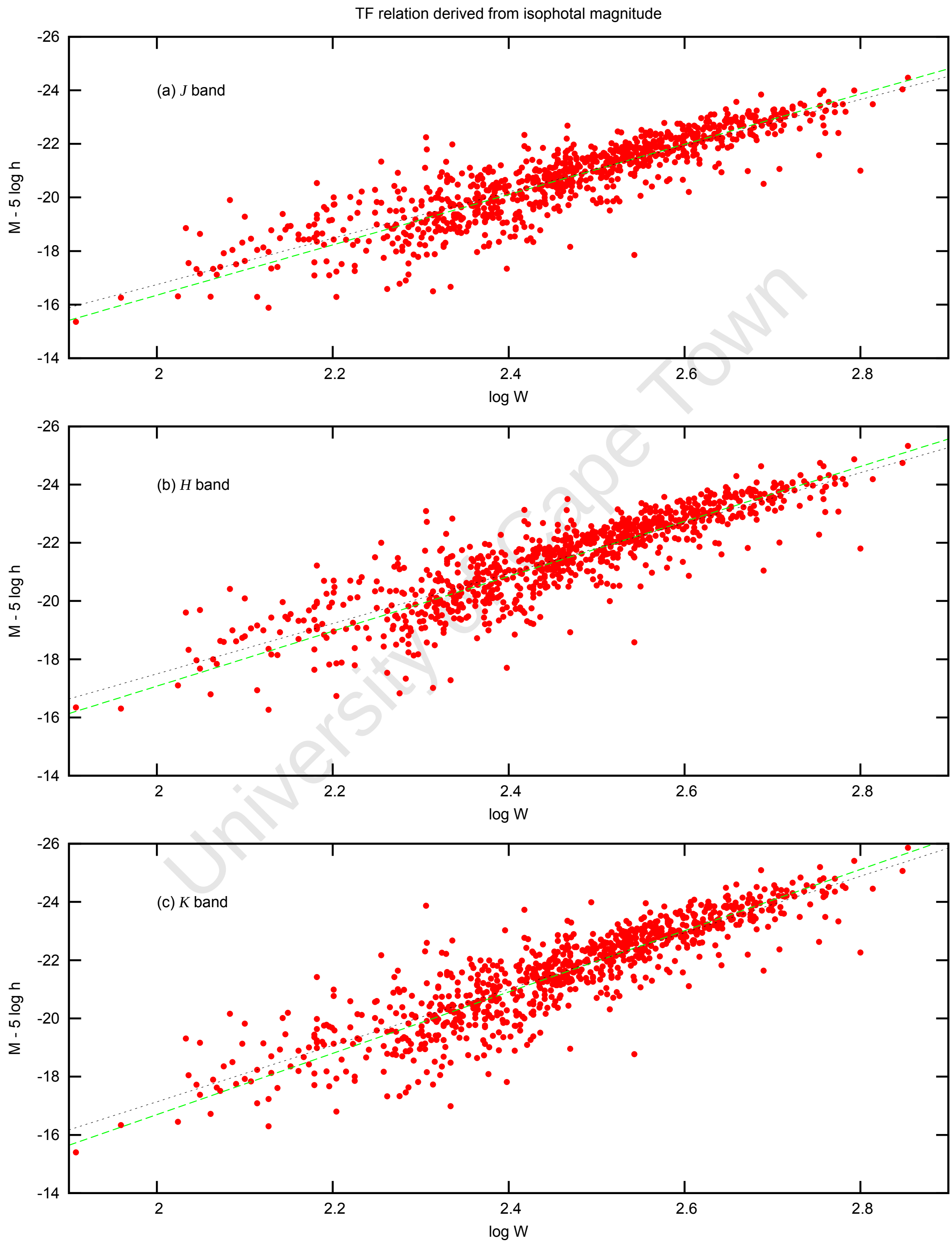

Figure 2.7: Global TF relation for the (a) J-band, (b) H-band, and (c) K_s-band (in+ sample) derived from the isophotal magnitude. The dashed line in all panels shows the respective bivariate fit to the data. The dotted lines show the direct fit.

function of the line-width.

The error on the isophotal magnitude (least source of error), as well as the error on the rotation width multiplied by the slope of the TF relation (expressed in magnitudes) are also displayed in Figure 2.8. A linear fit to the intrinsic scatter gives

$$\epsilon_{int,J} = 0.46 - 0.90(\log W - 2.5), \quad (2.16a)$$
$$\epsilon_{int,H} = 0.47 - 0.94(\log W - 2.5), \quad (2.16b)$$
$$\epsilon_{int,K_s} = 0.46 - 0.83(\log W - 2.5). \quad (2.16c)$$

In Masters et al. (2008) the intrinsic scatter is given by:

$$\epsilon_{int,J} = 0.39 - 0.78(\log W - 2.5), \quad (2.17a)$$
$$\epsilon_{int,H} = 0.38 - 1.14(\log W - 2.5), \quad (2.17b)$$
$$\epsilon_{int,K_s} = 0.35 - 1.17(\log W - 2.5). \quad (2.17c)$$

The intrinsic scatter, in magnitude units, is crucial to understand the errors on both distances and peculiar velocities derived from a TF relation. The intrinsic scatter in both the "isophotal" and "total" methods are very close, because the calibration sample of galaxies is hardly affected by foreground dust of the Milky Way. Equations 2.16 & 2.17 show that the intrinsic scatter is smaller in the total magnitude relation when using only the very large galaxies ($\log W > 2.5$) while for small galaxies ($\log W < 2.5$) the "isophotal" magnitude relation shows less scatter. This conclusion further substantiates that the use of the "isophotal" magnitude relation is preferable for all-sky surveys, which include both large and small galaxies.

2.6 Conclusion

I have presented the derivation of the NIR "isophotal" TF relation, which is optimally suited to derive the flow field in or close to the Zone of Avoidance. Using the isophotal magnitudes, I recalibrated the TF-relation in the J, H, and K_s-bands using the Masters et al. (2008) sample and the Riad et al. (2010) Galactic absorption corrections. I correct for the dependence of the TF relation on morphological type. Appropriate corrections to all biases (*i.e.* incompleteness bias, cluster size bias, cluster peculiar velocity, and other sources) are obtained. I also provide corrections to the magnitude both Galactic and internal for extinction, as well as a cosmological k-correction. I use the bivariate fit method, where errors in both sets of data are taken into consideration. Minimization of χ^2 was used to provide the final parameters. Because the calibration sample is located far from the Galactic Plane, no significant change in the TF scatter compared to previous studies has been seen. This suggests that their is no major problem in general to use isophotal TF relations.

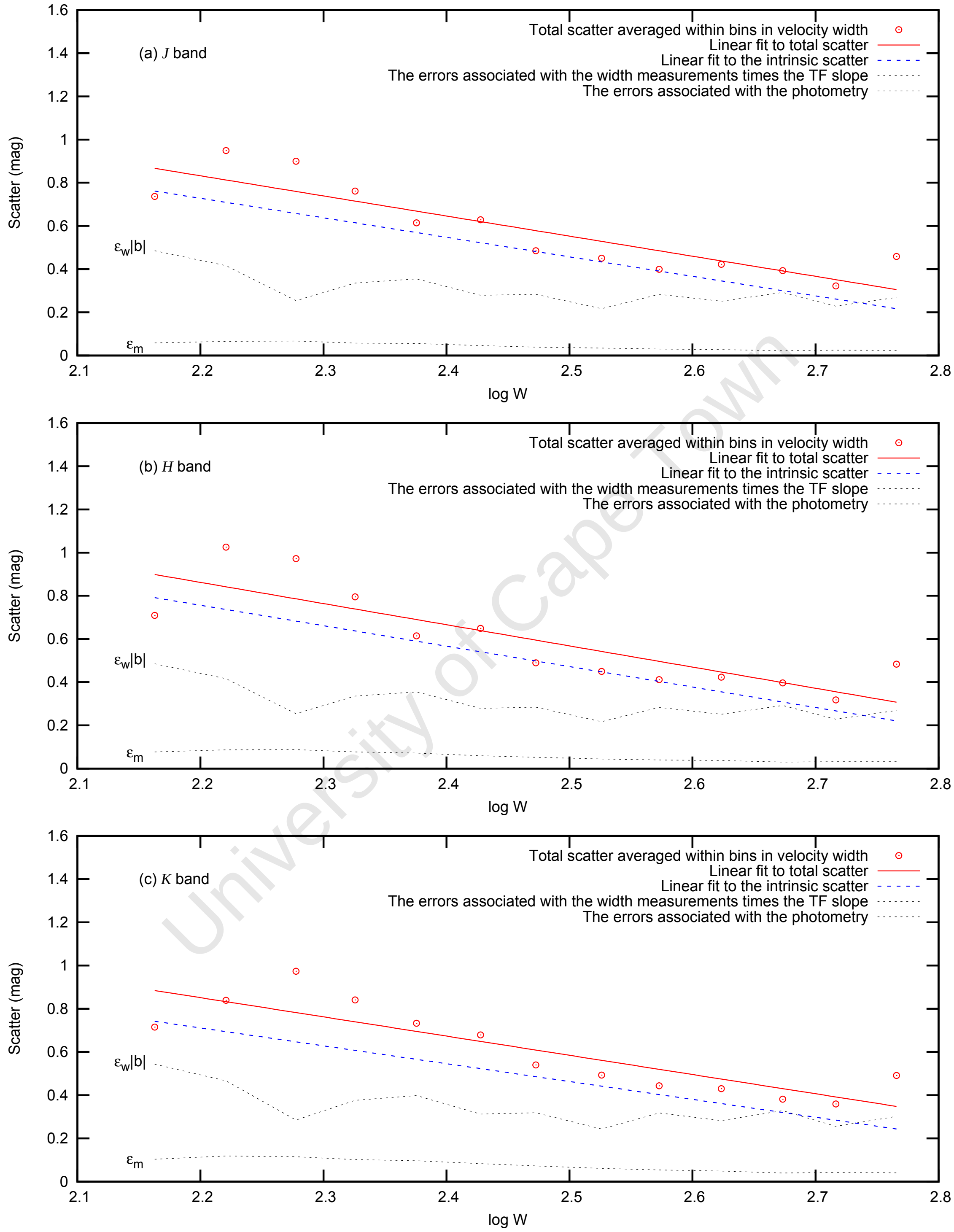

Figure 2.8: Scatter in the (a)J-band, (b)H-band, and (c)K_s-band. Unfilled circles present the total scatter averaged within bins in velocity width. Linear fit to the total scatter is shown as solid line and the dashed line shows the linear fit to the intrinsic scatter. The dotted lines present the error on the isophotal magnitude and the error on the rotation width multiplied by the slope

I analyze the total and intrinsic scatter of the final TF relations in detail. By comparison of the intrinsic scatter in both the "isophotal" and "total" relations I demonstrate that the scatter becomes lower in the "isophotal" relation at low line-width. The importance of the intrinsic scatter in the TF relations derived here, comes from their contribution to the error in both distances and peculiar velocities (Chapter 4).

Chapter 3

Inclination Correction

While efforts have been made to correct for the effect of dust extinction on the photometric properties of galaxies (magnitude and major axis), the effect of dust extinction on the geometrical properties of galaxies (axial ratio) has mostly been ignored. The inclination or the axial ratio of spirals (b/a) is an important parameter in the TF analysis because the actual sample selection and the correction of line-widths and magnitudes depend on inclination. The effect of foreground dust extinction on the shape of spiral galaxies can be severe in the ZoA, hence the determination of the actual "intrinsic" axial ratio b/a hence is crucial to our analysis. I therefore examine in this chapter the effect of the foreground dust on the shape of the observed spiral galaxies.

3.1 Introduction

Spiral galaxies consist of a disk plus a bulge. The disk is almost flat and contains large amounts of dust, while the bulge is rounder and tends to be dust-poor. The effect of dust within the galaxy on the derived photometric parameters has been investigated by several authors (e.g., Han 1992a, Giovanelli et al. 1994, Masters et al. 2003, Tuffs et al. 2004, Driver et al. 2007, Masters et al. 2010, Pastrav et al. 2013a;b). In this chapter I analyze another type of dust-induced change, i.e, the change in the shape of the background spirals due to the foreground dust in the Milky Way.

The effect of foreground dust extinction on the isophotal radius and magnitude of galaxies (elliptical as well as spirals) has been investigated extensively by Cameron (1990) and more recently by Riad et al. (2010), see also Chapter 2. These studies were restricted to analyze the effect of dust on the major axis but not the minor axis, and therefore not the change in the apparent shape (axial ratio).

In the ZoA where the dust extinction can be high, such an effect can be significant. The motivation for studying this effect is twofold. The first reason is to avoid a systematic bias in the sample selections which are constrained by inclination. The second reason is the dependence of the TF parameters on the inclination such as the correction of the HI line-width and the correction of the magnitude due to the internal extinction, as discussed below.

Inclination-dependent parameters in the TF relation

Two parameters in the TF depend on the inclination of a spiral galaxy. The first one is the HI spectral data. To derive the maximum rotational velocity the observed line-width needs to be corrected to edge-on orientation. According to Springob et al. (2007) this is:

$$W = [\frac{w_{50} - \Delta_s}{1+z} - \Delta_t]\frac{1}{\sin i}. \tag{3.1}$$

The inclination i is derived from the J-band ellipticity $\epsilon_J = 1 - (b/a)_J$ via:

$$\cos^2 i = \frac{(1-\epsilon)^2 - q_0^2}{1 - q_0^2} \tag{3.2}$$

(e.g., Giovanelli et al. 1997a) where q_0 is the intrinsic axial ratio of the galaxy ($q_0 = 0.13$ for Sbc and Sc, and $q_0 = 0.2$ for other types). The second set of data are the NIR magnitudes, where we use the equation adopted by a number of authors (e.g., Giovanelli et al. 1994, Tully et al. 1998, Masters et al. 2003) to correct for the internal extinction, which depends on the axial ratio as follows:

$$I_\lambda = \gamma \log(a/b). \tag{3.3}$$

Inaccurate inclinations of spiral galaxies will create a systematic bias in both corrected line-width and absolute magnitude, and therefore in the derived peculiar velocities.

Systematic selection effect

Inclined spiral galaxies are preferentially used in the TF analysis to minimize the corrections in the line-width. Most TF surveys apply a certain limit on the axial ratio for selecting spirals. The 2MTF project uses only galaxies with $b/a < 0.5$ (Masters et al. 2008, Masters 2008, Hong et al. 2013a) while Williams (2011) increases that limit to include galaxies with $b/a < 0.7$. Inaccurately derived inclinations will bias the survey sample, and therefore increasing the uncertainty in the analysis. This effect is dependent on the dust column density along the line-of-sight to the galaxies. It should therefore be explored how the foreground dust changes the apparent axial ratio and what its net effect may be on the TF peculiar velocity.

To avoid any systematic errors in our analysis due to the axial ratio, I quantify the effect of the foreground extinction on the axial ratio with the aim to construct a correction model. To study this effect three independent methods have been applied to different galaxy samples. In the following sections, I discuss these three methods in detail. Section 3.2 presents the first method which is based on a sample of galaxies drawn from the 2MASS Large Galaxy Atlas (LGA) (Jarrett et al. 2003) which will be absorbed artificially. The second method is based on fully simulated galaxies and its results are described in Section 3.3. In Section 3.4 I compare galaxies common to both a deep and a shallow survey to analyze this effect.

3.2 Sample of galaxies from the 2MASS LGA

In this section I use a sample of 54 spirals (see Table 3.1) extracted from the 2MASS LGA. The galaxies have been artificially absorbed, similar to Cameron (1990) and Riad et al. (2010) but for the full 2-dimensional data set. I have measured the surface brightness profile using the **ellipse** task in the **stsdas** package for both the major and minor axis by using the ellipticity as a free parameter.

Figure 3.1 as an example shows the surface brightness profile of NGC1515 (Sbc) to explain the method used. It has an intrinsic axial ratio of $b/a = 0.34$ in the J-band. In Fig. 3.1, the surface brightness is plotted against the major axis in the top panel and the minor axis in the bottom panel. The 3σ background noise of 20.09, 19.34, and 18.55 mag arcsec^{-2} in the J, H, and K_s-bands, respectively (Jarrett et al. 2000) have been used to measure the isophotal limit of the major and minor axis as shown by the solid black line. The projection of the intercept between the solid black line and the light profile on the x-axis gives the intrinsic major axis a° (top panel) and minor axis b° (bottom panel). I set the simulation limits to $A_J = 0.0 - 3.0$ mag. The inward displacements represented by the dotted lines in Fig. 3.1 show the simulated extinction levels A_J in mag. For each level of extinction the major and minor axes have been measured from the intercept of the dotted line and the light profile. As a function of extinction I calculate the ratios

$$f(a) = a^\circ/a, \tag{3.4a}$$

$$f(b) = b^\circ/b, \tag{3.4b}$$

where a°, a, b°, and b are the intrinsic and absorbed major and minor axes. The functions $f(a)$ and $f(b)$ are plotted against different values of simulated extinction A_J (top and middle panels) in Fig. 3.2. The bottom panel shows the ratio of $f(b)/f(a)$ against A_J, which clearly demonstrates that the axial ratio (b/a) increases with dust extinction (i.e. galaxies appear more rounder). Using the formula

$$f(R) = 10^{c(A_\lambda)^d} \tag{3.5}$$

given by Cameron (1990), where c and d are fitted parameters, I fitted the data as shown in Fig. 3.2 by the dashed line. The galaxy NGC1515, with an intrinsic axial ratio of $b/a = 0.34$ in the J-band would appear to have $b/a = 0.48$ if seen through 1 mag of extinction, respectively $b/a = 0.62$ if seen through 2 mag of extinction. For an extinction of $A_J \geq 1\overset{\mathrm{m}}{.}2$ this

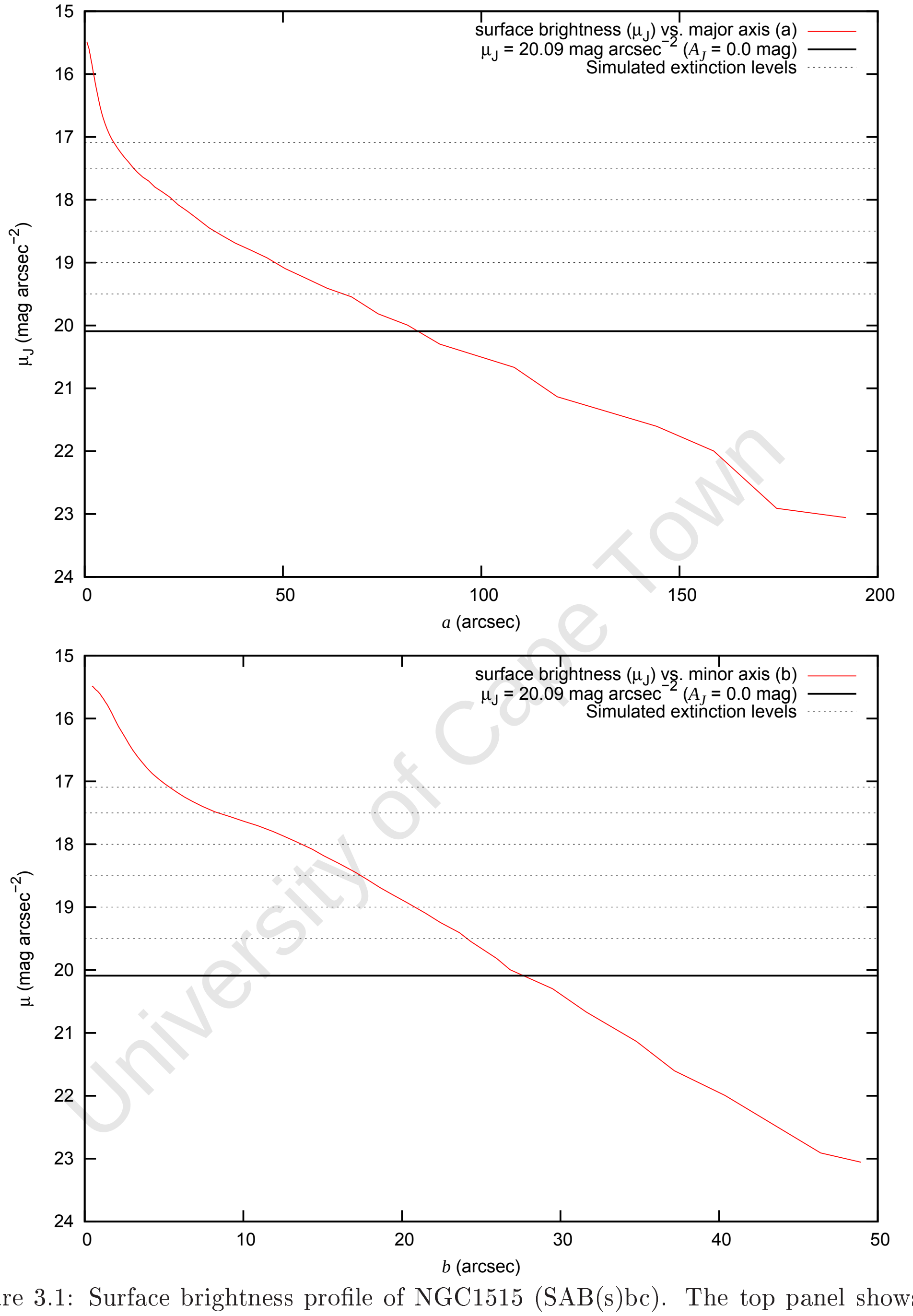

Figure 3.1: Surface brightness profile of NGC1515 (SAB(s)bc). The top panel shows the light profile against the major axis a. The bottom panel shows the light profile against the minor axis b. Note the different scales for major (top) and minor (bottom) axes. In all panels the solid black line shows the typical 3σ background noise of 20.09 mag arcsec^{-2} in the J-band, which is used to measure the intrinsic major or minor axis. The dotted lines show different levels of simulated extinction.

edge-on galaxy would be excluded from the 2MTF survey.

To analyze this effect statistically, this procedure was followed for all the other galaxies in our selected LGA sample. The 54 spiral galaxies have different morphological types and axial ratios, and contain both barred and unbarred galaxies (Table 3.1).

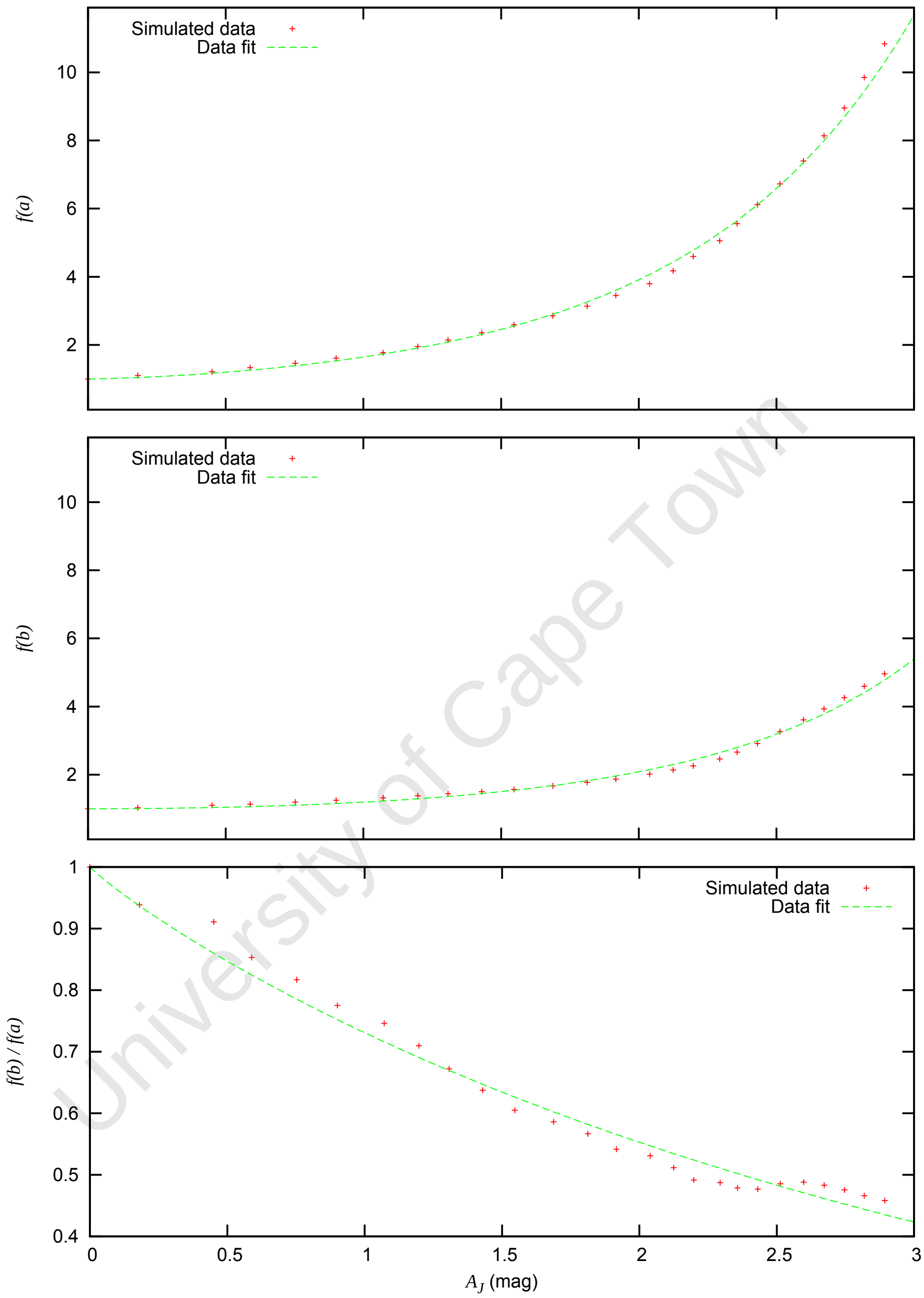

Figure 3.2: NGC1515(SAB(s)bc) galaxy major axis correction due to the foreground extinction $f(a)$ in the top panel, the minor axis correction due to the foreground extinction $f(b)$ in the middle panel, and the axial ratio correction due to the foreground extinction $f(b)/f(a)$ in the bottom panel. The dashed lines in all panels show the fit to the data.

Table 3.1: The sample of galaxies used. The columns are galaxy name, morphological type, axial ratio, the effective mean surface brightness and the central surface brightness for J, H, and K_s.

Galaxy	Morphology	$(b/a)_J$	$\mu_{J,e}$	$\mu_{J,c}$	$(b/a)_H$	$\mu_{H,e}$	$\mu_{H,c}$	$(b/a)_{K_s}$	$\mu_{K,e}$	$\mu_{K,c}$
M65	SAB(rs)a	0.28	17.27	14.30	0.30	16.57	13.58	0.32	16.32	13.31
M88	SA(rs)b	0.46	17.38	14.37	0.42	16.61	13.57	0.44	16.33	13.23
M94	SA(r)ab	0.79	15.56	12.75	0.75	14.87	12.01	0.79	14.55	11.70
M98	SAB(s)ab;HII	0.28	18.19	14.56	0.30	17.44	13.71	0.24	17.15	13.38
M101	SAB(rs)cd	0.83	19.59	16.14	0.89	18.94	15.43	0.99	18.69	15.13
M106	SAB(s)bc;LINER	0.45	17.82	14.39	0.47	17.11	13.70	0.49	16.88	13.39
NGC210	SA(s)b	0.56	17.41	15.32	0.58	16.36	14.53	0.52	15.86	14.21
NGC488	SA(r)b	0.71	18.09	14.82	0.75	17.52	14.06	0.81	17.10	13.81
NGC986	SB(rs)b	0.57	18.22	15.61	0.57	17.54	14.84	0.57	17.21	14.37
NGC1073	SB(rs)c	0.72	20.17	17.82	0.72	19.43	17.21	0.72	19.34	16.99
NGC1187	SB(r)c	0.59	18.99	15.54	0.61	18.23	14.66	0.55	17.93	14.28
NGC1247	Sbc	0.20	17.71	16.17	0.18	16.85	15.27	0.18	16.49	14.89
NGC1337	SA(s)cd	0.38	19.43	18.04	0.36	18.77	17.28	0.38	18.53	17.13
NGC1350	SB(r)ab	0.52	17.83	14.51	0.50	17.07	13.77	0.50	16.80	13.54
NGC1515	SAB(s)bc	0.34	17.89	15.81	0.36	17.10	14.96	0.40	16.82	14.96
NGC1532	SB(s)b;pec;sp	0.40	17.80	14.98	0.38	17.00	14.15	0.30	16.70	13.84
NGC1808	SAB(s:)b;Sy2	0.44	17.24	14.08	0.44	16.33	13.27	0.42	15.81	12.77
NGC3003	SBbc	0.34	19.34	17.80	0.30	18.70	17.07	0.30	18.32	16.69
NGC3184	SAB(rs)cd	0.99	19.75	16.74	0.99	19.08	16.05	0.85	18.84	15.73
NGC3198	SB(rs)c	0.39	19.06	16.70	0.41	18.37	15.80	0.35	18.14	15.37
NGC3326	Sa	0.91	17.32	16.21	0.83	16.46	15.49	0.88	15.98	15.12
NGC3338	SA(s)c	0.51	18.95	16.53	0.55	18.32	15.81	0.55	18.03	15.57

Continued on next page

Galaxy	Morphology	$(b/a)_J$	$\mu_{J,e}$	$\mu_{J,c}$	$(b/a)_H$	$\mu_{H,e}$	$\mu_{H,c}$	$(b/a)_{K_s}$	$\mu_{K,e}$	$\mu_{K,c}$
NGC3365	Scd	0.24	19.76	18.36	0.24	19.01	17.68	0.23	18.87	17.38
NGC3389	SA(s)c	0.46	19.11	17.55	0.40	18.45	16.83	0.46	18.20	16.57
NGC3511	SAB(s)c	0.28	18.92	16.64	0.30	18.18	15.82	0.32	17.87	15.52
NGC3614	SAB(r)c	0.67	19.63	17.75	0.75	18.89	17.04	0.77	18.72	16.79
NGC3877	Sc	0.24	17.93	15.92	0.24	17.15	15.10	0.24	16.83	14.71
NGC3898	SA(s)ab;LINER	0.55	16.98	14.14	0.55	16.25	13.38	0.59	16.00	13.19
NGC4096	SAB(rs)c	0.28	18.70	16.45	0.30	17.95	15.74	0.30	17.67	15.44
NGC4206	SA(s)bc	0.20	19.09	17.51	0.20	18.43	16.81	0.20	18.00	16.56
NGC4216	SAB(s)b	0.18	16.98	14.00	0.18	16.23	13.22	0.18	15.95	12.97
NGC4314	SB(rs)a	0.68	17.67	15.09	0.68	16.91	14.35	0.68	16.70	14.12
NGC4330	Scd	0.16	19.09	18.05	0.14	18.23	17.09	0.16	17.90	16.71
NGC4388	SA(s)b:;sp	0.32	17.81	16.02	0.28	16.98	15.08	0.32	16.58	14.59
NGC4448	SB(r)ab	0.32	17.53	15.44	0.32	16.84	14.69	0.32	16.60	14.41
NGC4517	SA(s)cd:;sp	0.16	18.79	17.66	0.14	17.95	16.72	0.16	17.60	16.34
NGC4527	SAB(s)bc	0.32	17.36	14.18	0.32	16.38	13.29	0.34	15.97	12.89
NGC4536	SAB(rs)bc	0.48	18.40	14.68	0.50	17.38	13.73	0.52	17.02	13.26
NGC4559	SAB(rs)cd	0.41	19.22	17.40	0.45	18.53	16.72	0.47	18.30	16.48
NGC4569	SAB(rs)ab;Sy	0.44	18.08	13.85	0.38	17.39	13.18	0.40	17.08	12.83
NGC4941	SAB(r)ab;Sy2	0.51	18.50	15.05	0.51	17.77	14.30	0.63	17.53	14.07
NGC5135	SB(l)ab;Sy2	0.49	17.33	15.51	0.49	16.77	14.65	0.49	15.94	14.17
NGC5170	SA(s)c;sp	0.26	17.74	15.32	0.24	16.90	14.47	0.26	16.66	14.22
NGC5371	SAB(rs)bc	0.68	18.79	15.29	0.66	18.09	14.53	0.70	17.84	14.30
NGC5529	Sc	0.20	17.95	16.63	0.20	17.01	15.66	0.16	16.58	15.25
NGC5566	SB(r)ab	0.53	16.96	14.20	0.53	16.17	13.47	0.53	15.91	13.24

Continued on next page

Galaxy	Morphology	$(b/a)_J$	$\mu_{J,e}$	$\mu_{J,c}$	$(b/a)_H$	$\mu_{H,e}$	$\mu_{H,c}$	$(b/a)_{K_s}$	$\mu_{K,e}$	$\mu_{K,c}$
NGC5777	Sbc	0.20	17.41	15.80	0.20	16.44	14.88	0.20	15.96	14.40
NGC5861	SAB(rs)c	0.55	18.82	17.21	0.55	18.08	16.36	0.65	17.79	16.05
NGC5965	Sb	0.28	17.70	15.74	0.30	16.86	14.99	0.32	16.60	14.73
NGC5985	SAB(r)b;Sy1	0.57	18.96	16.62	0.51	18.29	15.89	0.51	18.02	16.34
NGC5987	Sb	0.43	17.85	15.55	0.45	17.05	14.81	0.43	16.73	14.49
NGC6015	SA(s)cd	0.59	18.87	17.47	0.55	18.16	16.80	0.49	17.92	16.52
NGC6925	SA(s)bc	0.34	17.39	14.75	0.34	16.60	13.99	0.36	16.30	13.66
NGC7184	SB(r)c	0.26	18.09	15.58	0.30	17.45	14.84	0.34	17.09	14.59

I will now investigate the correlations between the change in the axial ratio and the properties of the galaxies, such as, inclination or type, to construct a correction model. The central surface brightness μ_c and the half-light effective mean surface brightness μ_e are used as indicator of morphological type (Jarrett et al. 2003).

3.2.1 Correction based on μ_c

Following the recipe given by Riad et al. (2010) I include the central surface brightness μ_c in the J, H, and K_s-bands to optimize the correction model. The correction equations become

$$f(R, \mu_c) = 10^{c(\mu_c)(A_\lambda)^{d(\mu_c)}}, \tag{3.6}$$

where

$$c(\mu_c) = c_0 \exp(\mu_c \times c_1), \tag{3.7}$$

$$d(\mu_c) = d_0 \exp(\mu_c \times d_1). \tag{3.8}$$

The values of c_0, c_1, d_0, and d_1 in the J, H, and K_s-bands are the fitting parameters. The mean value for each parameter derived from all galaxies is shown in Table 3.2.

Param.	J	H	K_s
c_0	−0.0046	−0.0120	−0.0221
c_1	0.1903	0.1392	0.1149
d_0	4.4303	2.3116	1.4236
d_1	−0.0668	−0.0291	−0.0053

Table 3.2: The fitting parameters of the correction based on the central surface brightness μ_c

Figures 3.3, 3.4 and 3.5 show the axial ratio correction for all galaxies in our sample in the J, H, and K_s-bands, respectively. The sample is subdivided into classes of central surface brightness (as proxy for morphology). Panels from top to bottom reflect the SB ranges of $\mu_c < 15$, $15 < \mu_c < 16$, $16 < \mu_c < 17$ and $17 < \mu_c < 19$. The left panels show highly-inclined galaxies of axial ratio $b/a < 0.4$ and the right panels show less-inclined galaxies of axial ratio $b/a > 0.4$.

The effect on the observed (obscured) shape is stronger for intrinsically highly-inclined galaxies than the less-inclined galaxies in all bands. Note the different A_λ ranges for the J, H, and K_s-bands. The correction for the less-inclined galaxies always lies above $0.6(b/a)_{int}$ while the correction for highly-inclined galaxies can reach $0.2(b/a)_{int}$. The dependence of the correction on the morphological type needs larger samples for quantification.

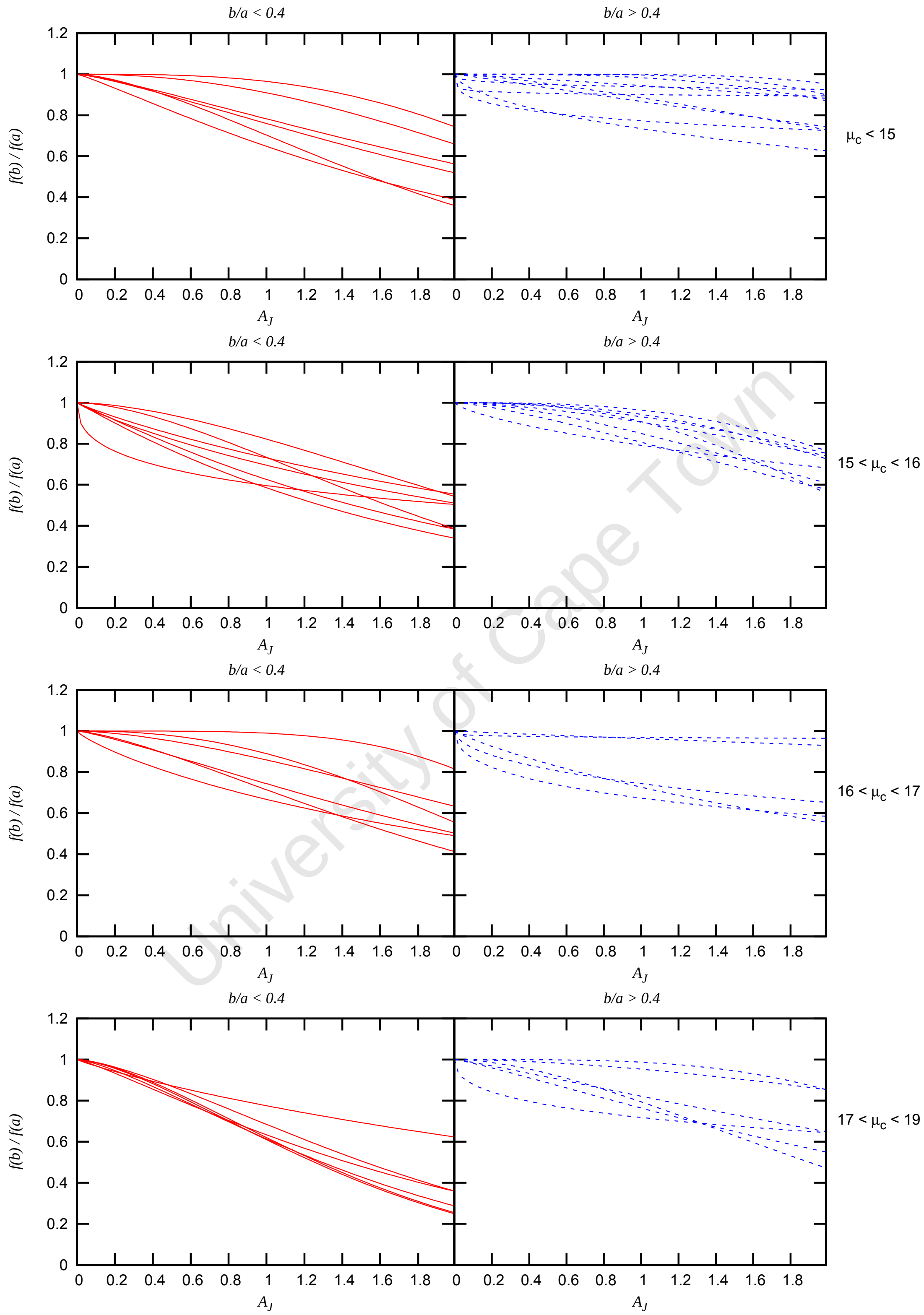

Figure 3.3: Axial ratio correction $f(b)/f(a)$ based on μ_c in the J-band subdivided as a function of their central surface brightness (top to bottom) and intrinsic inclination (left to right) versus the foreground extinction.

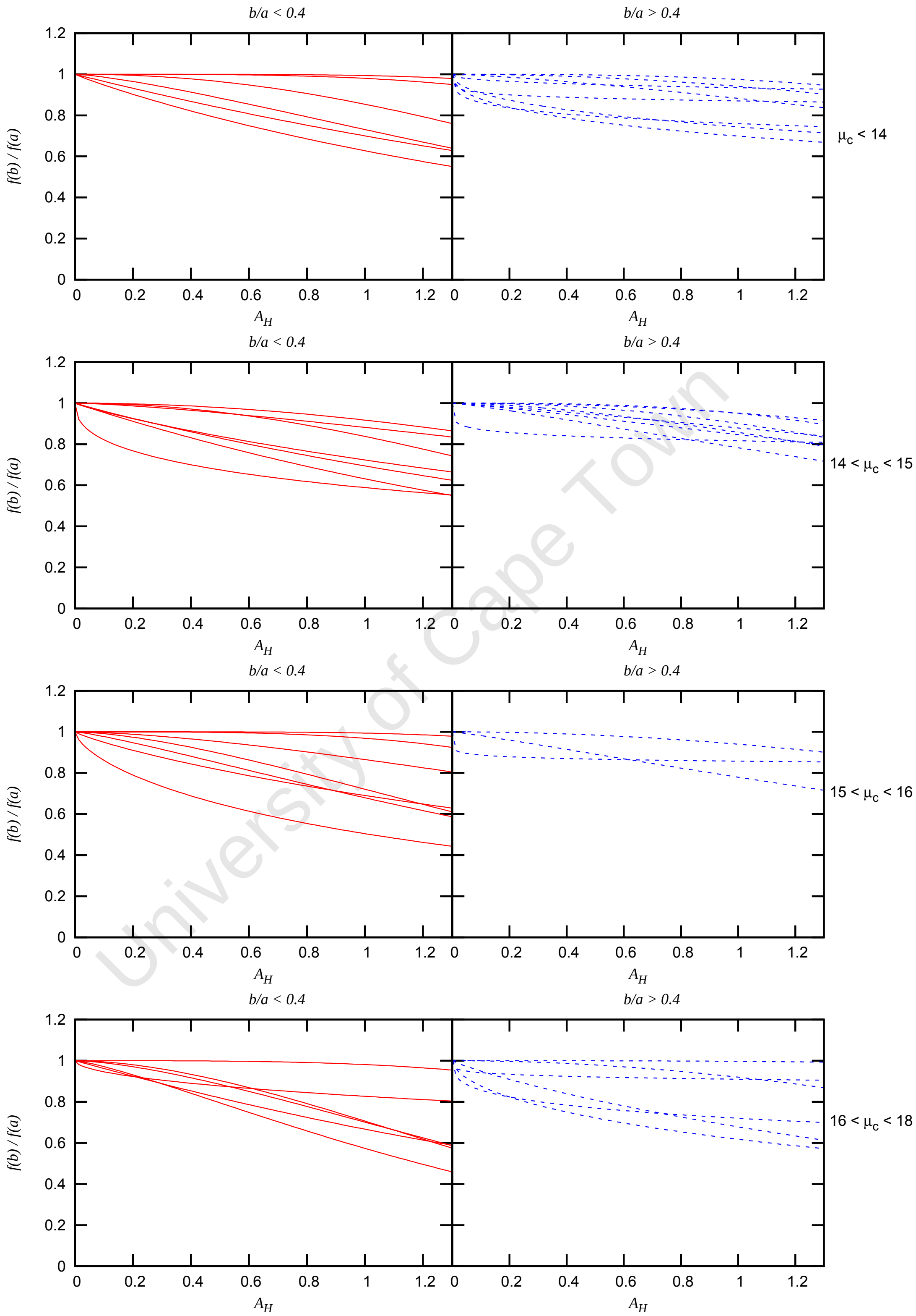

Figure 3.4: Axial ratio correction $f(b)/f(a)$ based on μ_c in the H-band subdivided as a function of their central surface brightness (top to bottom) and intrinsic inclination (left to right) against the foreground extinction.

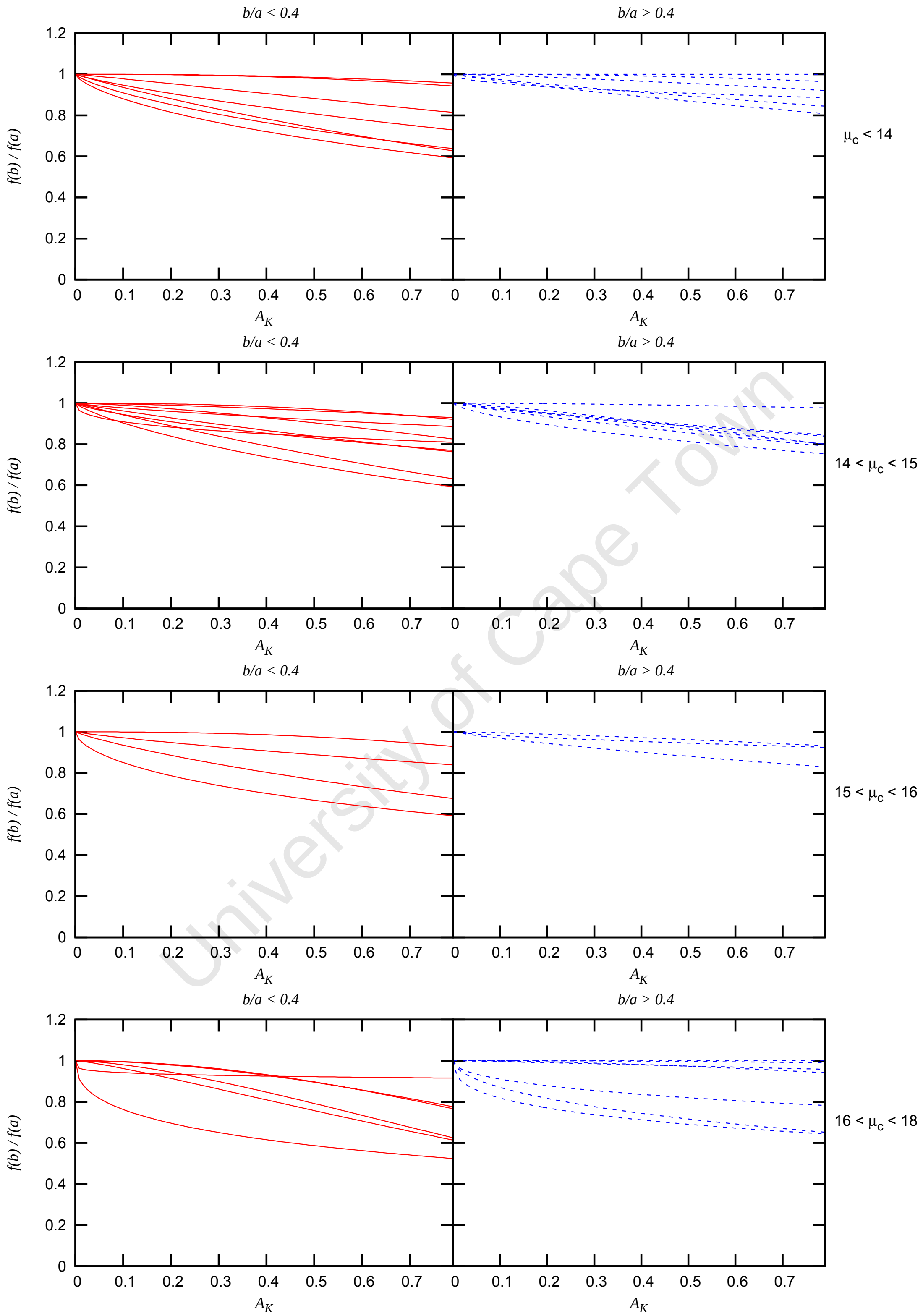

Figure 3.5: Axial ratio correction $f(b)/f(a)$ based on μ_c in the K_s-band subdivided as a function of their central surface brightness (top to bottom) and intrinsic inclination (left to right) against the foreground extinction.

3.2.2 Correction based on μ_e

The same method was applied using the half-light effective mean surface brightness μ_e. The correction equations are

$$f(R, \mu_e) = 10^{c(\mu_e)(A_\lambda)^{d(\mu_e)}}, \tag{3.9}$$

where

$$c(\mu_e) = c_0 \exp(\mu_e \times c_1), \tag{3.10}$$

$$d(\mu_e) = d_0 \exp(\mu_e \times d_1), \tag{3.11}$$

and c_0, c_1, d_0, and d_1 in J, H, and K_s-band are the fitting parameters, see Table 3.3 for the mean value for each parameter.

Param.	J	H	K_s
c_0	−0.0037	−0.0154	−0.0469
c_1	0.1793	0.1060	0.0562
d_0	4.2096	1.5685	2.1028
d_1	−0.0550	−0.0027	−0.0272

Table 3.3: The fitting parameters of the correction based on the μ_e

The parameters for the two methods (see Tables 3.2 and 3.3) show no significant change. This can also been demonstrated by comparing Figure 3.5 which shows the axial ratio correction $f(b)/f(a)$ based on μ_c in the K_s-band and Figure 3.6 which shows the correction but based on μ_e in the K_s-band.

3.3 Simulated galaxies

This section presents the second method used to quantify the effect of dust on the shape of spirals and is based on fully simulated galaxies. The advantage of using simulated galaxies is twofold: firstly it measures the effect on the same galaxy with foreground dust and without. Secondly we can test the correction model by applying it to the obscured galaxies and compare their axial ratio with the same galaxy before the obscuration. The IRAF *artdata* tasks (mkobject, mknoise, gallist, and starlist) were used in the simulations. I created artificial spiral galaxies (disk plus bulge) with different axial ratios b/a. The artificial galaxies were created to be similar to the 2MASS LGA galaxy M88 in the J and K_s-band. Figure 3.7 shows a 4×4 matrix of the simulated galaxies. The first column in Fig. 3.7 shows the unabsorbed galaxy with axial ratios of 0.2, 0.4, 0.6, and 0.8 from top to bottom. The columns from left to right show how the shape changes of the respective galaxies for increasing levels of absorption.

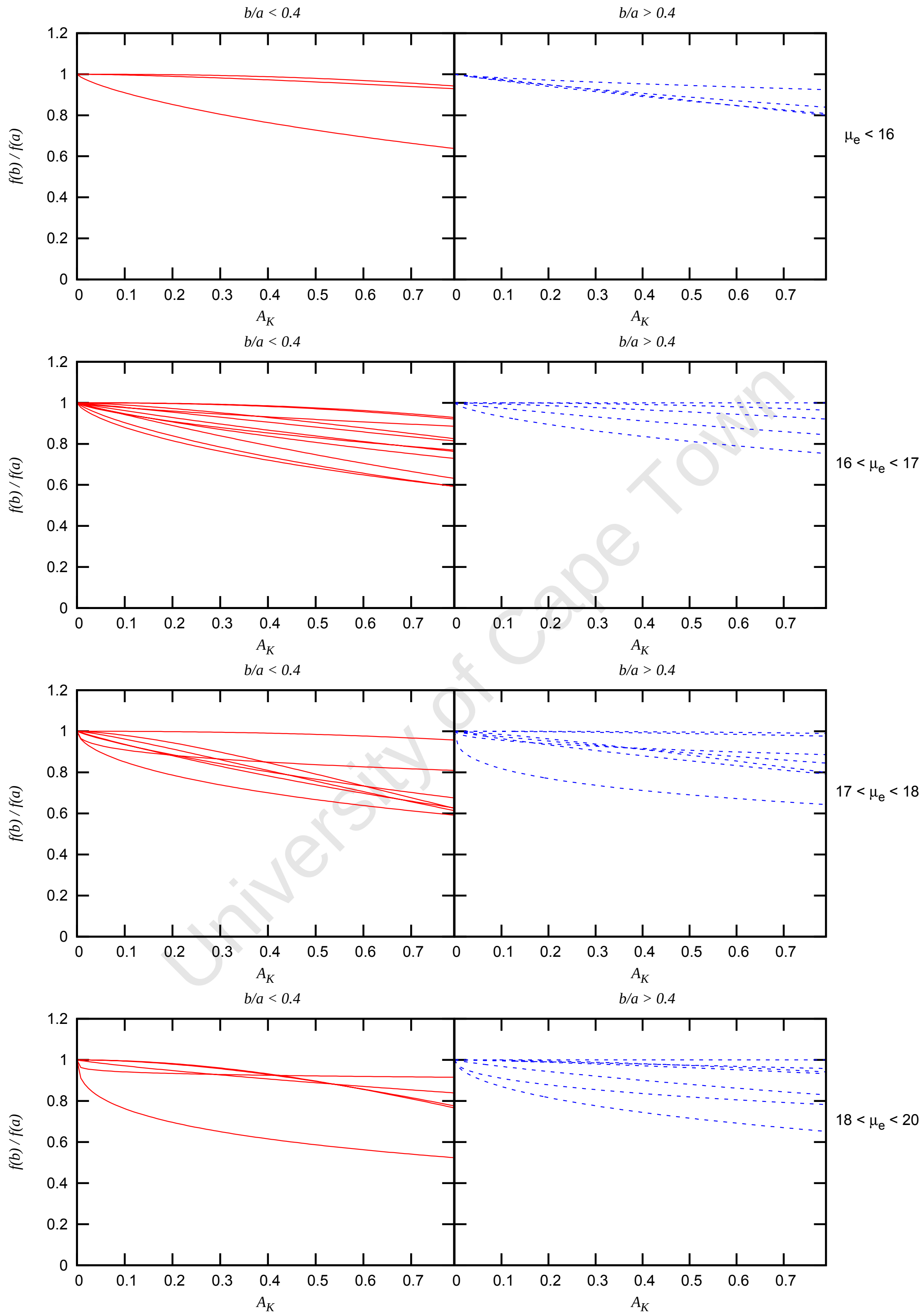

Figure 3.6: Axial ratio correction $f(b)/f(a)$ based on μ_e in the K_s-band subdivided as a function of their half-light effective mean surface brightness (top to bottom) and intrinsic inclination (left to right) against the foreground extinction.

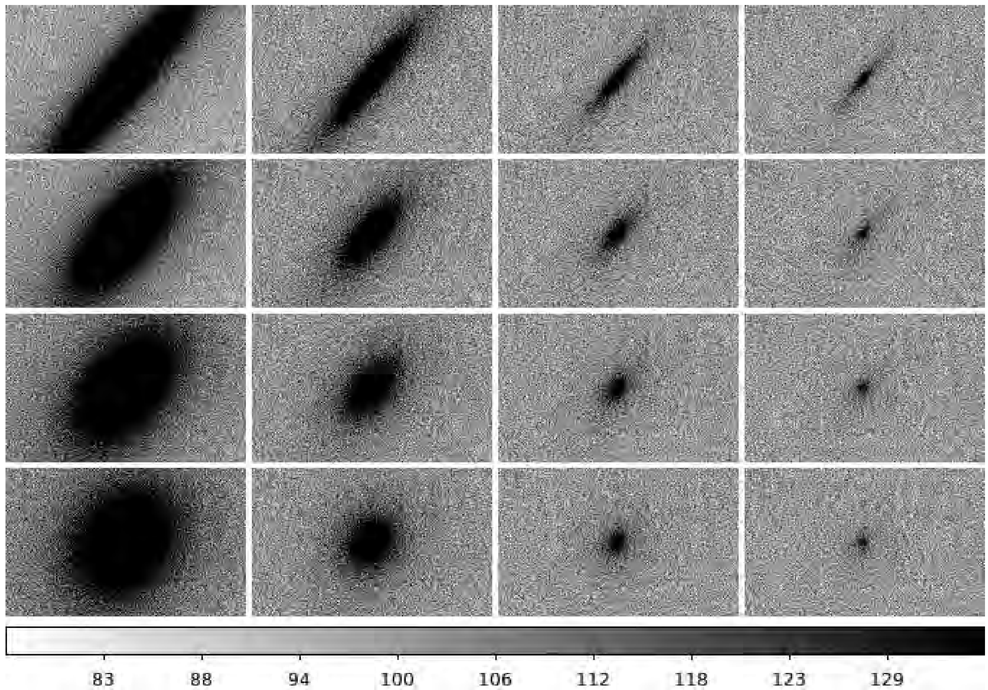

Figure 3.7: 4×4 Matrix of simulated galaxies. The left panels show the unabsorbed galaxies with intrinsic axial ratios ranging from 0.2, 0.4, 0.6, to 0.8 (top to bottom). From left to right the extinction increases (decreasing the flux).

3.3.1 Correction model

The 2-dimensional surface brightness profiles (using major and minor axes) for the simulated galaxies were measured using the IRAF **ellipse** task in the **stsdas** package. I used the same method as in Fig. 3.1 to determine the correction model, i.e, by creating inward displacements of the light profile, and to then measuring the axial ratio as a function of foreground extinction. I determined the correction model $f(R)$ by using Eq. 3.5. Only the average correction is shown here. Fitting parameters and axial ratios for each case are listed in Table 3.4.

b/a	0.20	0.40	0.60	0.80
c_J	-0.095	-0.076	-0.026	-0.004
c_{K_s}	-0.249	-0.164	-0.101	-0.037
d_J	1.564	1.430	1.964	2.558
d_{K_s}	0.957	0.887	0.704	0.318

Table 3.4: The parameters for simulated galaxies in both the J and K_s-bands.

The four cases for the J-band are plotted in Figure 3.8. Results in this section are consistent with those in section 3.2. These parameters in Table 3.4 and Fig. 3.8 show that both methods (LGA and simulated galaxies) provide the same result namely that the effect of dust on the shape is stronger for intrinsically highly-inclined galaxies than the less-inclined galaxies.

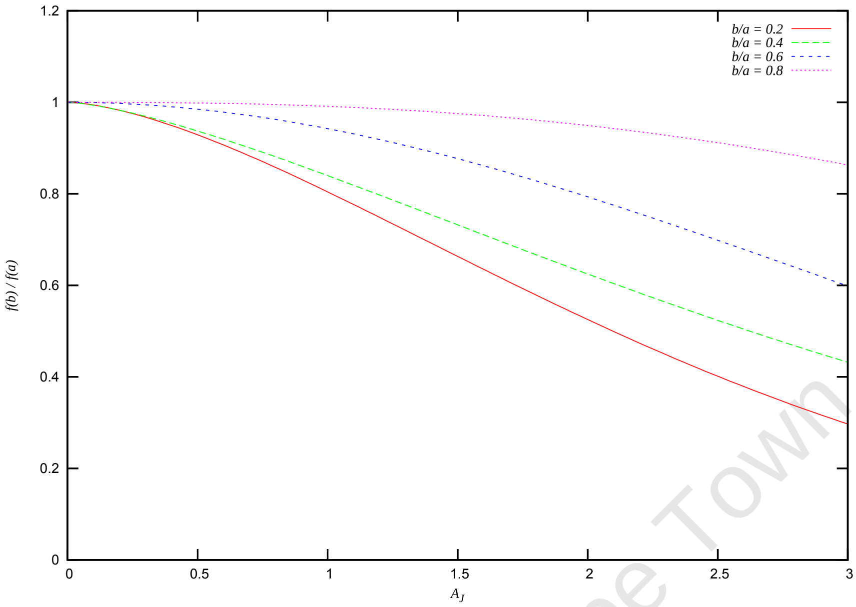

Figure 3.8: Axial ratio correction $f(b)/f(a)$ based on fully simulated galaxies in the J-band subdivided into four subsamples as a function of their intrinsic inclination plotted versus the foreground extinction.

3.3.2 Applying the correction model

After creating the simulated galaxies in Fig. 3.7, I test the correction parameters. For each single panel the IRAF **ellipse** task in the **stsdas** package is used to measure the axial ratio b/a at the 3σ isophote (i.e. ~ 3 times the background noise). After that I correct the artificially obscured axial ratios by inserting the derived parameters in Table 3.4 into equation 3.5.

To test whether the average model reproduces the intrinsic axial ratio from the absorbed value, I compare the corrected values with the intrinsic values. The ratio of the measured to true axial ratio as a function of extinction in the J-band is shown in Figs. 3.9 and 3.10 before and after applying the correction, respectively. Galaxies with axial ratio $b/a < 0.2$ are shown as squares, $0.2 < b/a < 0.4$ as circles, $0.4 < b/a < 0.6$ as upwards-pointing triangles and $0.6 < b/a < 0.8$ as downwards-pointing triangles. Figure 3.10 shows clear agreement between the corrected axial ratio and the intrinsic axial ratio except at the highest extinction.

Figures 3.11 & 3.12 show the same as Figures 3.9 & 3.10 for the K_s-band. Figs. 3.10 & 3.12 can be used to assess up to which extinction level the model can be satisfactorily corrected. The proposed correction model seems fairly reliable up to extinction levels of about $A_J = 3$ mag and $A_{K_s} = 1$ mag, which is about the same dust column density.

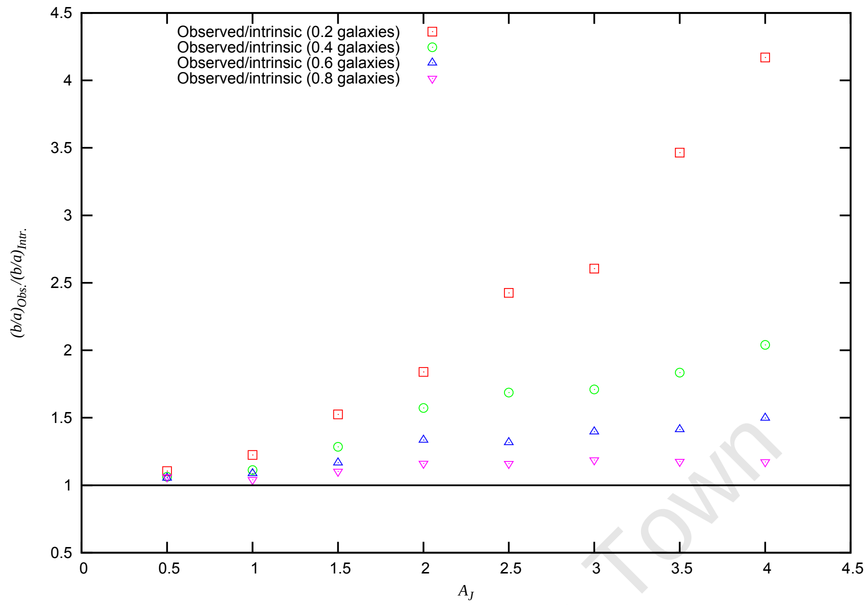

Figure 3.9: Absorbed axial ratio divided by intrinsic axial ratio in the J-band as a function of the foreground extinction. The unfilled squares, circles, upwards-pointing triangles and downwards-pointing triangles present galaxies of axial ratio $b/a < 0.2$, $0.2 < b/a < 0.4$, $0.4 < b/a < 0.6$, and $0.6 < b/a < 0.8$, respectively.

3.4 Comparison of shallow and deep observations

I finalize my analysis by applying the derived inclination correction model to a sample of 82 2MASX galaxies which also have independent photometry from deeper and more resolved data obtained with the IRSF (see Chapter 2). Here we applied (a) the average correction, (B) the correction based on the half-light effective mean surface brightness μ_{Je}, and (C) on the central surface brightness μ_c correction to the 2MASS data set. We assume that the IRSF axial ratio $(b/a)_{IRSF}$ is the true one as the IRSF survey is $2^{\rm m}$ deeper than the 2MASS survey in the K_s-band. Therefore, no corrections are applied to the IRSF data set. However, this is probably not true, because the galaxies in common lie deep in the ZoA and the IRSF images will also have been affected by absorption.

Figure 3.13 displays the IRSF axial ratio $(b/a)_{IRSF}$ divided by the 2MASX axial ratio $(b/a)_{2MASS}$ before applying and after applying the three corrections versus the extinction levels A_K. Filled red squares present the IRSF and 2MASX ratio without applying any correction to the 2MASX axial ratio. Unfilled green circles stand for the simple average correction to the 2MASX galaxies, blue filled circles stand for the correction based on the μ_e, and downwards-pointing triangles show the correction based on the μ_c to the 2MASS

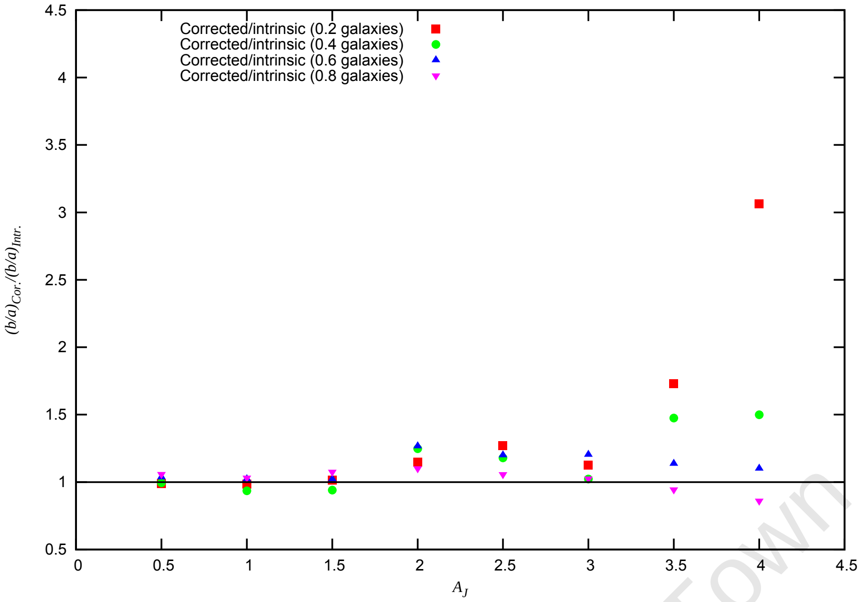

Figure 3.10: Corrected axial ratio divided by intrinsic axial ratio in the J-band as a function of the foreground extinction. The filled squares, circles, upwards-pointing triangles and downwards-pointing triangles present galaxies of axial ratio $b/a < 0.2$, $0.2 < b/a < 0.4$, $0.4 < b/a < 0.6$, and $0.6 < b/a < 0.8$, respectively.

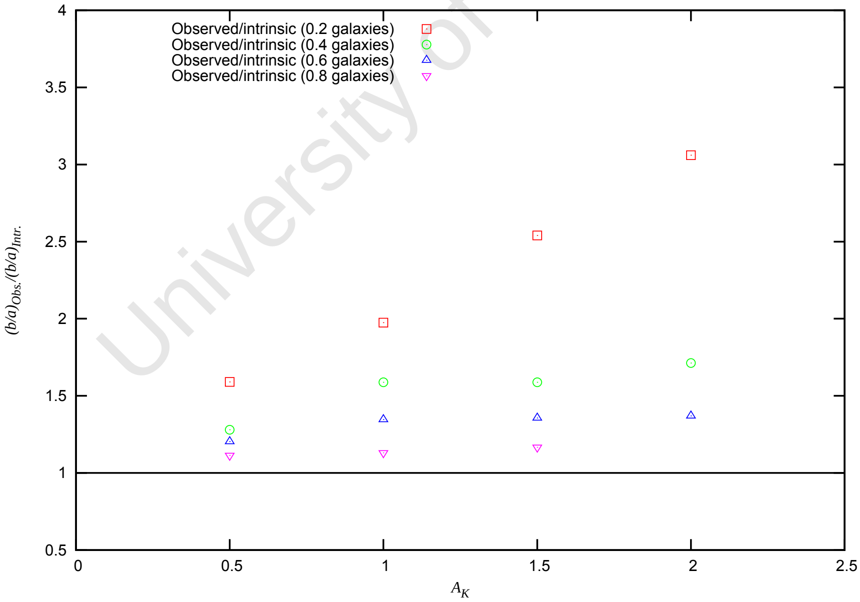

Figure 3.11: Absorbed axial ratio divided by their intrinsic axial ratio in the K_s-band as a function of the foreground extinction. The unfilled squares, circles, upwards-pointing triangles and downwards-pointing triangles present galaxies of axial ratio $b/a < 0.2$, $0.2 < b/a < 0.4$, $0.4 < b/a < 0.6$, and $0.6 < b/a < 0.8$, respectively.

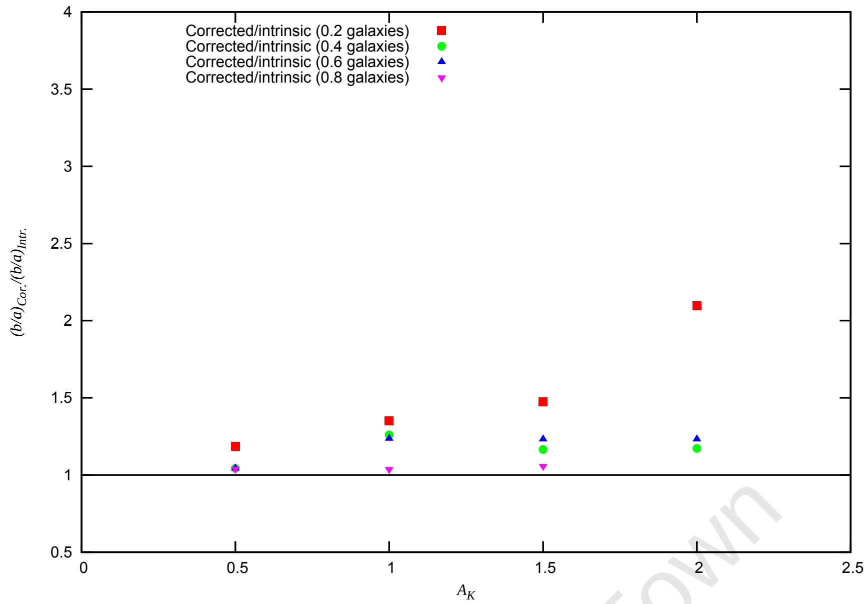

Figure 3.12: Corrected axial ratio divided by their intrinsic axial ratio in the K_s-band as a function of the foreground extinction. The filled squares, circles, upwards-pointing triangles and downwards-pointing triangles present galaxies of axial ratio $b/a < 0.2$, $0.2 < b/a < 0.4$, $0.4 < b/a < 0.6$, and $0.6 < b/a < 0.8$, respectively.

axial ratios. The solid black line shows the ideal value that all points should follow if the 2MASS and IRSF derived axial ratio are the same.

We can clearly notice that the correction based on μ_c is more efficient than the μ_e correction and the average correction. The deviation of the ratio at extinction level of $A_K > 0.6$ can be explained by the fact that both data sets from 2MASX and IRSF are highly affected by dust at this extinction level and the assumption of using the IRSF axial ratio as the intrinsic axial ratio become unreliable.

This method still needs further analysis based on a larger sample of spirals.

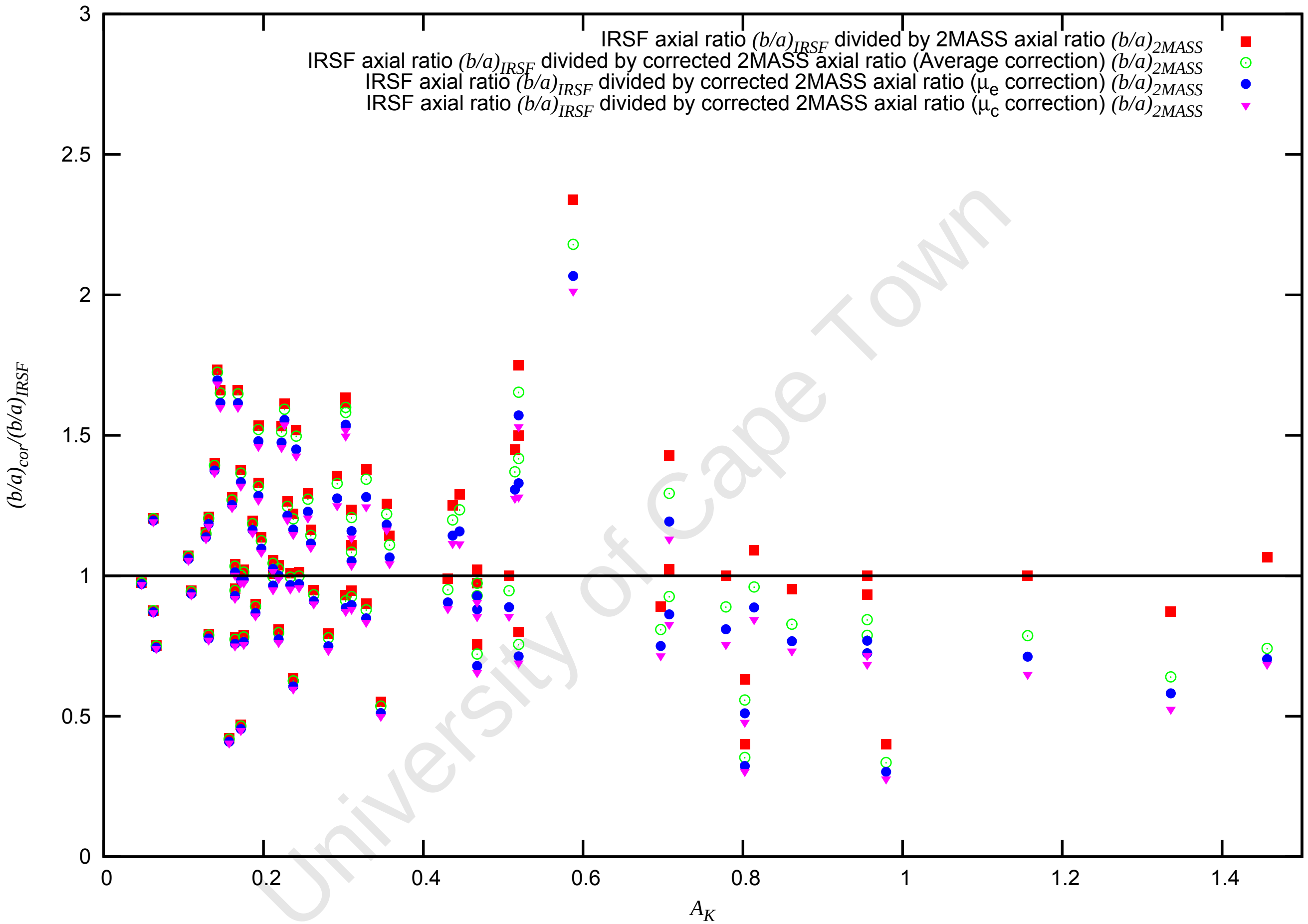

Figure 3.13: IRSF axial ratio $(b/a)_{IRSF}$ divided by 2MASS axial ratio $(b/a)_{2MASS}$ are represented as filled red squares. Unfilled green circles show the IRSF axial ratio $(b/a)_{IRSF}$ divided by 2MASS axial ratio $(b/a)_{2MASS}$ corrected using the average corrections, filled blue circles using the μ_e correction, and triangles using the μ_c correction.

3.5 Conclusion

In this chapter I studied the effect of the foreground dust on the axial ratio of observed spiral galaxies. I find that galaxies appear rounder with increasing obscuration level. Three different methods using independent samples of galaxies were used to quantify this effect. The first method uses 54 spiral galaxies obtained from the LGA with different morphological types and intrinsic axial ratios. This method shows that the effect of dust is stronger for the highly-inclined galaxies than the less-inclined galaxies. Similar results are obtained from the second method which is based on fully simulated galaxies. Three different preliminary correction models were proposed from these two methods. The average correction model which is the simplest model, the optimized correction model which is based on the central surface brightness μ_c and a third model based on the half-light effective mean surface brightness μ_e. These correction models have been tested and show its applicability to reproduce the intrinsic axial ratio from the observed value up to extinction level of about $A_J = 3$ mag, respectively $A_K = 1$ mag. The third method is based on comparing the axial ratios from shallow and deep surveys. A sample of 82 spirals have photometry both in 2MASX and IRSF. This method still need more analysis and larger sample of spirals.

In the future, we will expand the analysis of this effect through statistical studies. Simulation of different level of extinction on a larger sample of spirals will be applied. This will enable us to quantify the effect of the extinction on the number of selected galaxies in the TF analysis. An accurate correction model will increase the number of intrinsically edge-on galaxies in the TF sample, which are excluded because of its appearance.

Chapter 4

Galaxy Peculiar velocities in the Zone of Avoidance

In this chapter the Tully-Fisher template relation constructed in Chapter 2 is used to derive the peculiar velocities of galaxies that lie behind the Milky Way. The HI and NIR data of a subsample of the HIZoA galaxies in the southern ZoA are used. This chapter is organized as follows. In Section 4.2, I present the data from both the southern and northern ZoA. Section 4.3 discusses all the corrections applied to galaxy parameters of the sample. In Section 4.4 the derived peculiar velocities for field galaxies in the ZoA are analyzed. As an example the preliminary flow field for a subsample of galaxies in the southern ZoA is presented in Section 4.5.

4.1 Introduction

Unlike those for nearby stars, the proper motions (the motion perpendicular to our line-of-sight) of galaxies cannot be measured and only the radial velocity (the motion along our line-of-sight) can be observed. The radial velocity of galaxies can be decomposed into two components: (1) a recessional velocity due to the uniform expansion of the universe and (2) a peculiar velocity caused by density inhomogeneities. It is not straight forward to separate these two components as it requires a distance indicator that is independent of redshift. Two types of distance indicators are used: (1) primary distance indicators which do not require calibration by another method, and (2) secondary distance indicators, so-called because they require calibration via primary distance indicators. Typically Cepheid variable stars are used as the primary distance indicator, however beyond 20 Mpc they become too faint even with the Hubble Space Telescope, and a secondary indicator must be used.

In the last few decades, the TF relation (Tully & Fisher 1977) for spirals and the Faber-Jackson (FJ) relation (Faber & Jackson 1976), the modified FJ relation (Dressler 1987), and the Fundamental Plane (FP) relation (Djorgovski & Davis 1987) for elliptical galaxies have been adopted as the workhorses for determining distances independent of the Hubble velocity relation. Throughout this thesis I focus only on using the TF method.

Since its inception many authors have used the TF relation in distance and peculiar velocity surveys (e.g., Han 1992b; Courteau 1993, Courteau et al. 1993; Mould et al. 1993; da Costa et al. 1996; dell'Antonio et al. 1996; Giovanelli et al. 1998; Tully & Pierce 2000; Masters 2005; Springob et al. 2007; Theureau et al. 1998; Tully et al. 2008; Masters et al. 2008; Courtois & Tully 2012). One of the largest TF surveys available to date is the I-band (SFI++) survey (Springob et al. 2007), which uses both cluster and field galaxies. The 2MASS Tully-Fisher Survey (2MTF; Masters et al. 2008, Hong et al. 2013a;b) intends to provide a complete TF analysis (i.e. distances and peculiar velocities) of all bright inclined spirals with $K_s{}^\circ \leq 11\overset{\mathrm{m}}{.}25$ in the 2MASS Redshift Survey (2MRS; Huchra et al. 2005; 2012). Although the use of the NIR TF analysis will reduce the impact of dust extinction of the Milky Way, the Zone of Avoidance is not well sampled in the 2MTF ($|b| < 5°$; $|b| < 8°$ for $|l| < 30°$). The ZoA thus remains mostly uncharted territory for bulk studies, representing a large gap in our understanding of the local universe.

This Chapter aims to use the available HI and NIR data to test the reliability of determining peculiar velocities for galaxies in the ZoA which are excluded from the 2MTF. The 2MTF, thus supplemented with our data, will result for the first time in a complete all-sky peculiar velocity survey.

This Chapter is organized as follows. In Section 4.2 we discuss the data from both the HI and NIR. Section 4.3 provides a number of what corrections applied to the data. Section 4.4 provides a recipe on how to derive peculiar velocities for field galaxies in the ZoA. A preliminary flow field for a subsample of the southern ZoA is presented in Section 4.5.

4.2 Data

4.2.1 HI Parkes deep ZoA survey

The HI Parkes Deep Zone of Avoidance Survey (HIZoA) is a blind HI survey of the southern ZoA ($|b| < 5°$; Dec $< +15°$), conducted with the 64 m Parkes radio telescope in three parts: (1) the main part covers $|b| < 5°; 212° \leq l \leq 36°$ (Kraan-Korteweg et al. 2005; Henning et al. 2005; Henning et al. in prep), (2) the Northern Extension (NE) covers the northern regions visible from Parkes ($|b| < 5°; 36° < l < 52°$ and $196° < l < 212°$; Donley et al. 2005), and (3) the Galactic Bulge (GB) extension, which goes to higher latitudes around the GB region ($5° < |b| < 10°; 332° < l < 36°$ and $10° < |b| < 15°; 352° < l < 24°$; Shafi 2008; Kraan-Korteweg et al. 2008). These three surveys cover the most obscured southern ZoA visible from Parkes out to 12700 km/s, and result in more than a thousand detected galaxies with an rms $\sim$ 6mJy/beam. Figure 4.1 shows the spatial distribution of the HIZoA galaxies (bottom panel) represented by the open circles and colour-coded by redshift. The small dots represent all galaxies with known velocities (from the literature) in and around the ZoA. The top panel shows the archival galaxies while the bottom panel shows both the HIZoA galaxies as well as the archival galaxies, and demonstrates how effective HI surveys are in filling the ZoA.

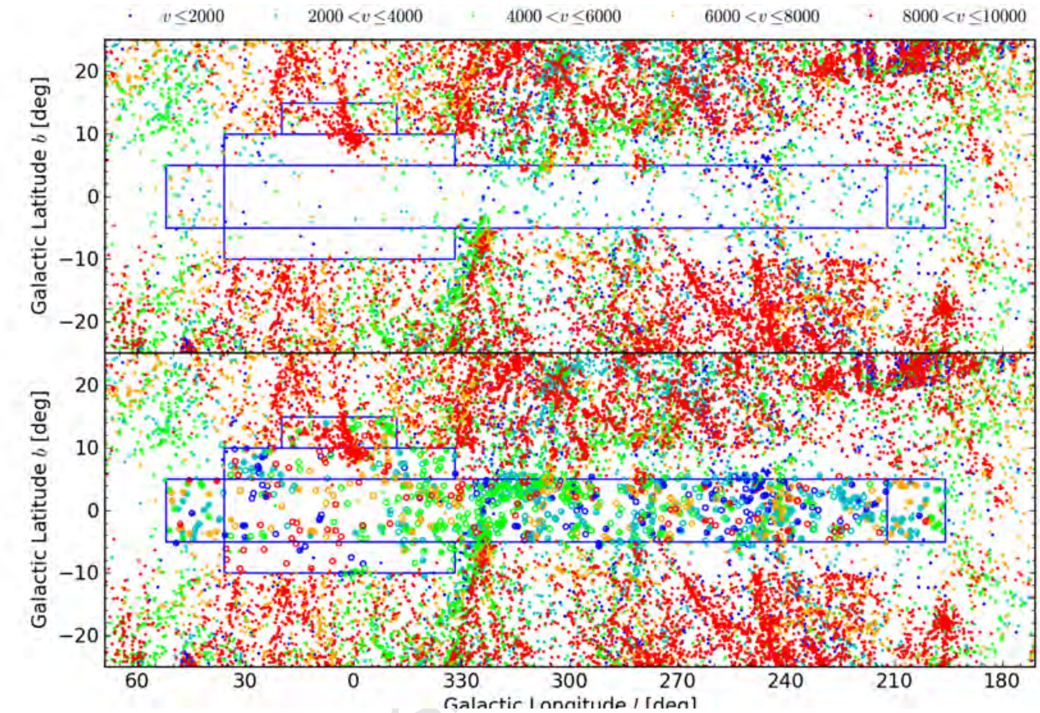

Figure 4.1: The spatial distribution of the HIZoA galaxies plus galaxies of known velocities colour-coded by redshift. The open circles represent the HIZoA galaxies while the small dots represent the literature galaxies. The blue rectangles outline the boundaries of the three surveys in the southern ZoA. Figure is taken from Williams (2011).

Figure 4.2 displays the velocity distribution of the HIZoA galaxies. The histogram shows that 75% of the HIZoA galaxies lie within 6000 km/s, then there is a clear drop-off to the high-velocity end of 12700 km/s.

4.2.2 Deep NIR follow-up survey

While 2MASS covers the entire sky and over 1,000,000 galaxies have been observed, coverage at the lower Galactic latitudes is patchy and incomplete. Only 130 of the 1104 HIZoA galaxies have a likely counterparts in 2MASS (Williams 2011). Moreover, measurements suffer from confusion and blending. To alleviate and improve upon 2MASS measurements, we have started an NIR J, H, K_s-bands follow-up survey of all HIZoA-galaxies with the

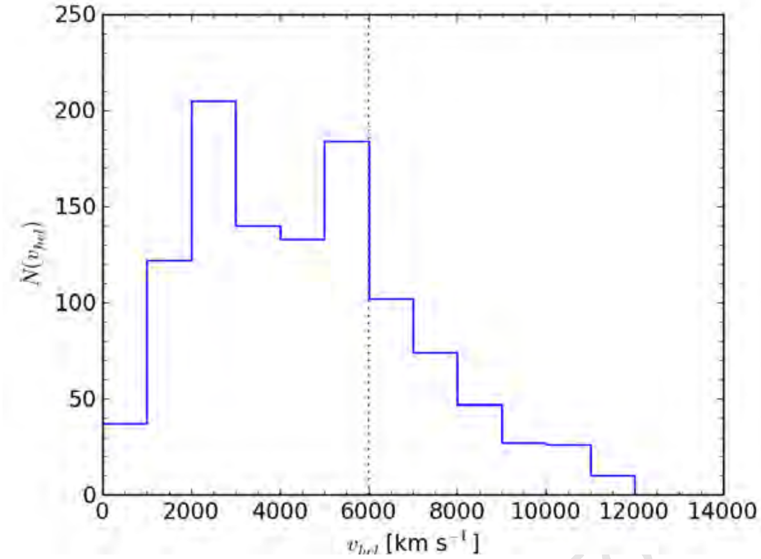

Figure 4.2: The velocity distribution of the HIZoA galaxies. Figure adopted from Williams (2011)

InfraRed Survey Facilty (IRSF) on the 1.4m telescope at Sutherland, South Africa. The Simultaneous 3-colour InfraRed Imager for Unbiased Survey (SIRIUS) camera on the IRSF has a field of view of $7'.7 \times 7'.7$ with a resolution of $0''.45$/pixel. The targeted survey images have exposure time of 10 min, which results in a 2 mag deeper survey compared to 2MASX in the K_s-band. The acquisition operations were started in 2006 and finished in 2013, resulting in complete deep NIR survey of the entire HIZoA detections (Williams 2011; Williams et al. 2011; Said et al. in prep).

A comparison for some of the IRSF galaxies that are also identified in 2MASX is shown in Figure 4.3. The right hand panels show composite 3-colour 2MASS JHK_s images, while the left hand panels show the 3-colour images constructed from the deep IRSF JHK_s images. The improved sensitivity and higher resolution ($0''.45$/pixel) of the IRSF images compared to 2MASS allow for high fidelity measurement of the surface brightness profile over the disk. Furthermore, faint stars superimposed on the galaxy image can be resolved, and therefore removed in the IRSF images while they cannot typically be detected in the 2MASS images.

Note that the IRSF finds many more counterparts to HIZoA galaxies compared to the shallower 2MASX (approximately 80% versus 12%).

4.2.3 The peculiar velocity sample within the ZoA

The peculiar velocity sample in the southern ZoA used here is the same as that used by Williams (2011). It originates from a cross-matching of HIZoA galaxies with 6000 km s^{-1} and the IRSF images. Only galaxies with secure counterparts and reliable photometry

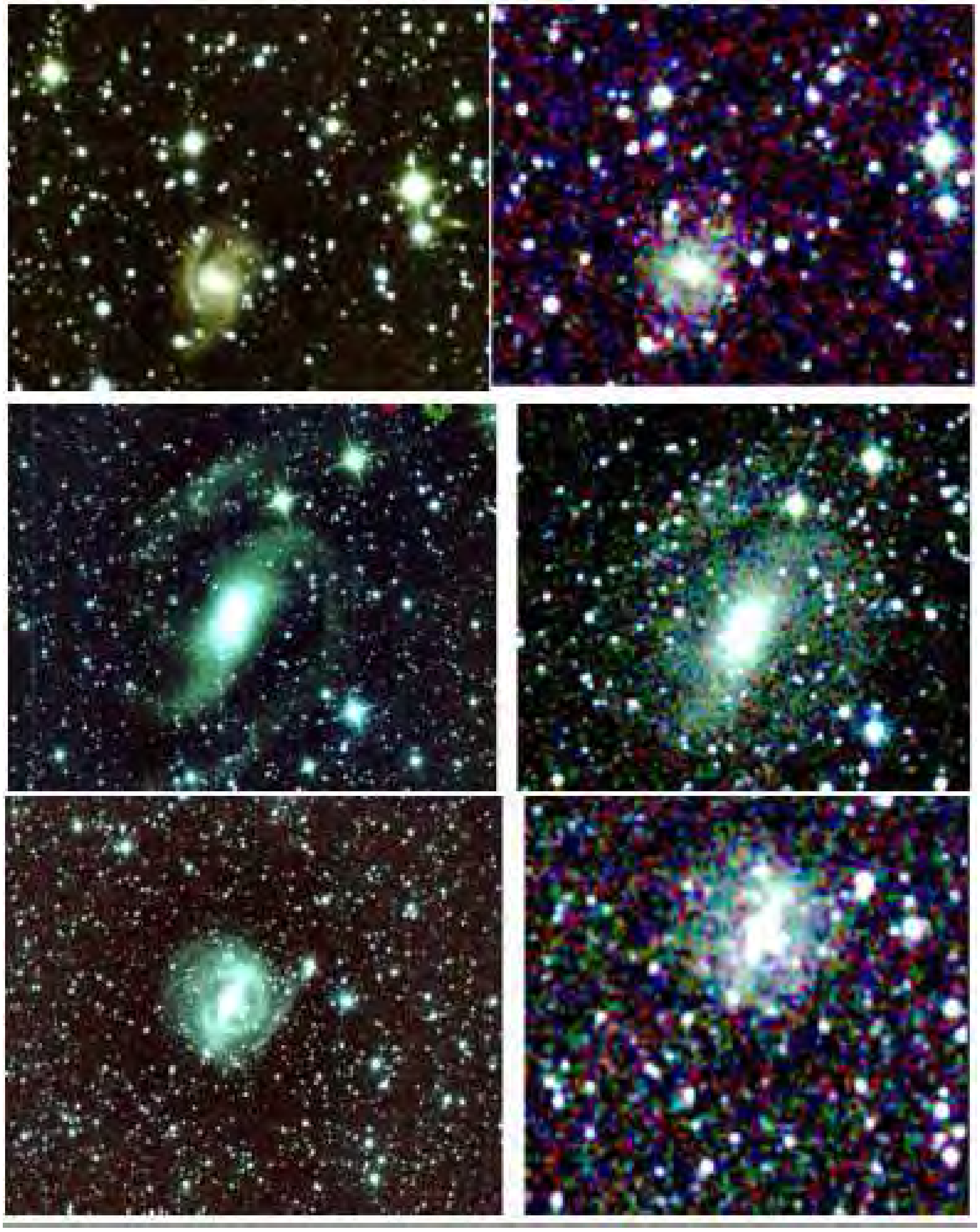

Figure 4.3: Comparison of the IRSF image quality (left panels) and the 2MASS images quality (right panels). The 3-colour images are constructed from assigning the colour blue to the J-band (1.2 μm), green to the H-band (1.6 μm), and red to the K_s-band (2.2 μm). Longer exposure time (10 min) and higher resolution ($0\farcs45$/pixel) of the IRSF survey compared to the 2MASS survey (8 sec and $2''$/pixel), reveal the fainter outer parts of galaxies and resolve faint stars superimposed on the galaxy image.

are used. After applying additional restrictions on inclination ($b/a < 0.7$) and line-width ($\log W > 1.8$), the final number of galaxies in the sample becomes 178 spirals.

4.3 Corrections

To be consistent with the calibrated Tully – Fisher relation constructed in Chapter 2, I apply the same corrections to the photometric and spectroscopic parameters. The parameters of interest here are the line-width, corrected for inclination and the magnitude, corrected for Galactic and internal extinction, and the k-correction.

4.3.1 Line-width corrections

The HIZoA survey provides the HI spectral data, including velocity and line-width. Consistent with the calibration method, I use the equation given by Springob et al. (2007) to correct the line-width

$$W = [\frac{w_{50} - \Delta_s}{1+z} - \Delta_t]\frac{1}{\sin i} \tag{4.1}$$

where w_{50} is the width measured at 50% of the peak flux, Δ_t is the effect of turbulent motion and Δ_s is the instrumental correction. The difference between this equation and the one used by Giovanelli et al. (1997a) is that the effect of turbulent motion is subtracted here linearly and not quadratically. For the the effect of turbulent motion, $\Delta_t = 6.5$ km s^{-1} is used, and for the instrumental correction

$$\Delta_s = 2\Delta v\lambda \tag{4.2}$$

is used (Springob et al. 2005). The parameter λ is a piece-wise defined function of SNR and channel separation:

$$\lambda = \lambda_1(\Delta v) \qquad \log(\mathrm{SNR}) < 0.6, \tag{4.3a}$$

$$\lambda = \lambda_2(\Delta v) + \lambda_2'(\Delta v)\log(\mathrm{SNR}) \qquad 0.6 < \log(\mathrm{SNR}) \leq 1.1, \tag{4.3b}$$

$$\lambda = \lambda_3(\Delta v) \qquad \log(\mathrm{SNR}) > 1.1. \tag{4.3c}$$

Table 4.1 shows the values of λ as given in (Springob et al. 2005). The inclination i is derived

(Δv) (km s $^{-1}$)	Smoothing	$\lambda_1(\Delta v)$	$\lambda_2(\Delta v)$	$\lambda_2'(\Delta v)$	$\lambda_3(\Delta v)$
< 5	H	0.005	-0.468	0.785	0.395
5-11	H	$0.04\Delta v - 0.18$	$0.05\Delta v - 0.72$	$-0.03\Delta v + 0.92$	$0.02\Delta v + 0.28$
> 11	H	0.227	-0.1523	0.623	0.533
< 5	B	0.020	-0.4705	0.820	0.430
5-11	B	$0.05\Delta v - 0.24$	$0.04\Delta v - 0.67$	$0.02\Delta v + 0.72$	$0.06\Delta v - 0.12$
> 11	B	0.332	-0.2323	0.940	0.802

Table 4.1: Velocity width instrumental correction parameters

from the J-band ellipticity $\epsilon_J = 1 - (b/a)_J$ via

$$\cos^2 i = \frac{(1-\epsilon)^2 - q_0^2}{1 - q_0^2} \tag{4.4}$$

following Giovanelli et al. (1997a). The parameter $(a/b)_J$ is the J-band axial ratio fit to the 3σ isophote (the isophote which corresponds to a surface brightness $\sim$ 3 times the background noise). The values for the surface brightness of $\sim 3\sigma$ are 20.09 mag arcsec^{-2} at J, 19.34 mag arcsec^{-2} at H, and 18.55 mag arcsec^{-2} at K_s (Jarrett et al. 2000). The J-band axial ratio $(b/a)_J$ is the best tracer of the inclination, it suffers less than H, and K_s-bands from the effect of the bulge if the 3 σ isophote is close to the center (Masters et al. 2003). We proceed to use the J-band after applying a seeing correction which is parameterized as

$$(a/b)_{corr} = (a/b)_{obs}(1 - 0.02x + 0.21x^2 - 0.01x^3), \tag{4.5}$$

with

$$x = \mathrm{FWHM}(\frac{a/b}{r_{20}})_{\mathrm{measured}}, \tag{4.6}$$

where FWHM = 2.″5 (the full-width half-maximum of the seeing disc) (Masters et al. 2003).

4.3.2 Magnitude corrections

The corrected absolute magnitude of the galaxy is calculated from the observed apparent magnitude as

$$M_{\mathrm{corr}} - 5\log h = m_{\mathrm{obs}} - A_X - I_X - k_X - 5\log v_{\mathrm{CMB}} - 15, \tag{4.7}$$

where A_X, I_X, and k_X are a correction for extinction due to dust in our galaxy, a correction for extinction internal to the galaxy itself, and a cosmological k-correction, respectively.

The Schlegel et al. (1998) extinction map is not well calibrated at low Galactic latitude regions (see Chapter 1 for discussion of different extinction maps). Different authors have shown that Schlegel et al. (1998) overestimates the reddening at low latitudes (Arce & Goodman 1999, Nagayama et al. 2004, Schröder et al. 2005; 2007). Therefore, an additional correction of only 82% of the DIRBE/IRAS values (Schröder et al. 2007, Williams 2011) was adopted.

Additionally, the peculiar velocities need to be in the CMB frame. I transform the heliocentric velocity v_{hel} to v_{CMB} using the model given by Fixsen et al. (1996):

$$v_{\mathrm{CMB}} = v_{\mathrm{hel}} + v_{\mathrm{apex}}[\sin b \sin b_{\mathrm{abex}} + \cos b \cos b_{\mathrm{abex}} \cos(l - l_{\mathrm{abex}})] \tag{4.8}$$

where $v_{\mathrm{apex}} = 371.0$ km s^{-1}, $l_{\mathrm{abex}} = 264.^\circ14$, and $b_{\mathrm{abex}} = 48.^\circ26$ are the velocity and Galactic coordinates of the apex vector describing the relative motion of the Sun with respect to the CMB.

4.3.3 Malmquist bias corrections

Over the years, many schemes have been adopted to correct for the Mamquist bias (Freudling et al. 1995, Park & Park 2006, Springob et al. 2007). Because our sample is not yet complete and therefore our results in this chapter are a preliminary results, I left any correction for this effect for now.

4.4 Tully-Fisher analysis

Before proceeding with the derivation of the peculiar velocity field in the southern ZoA based on a preliminary sample, a comparison of the TF relations derived from total and isophotal magnitude is presented here. Figures 4.4 and 4.5 show the absolute magnitude as a function of rotational width for galaxies in our sample in J(top panel), H(middle panel) and K_s(bottom panel). In all panels the dashed green line displays the TF calibrated relation derived from the total magnitudes as in Masters et al. (2008) and isophotal magnitude as in Chapter 2. Dotted black lines in all panels represent ± 3 times the intrinsic scatter of the TF calibrated relation (ϵ_{int}). While Fig. 4.5, derived from the isophotal magnitude, shows a good agreement between the galaxies in the ZoA and the calibrated TF relation, Figure 4.4, derived from the total magnitude shows a larger scatter and offset between our sample and the TF relation for the total mass. This offset in Figure 4.4 demonstrates that the use of the total magnitude can lead to an artificial cosmic flow. This can be seen in the huge offset in the distribution of peculiar velocities in Fig. 4.8. The offset disappears when using the isophotal magnitude in Fig. 4.9. Most of the galaxies in Figure 4.5 lie within $\pm 3\epsilon_{int}$ of the calibrated TF relation.

4.4.1 The total observed scatter

The total observed scatter in Figs. 4.4 and 4.5 increases with decreasing rotation width for both total and isophotal magnitudes. I therefore employ the equation used by Giovanelli et al. (1997a) to parametrize the scatter as:

$$\sigma = a + b(\log W - 2.5). \tag{4.9}$$

The observed scatter in the J, H, and K_s-bands as a function of line-width is shown in Figs. 4.6 & 4.7 for total and isophotal magnitude respectively. Fitting a linear relation of the above form to the scatter in each of the three bands yields the following relations for total magnitudes:

$$\epsilon_{\text{obs},J} = 0.906 - 2.284(\log W - 2.5), \tag{4.10a}$$

$$\epsilon_{\text{obs},H} = 0.797 - 2.213(\log W - 2.5), \tag{4.10b}$$

$$\epsilon_{\text{obs},K} = 0.813 - 2.698(\log W - 2.5), \tag{4.10c}$$

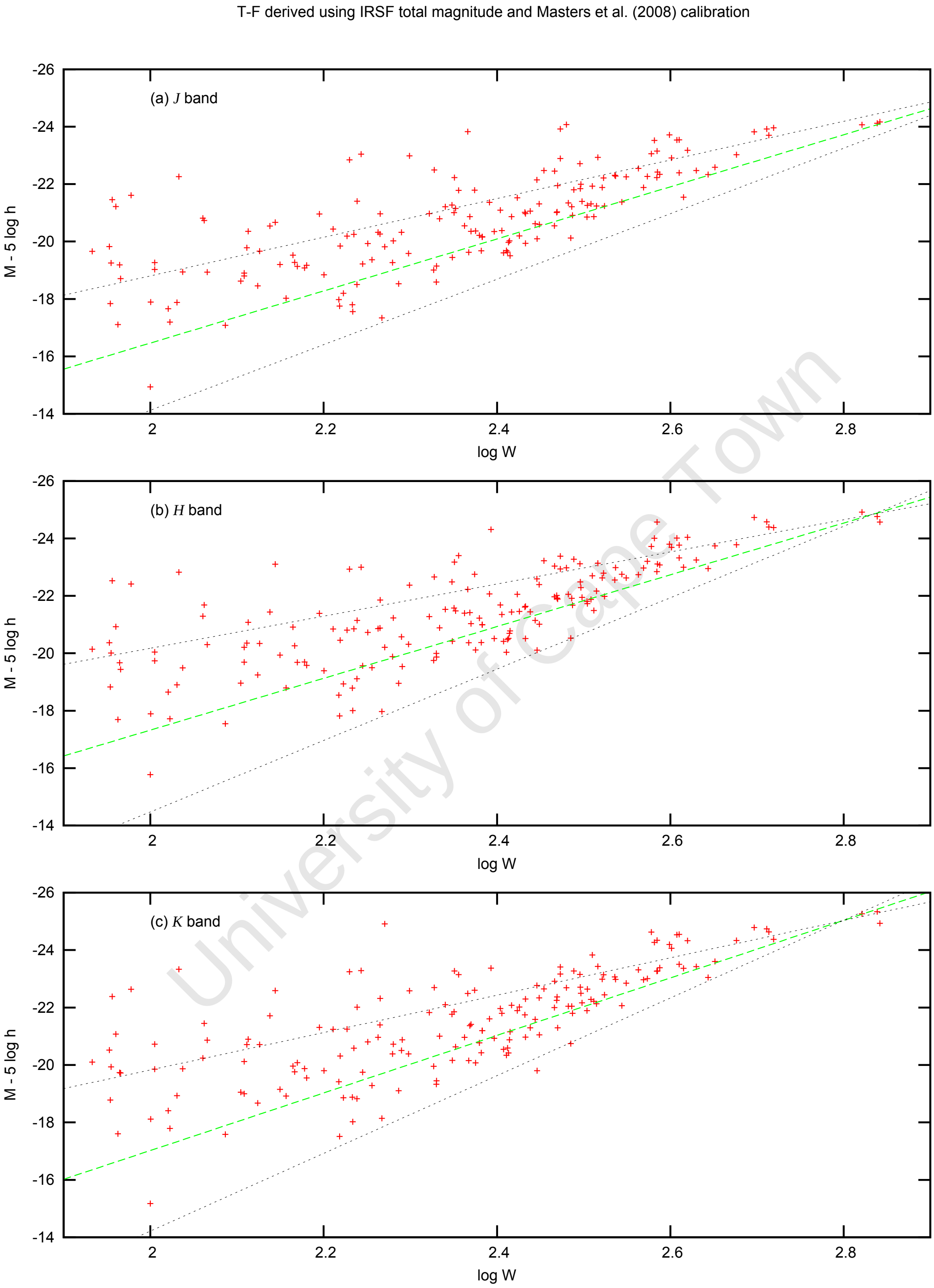

Figure 4.4: Tully-Fisher relation for galaxies in the ZoA. Absolute magnitude of 178 galaxies derived from IRSF total magnitude in J, H, and K_s-bands as a function of rotation width. The green dashed line in all panels denotes the TF relations in the J, H, and K_s-bands of Masters et al. (2008). Black dotted lines above and below the TF relation show three times the TF intrinsic scatter ($\pm 3\epsilon_{int}$) of Masters et al. (2008).

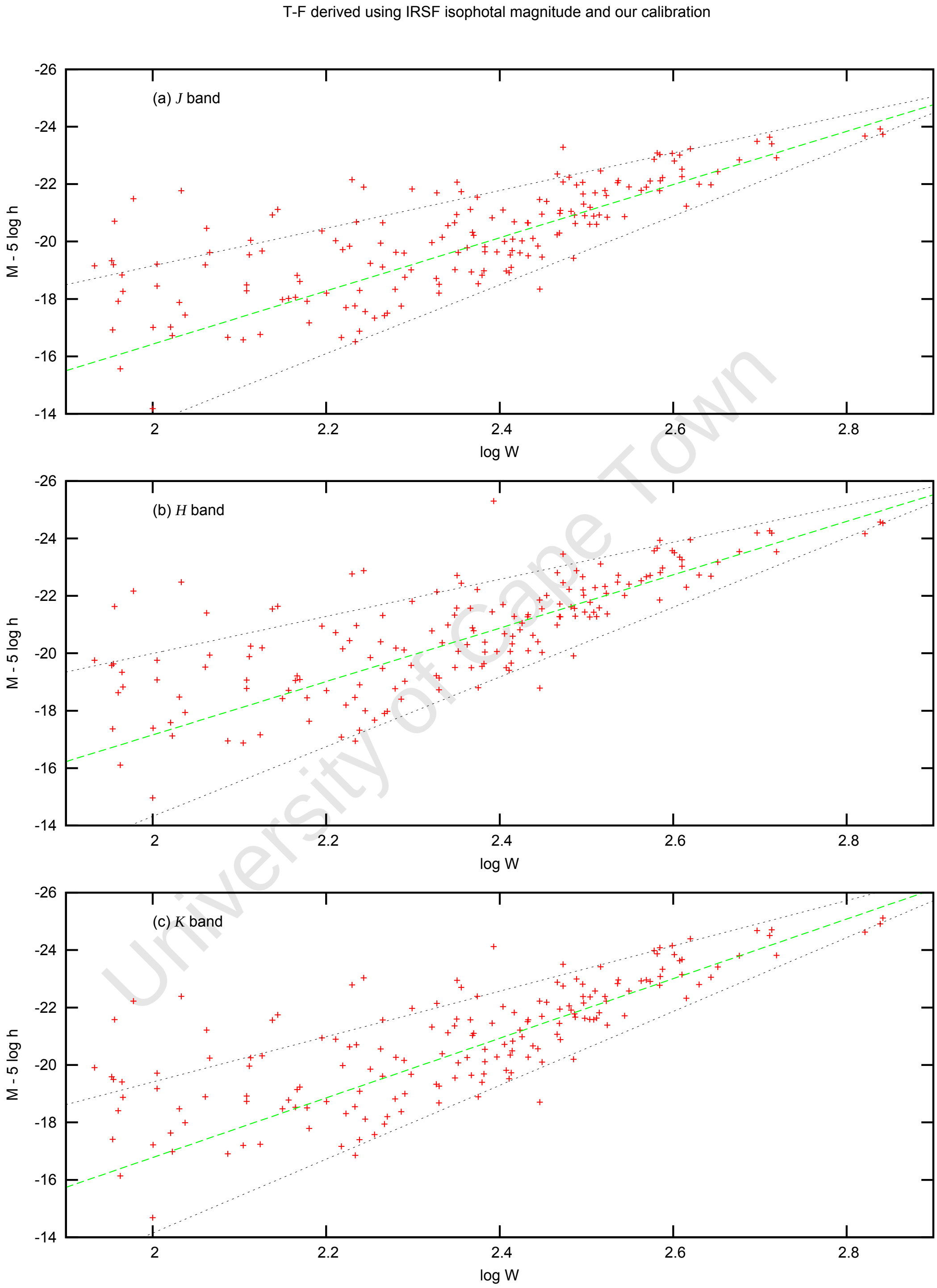

Figure 4.5: Tully-Fisher relation for galaxies in the ZoA. Absolute magnitude of 178 galaxies derived from IRSF isophotal magnitude in the J, H, and K_s-bands as a function of rotation width. The green dashed line in all panels denotes the TF relations in J, H, and K_s-bands derived by us. Black dotted lines above and below the TF relation show three times the TF intrinsic scatter ($\pm 3\epsilon_{int}$) derived in Chapter 2.

and for isophotal magnitudes:

$$\epsilon_{\mathrm{obs},J} = 0.731 - 2.243(\log W - 2.5), \tag{4.11a}$$
$$\epsilon_{\mathrm{obs},H} = 0.690 - 2.258(\log W - 2.5), \tag{4.11b}$$
$$\epsilon_{\mathrm{obs},K} = 0.716 - 2.369(\log W - 2.5). \tag{4.11c}$$

Equations 4.10 and 4.11 and Figures 4.6 and 4.7 demonstrate that the scatter for isophotal TF is reduced by about 20%, 13%, and 12% in the J, H, and K_s-bans, respectively.

4.4.2 Peculiar velocities in the ZoA

The peculiar velocity for field galaxies is given by

$$v_{\mathrm{pec}} = v_{\mathrm{CMB}}(1 - 10^{0.2\Delta M}), \tag{4.12}$$

and the distance to a galaxy by

$$d = \frac{v_{\mathrm{CMB}}}{H_0} 10^{0.2\Delta M}, \tag{4.13}$$

where $\Delta M = M - M(W)$, and $M(W)$ is the absolute magnitude value for the width given by the calibrated TF relation. $\Delta M = 0$ only if the galaxy has no peculiar velocity. The distances and peculiar velocities are calculated for galaxies in our sample. The uncertainties in the peculiar velocity are calculated by combining the absolute magnitude error, velocity width error, and the intrinsic scatter in TF-template relation in a quadratic form.

Histograms of the distribution of the peculiar velocities calculated using total and isophotal magnitude, are shown in Figures 4.8 and 4.9, respectively. Figure 4.8 shows how the offset due to the use of the total magnitude can create a systematic flow: an offsets in of $\Delta m \sim$ 0.2-0.3 may create an artificial flow of about 200-600 km/s in the velocity range of 2000-6000 km/s.

The extreme wings in Figure 4.9 are due to small and face-on galaxies. When excluding those galaxies, these wings disappear as shown in Fig. 4.10 but resulting in a reduction of the number of galaxies in the sample.

Another two histograms have been constructed (the green shaded histogram and the blue filled histogram in Fig. 4.11) to analyze and quantify the overall flow. The shaded histogram in Figure 4.11 shows only the galaxies in the Great Attractor region ($290° < l < 350°$). The shaded histogram indicates a systematic offset compared to the overall sample (the mean value is shifted toward the positive peculiar velocity values compare to the original histogram). The flow in another region away from the GA have been analyzed. The filled histogram denotes the distribution of the peculiar velocity of galaxies away from the GA

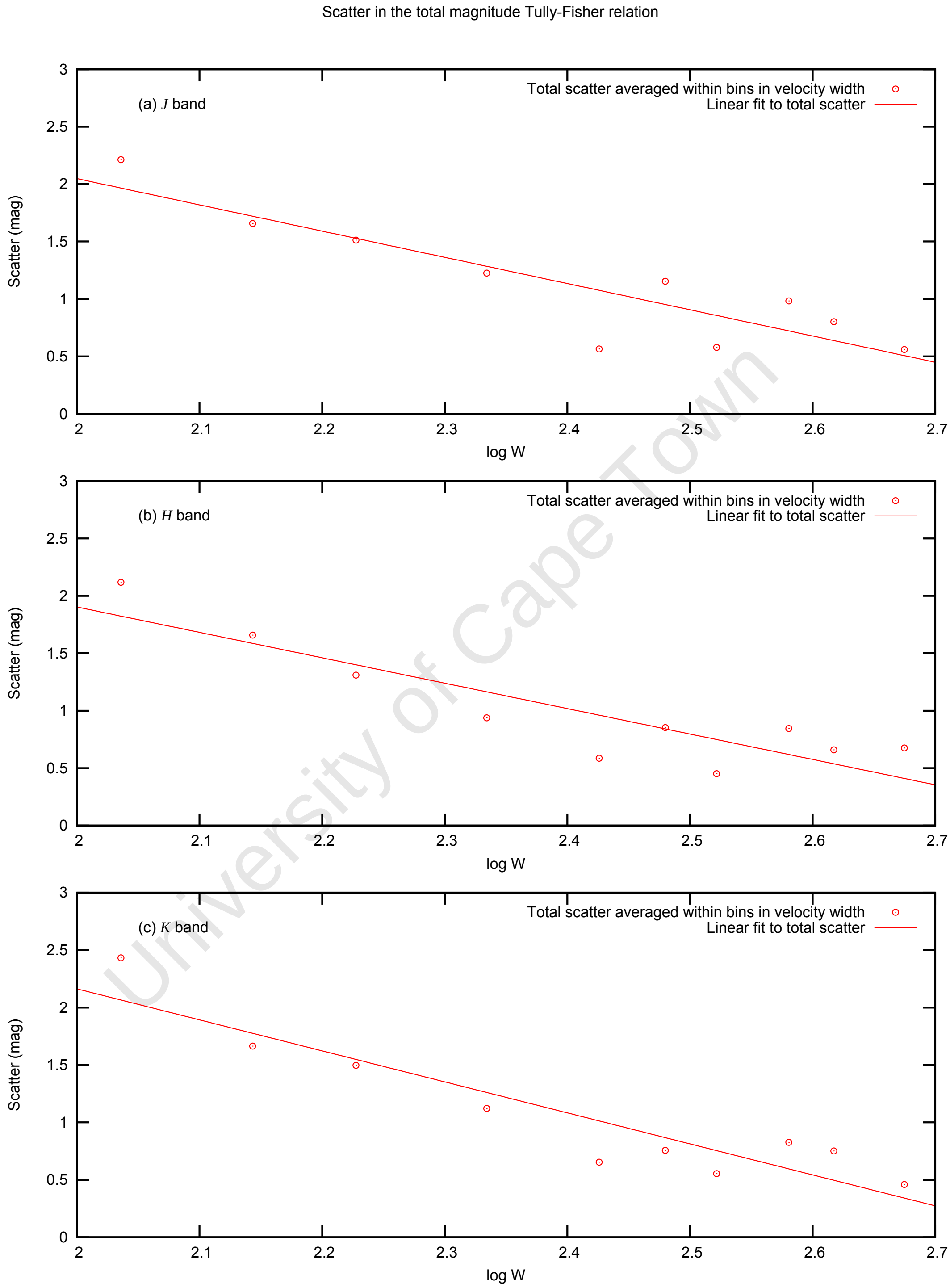

Figure 4.6: Scatter in the total magnitude Tully-Fisher relation using the IRSF sample in the J, H, and K_s-bands. The solid line shows the linear fit to the scatter averaged in bins of velocity width.

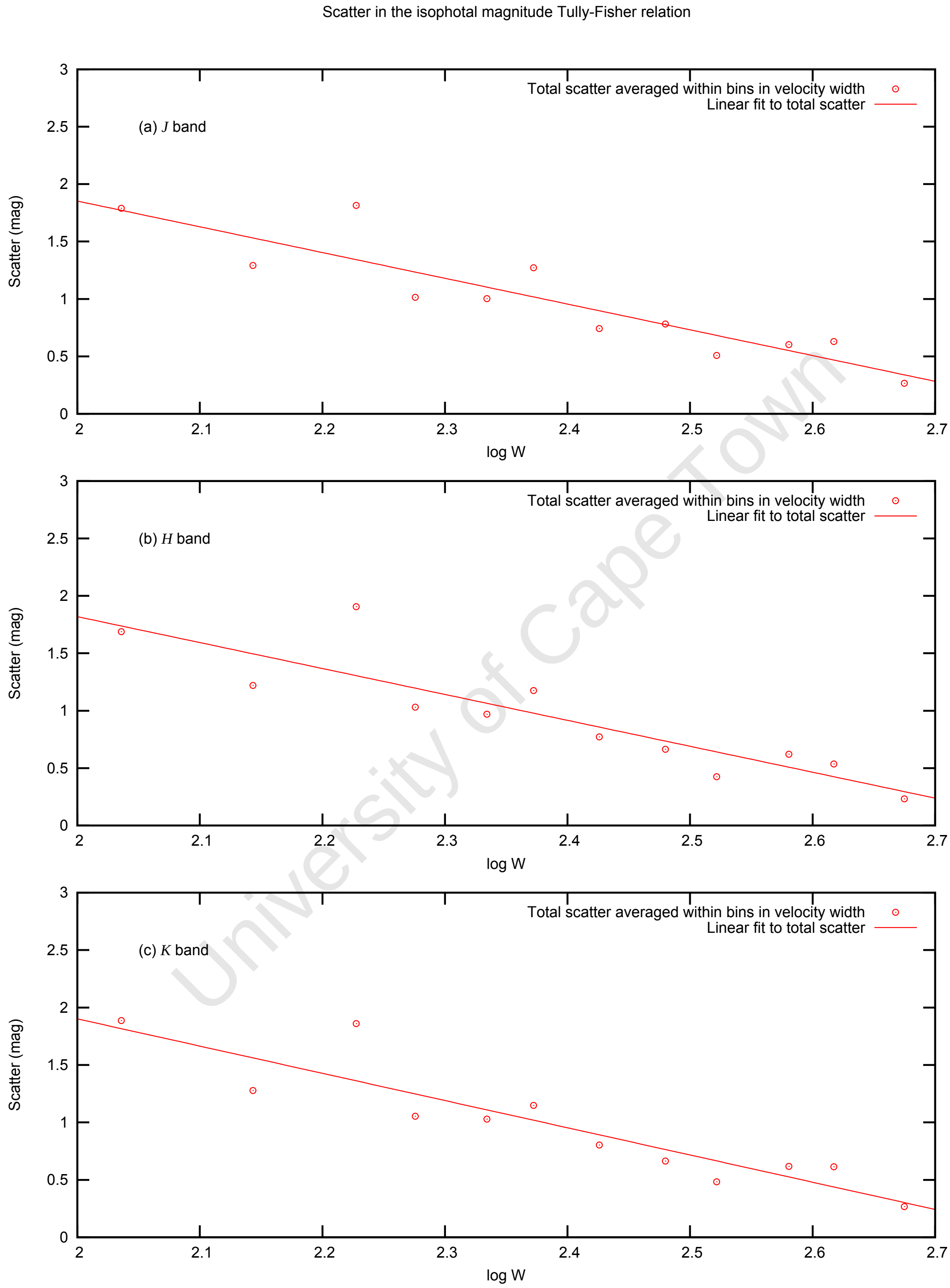

Figure 4.7: Scatter in the isophotal magnitude Tully-Fisher relation using the IRSF sample in the J, H, and K_s-band. The solid line shows the linear fit to the scatter averaged in bins of velocity width.

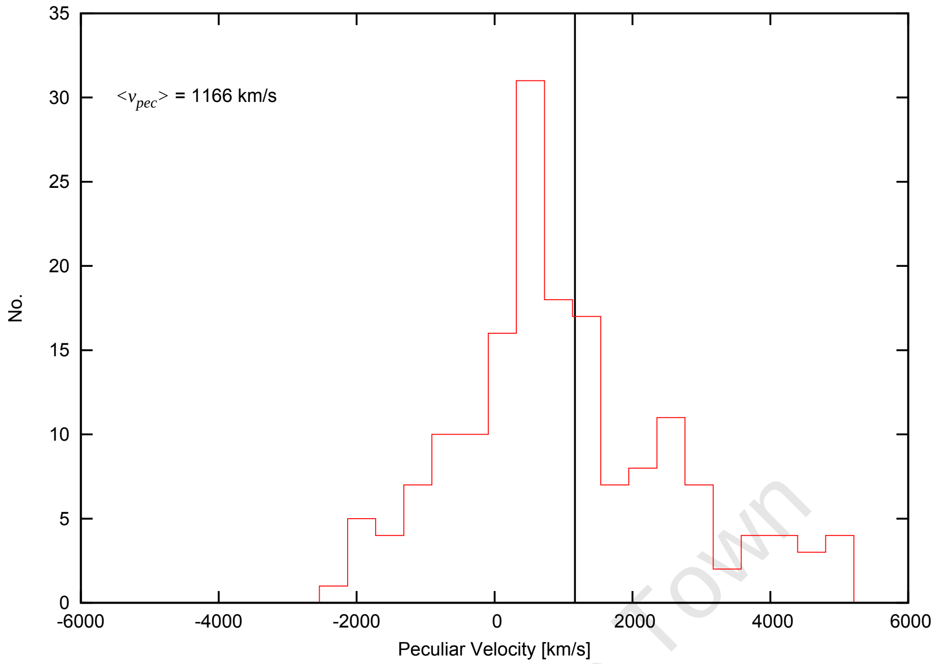

Figure 4.8: The distribution of our derived peculiar velocities of the 178 galaxies in the southern ZoA using total magnitude. The solid vertical line shows the mean peculiar velocity of the sample

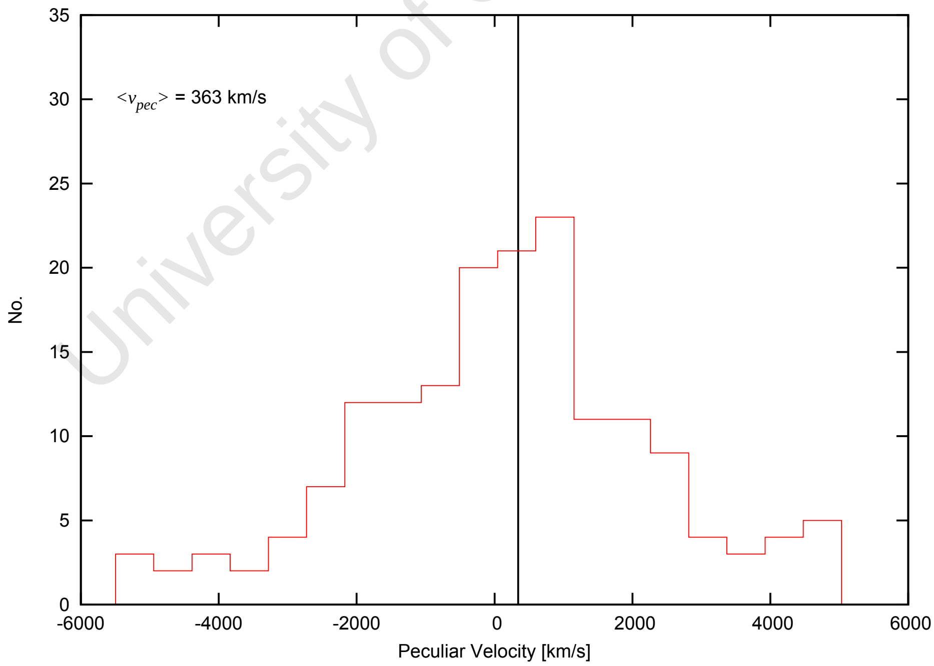

Figure 4.9: The distribution of our derived peculiar velocities of the 178 galaxies in the southern ZoA using isophotal magnitude. The solid vertical line shows the mean peculiar velocity of the sample

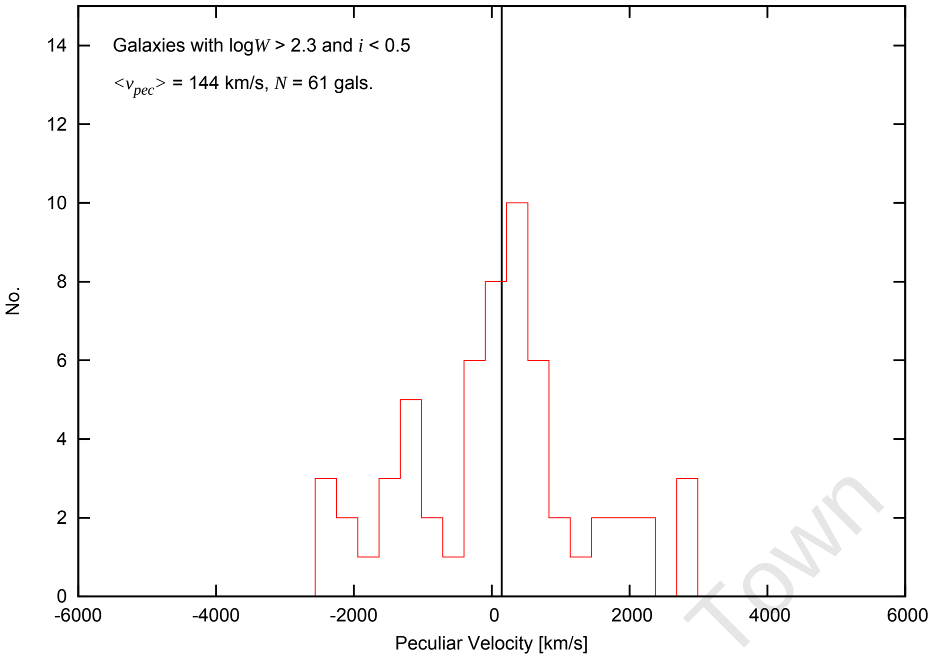

Figure 4.10: The distribution of our derived peculiar velocities of the 61 (large and edge-on) galaxies in the southern ZoA using isophotal magnitude. The solid vertical line shows the mean peculiar velocity of the sample

region ($240° < l < 290°$). This filled histogram shows an overall flow close to zero.

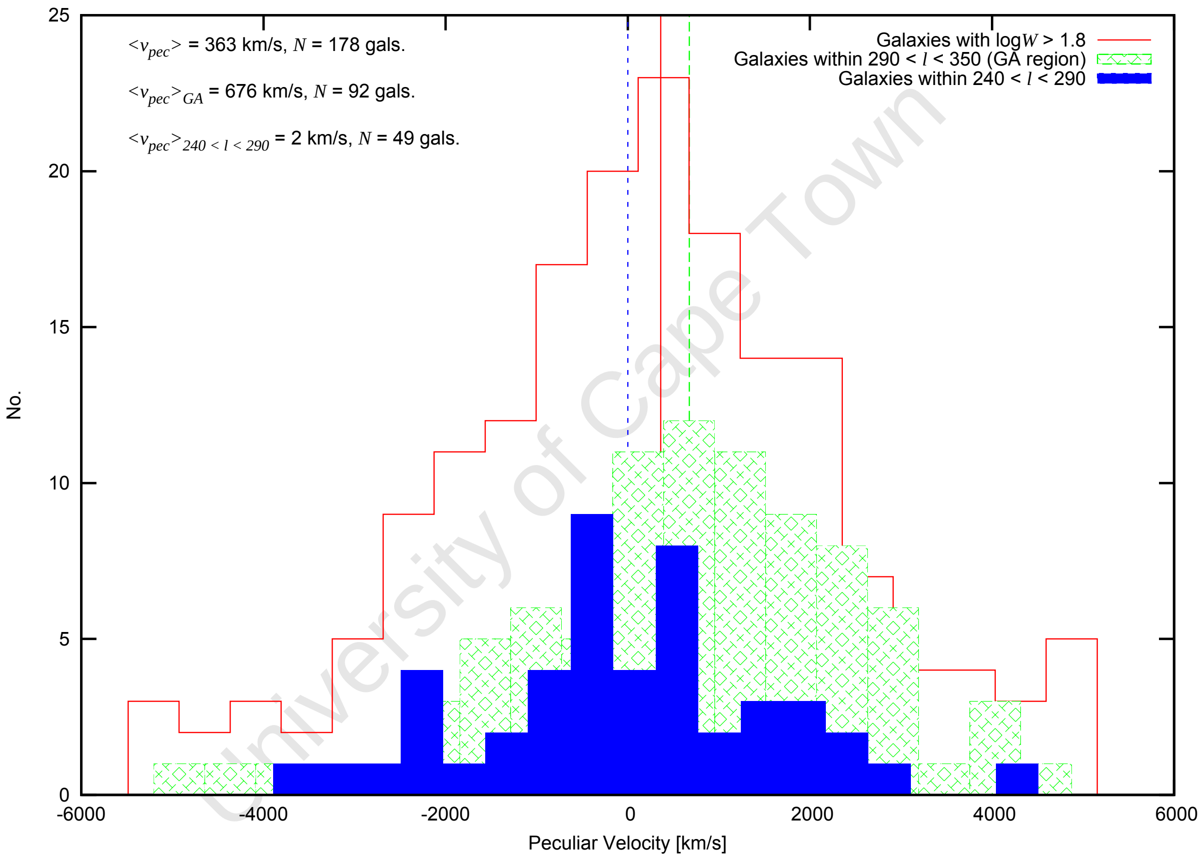

Figure 4.11: Distribution of peculiar velocities derived from isophotal TF relation in the K_s-band. The unfilled histogram shows the peculiar velocity distribution of all galaxies. The shaded histogram represents only galaxies in the GA region $290° < l < 350°$. The filled histogram represents galaxies in $240° < l < 290°$ region. The mean values of the distributions are plotted as vertical lines.

4.5 Flow field in the ZoA

Given that most extreme large peculiar velocities originate from low line-width or face-on galaxies, I used only galaxies with $|v_{pec}| \leq 2500$ km/s to construct the first preliminary map of the flow-field in the ZoA (Figure 4.12). This map is obtained by interpolating the peculiar velocities across Galactic longitude and recessional velocity. Each dot in the map is a galaxy, colour-coded by its measured peculiar velocity. The black star represents the center of the Great Attractor (GA) (Kraan-Korteweg et al. 1996; Woudt 1998; Woudt et al. 1999). The red colour denotes galaxies moving away from us while the blue colour represents galaxies moving toward us. The map clearly suggests infall into the GA (black star). Another infall into the Puppis region ($l \sim 240°$) at about 3000 km/s is observed. Backside infall into Puppis is also evidenced by the blue colour. These patterns suggest that the flow patterns from the preliminary ZoA TF application appear reasonable.

To quantify the effect of the small and face-on galaxies I further divide the sample into different subsamples according to line-width and inclination: (A) contains all 120 galaxies in our sample, (B) contains 75 more edge-on galaxies ($b/a < 0.5$), (C) only 78 large galaxies ($\log W > 2.3$) and (D) 49 large and more edge-on galaxies. These last three subsamples B, C and D, have been used to construct maps of the flow-field in the ZoA (Figures 4.13, 4.14 and 4.15). The details of the flow field can be seen even with the smallest sample in Fig. 4.15.

The restriction of galaxies with $v_{obs} \leq 6000$ km/s limits our ability to quantify the backside infall toward the GA, respectively assess whether the GA as a whole falls towards the much more remote Shapley Concentration (SC). To improve on the GA infall signal we started to extend our sample to $v_{obs} \leq 9000$ km/s in 2012. For even larger redshifts the sample becomes very sparse and the errors on measured peculiar velocities become comparable to the peculiar velocities themselves. The peculiar velocity error is calculated by combining the absolute magnitude error, velocity width error, and the intrinsic scatter in TF-template relation in a quadratic form. Most of the galaxies have errors of a few hundred km/s (Figure 4.16), which is a typical value for most methods available today. Figure 4.16 shows the error in the four subsamples A, B, C and D.

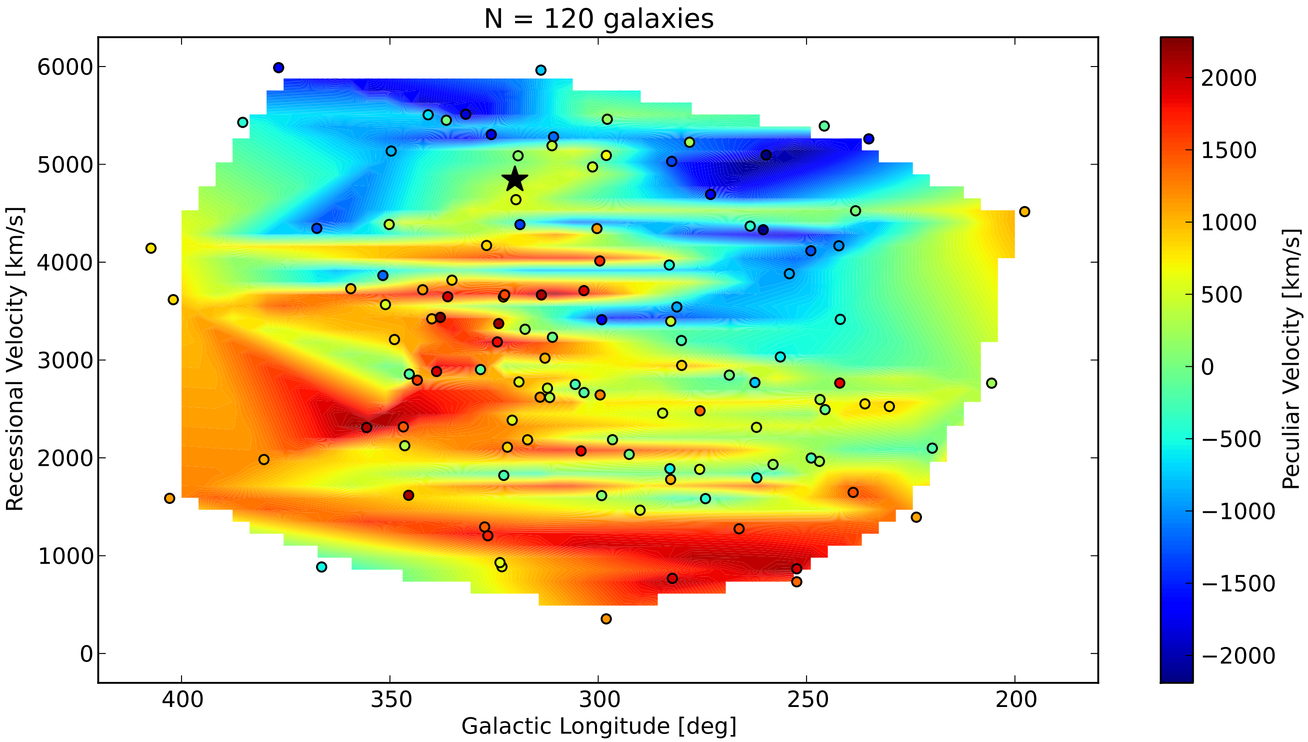

Figure 4.12: Peculiar velocity map of 120 galaxies with recessional velocity $\leq$ 6000 [km/s] and $-2500 < v_{pec} < 2500$[km/s] obtained by interpolating the peculiar velocities across the Galactic longitude and recessional velocity. All galaxies with $\log W > 1.8$ are used here. Individual galaxies are colour-coded by their predicted peculiar velocities in (km/s). The center of the GA is plotted as a large black star at $(l, b, v) = (320°, 0°, 4500$ km/s) (Kolatt et al. 1995).

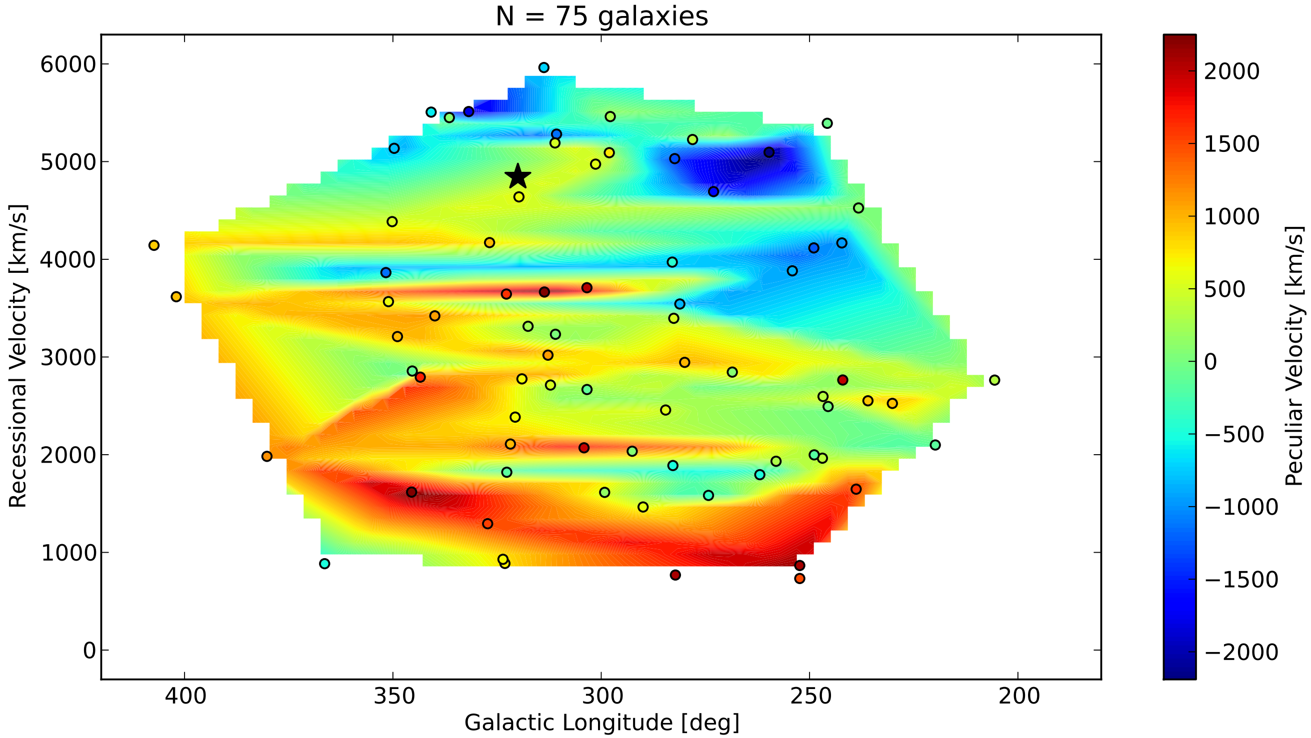

Figure 4.13: Peculiar velocity map of 75 galaxies with recessional velocity $\leq$ 6000 [km/s] obtained by interpolating the peculiar velocities across the Galactic longitude and recessional velocity. All galaxies with $\log W > 1.8$ and $b/a < 0.5$ are used here. Individual galaxies are colour-coded by their predicted peculiar velocities in (km/s). The center of the GA is plotted as a large black star at $(l, b, v) = (320°, 0°, 4500$ km/s) (Kolatt et al. 1995).

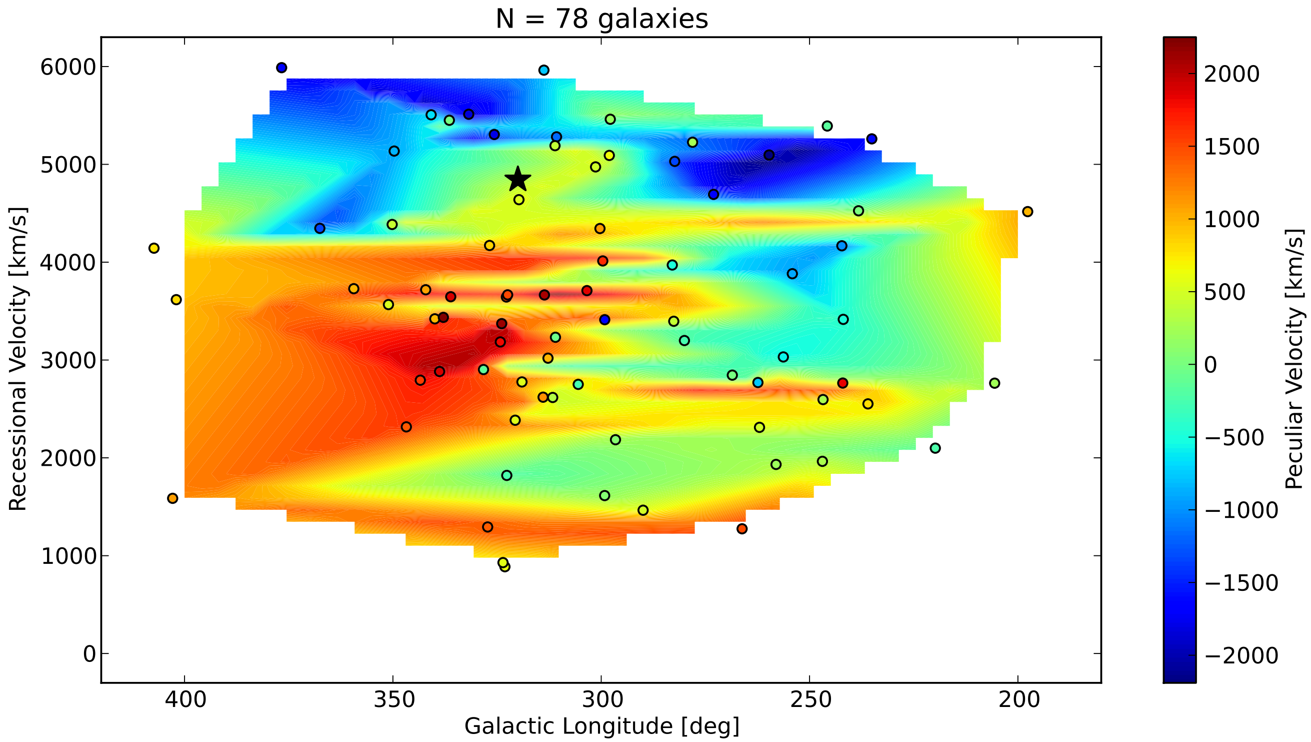

Figure 4.14: Peculiar velocity map of 78 galaxies with recessional velocity ≤ 6000 [km/s] obtained by interpolating the peculiar velocities across the Galactic longitude and recessional velocity. All galaxies with $\log W > 2.3$ are used here. Individual galaxies are colour-coded by their predicted peculiar velocities in (km/s). The center of the GA is plotted as a large black star at $(l, b, v) = (320°, 0°, 4500$ km/s) (Kolatt et al. 1995).

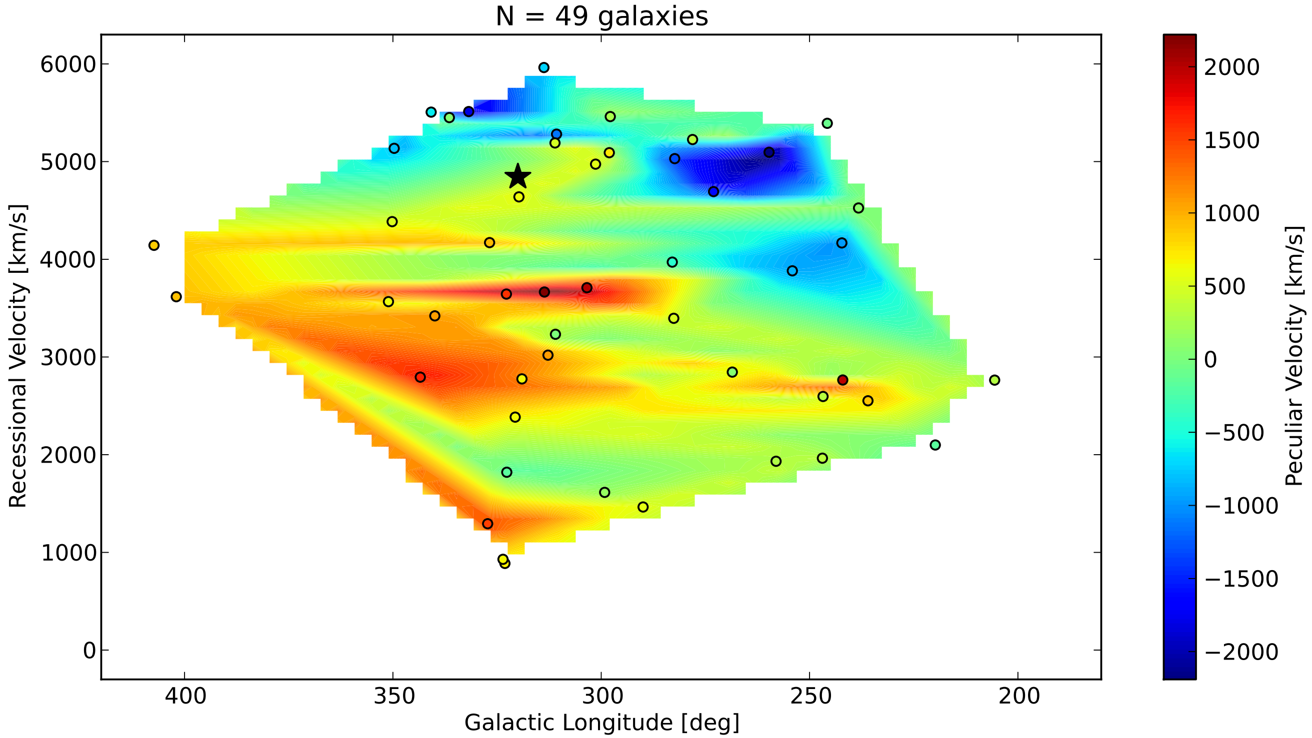

Figure 4.15: Peculiar velocity map of 49 galaxies with recessional velocity ≤ 6000 [km/s] obtained by interpolating the peculiar velocities across the Galactic longitude and recessional velocity. All galaxies with $\log W > 2.3$ and $b/a < 0.5$ are used here. Individual galaxies are colour-coded by their predicted peculiar velocities in (km/s). The center of the GA is plotted as a large black star at $(l, b, v) = (320°, 0°, 4500$ km/s) (Kolatt et al. 1995).

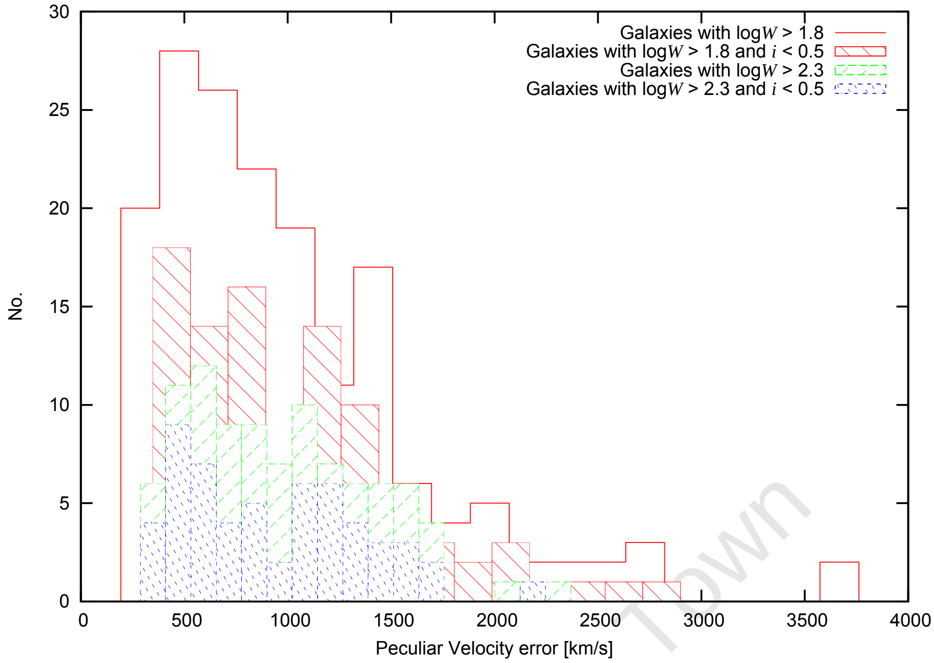

Figure 4.16: Distribution of the errors on peculiar velocities. The unfilled histogram shows errors on peculiar velocities of galaxies with $\log W > 1.8$. The red shaded histogram represents galaxies with $\log W > 1.8$ and $i < 0.5$. The green shaded histogram shows galaxies with $\log W > 2.3$. The blue shaded histogram shows galaxies with $\log W > 2.3$ and $b/a < 0.5$.

For a first interpretation of the resulting data, I compare the derived peculiar velocities with a GA model proposed by Faber & Burstein (1988). The model describes the influence of the GA as $v_{pec,A} = v_A(r_A/d_A)[(d_A^2 + c_A^2)/(r_A^2 + c_A^2)]^{(n_A+1)/2}$, where v_{pec} is the predicted peculiar velocity, r_A is the distance of a galaxy from the infall center, d_A is the distance of the infall center from the Local Group, v_A is the peculiar velocity generated by the GA at the position of the LG, and c_A is the core radius of the center of the GA. We adopted the values of parameters given in Burstein (1990), $n_A = 1.7$, $v_A = 535$ km/s and $c_A = 1430$ km/s. For d_A we used 4844 km/s, following Woudt, Kraan-Korteweg, & Fairall (1999). To compare the single GA model to our data, I restricted the sample to the most accurate subsample using only the galaxies with $\log W > 2.3$ and $b/a < 0.5$ in the Great Attractor region ($290° < l < 350°$; $|b| \leq 5°$). Figure 4.17 depicts the data with the GA model. The shaded area represents our observational limit of $v_{obs} \leq 6000$ km/s. While the errors of the peculiar velocities increase with distance (as expected), the peculiar velocities seem to follow the shape of the early GA model quite well (although no quantitative analysis has been done as yet). In the near future, this kind of analysis can be also used to fit for both the position and mass of superclusters such as the GA.

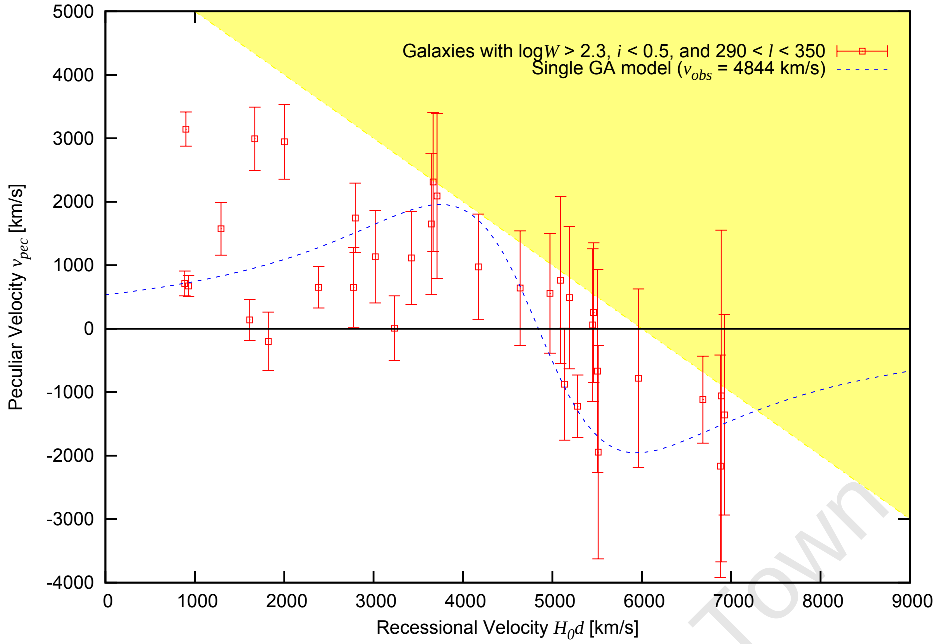

Figure 4.17: Peculiar velocity as a function of recessional velocity for a subsample of galaxies with $\log W > 2.3$, $b/a < 0.5$ in the GA region $290° < l < 350°$. The dashed curve presents the GA model.

4.6 Conclusion

In this Chapter I applied the calibrated NIR Tully – Fisher relation for isophotal magnitude (derived in Chapter 2) to derive distances and peculiar velocities for a subsample of galaxies in the southern ZoA. I have shown that a peculiar velocity analysis in the ZoA is feasible if an "isophotal" (NIR J, H, K_s-bands) TF relation is applied. A recipe on how to derive peculiar velocities for field galaxies in the ZoA has been discussed in detail. This "isophotal" TF relation and the new data provide a powerful tool to trace the matter distribution in the ZoA. Our preliminary data with $v_{hel} \leq 6000$ km/s shows clear infall into the GA. The backside infall cannot be quantified with the existing data set. The data set has since been extended to include all the HI galaxies in the southern ZoA within $v_{obs} \leq 9000$ km/s. This will enable us to test muti-attractor models, such as Great Attractor plus the Shapley Concentration. Combining our data with that from 2MTF will lead to a complete all-sky peculiar velocity survey.

Chapter 5

Conclusion

5.1 Summary of conclusions

In this thesis I present the recalibration of the TF relation using isophotal magnitudes of a sample of 888 galaxies in the NIR J, H, and K_s-bands. This calibration sample is the same as the one used for the 2MTF project based on total magnitudes. No significant change in the isophotal TF relation scatter was found, compared to the scatter in the total TF relation, because the calibration sample is not affected by the dust of the Milky Way. However, this does not hold for low surface brightness galaxies or galaxies obscured by dust.

As shown in Chapter 2, the advantage of the isophotal TF relation is twofold, particularly in the ZoA galaxies: first, it reduces the scatter of the derived peculiar velocity by about 20% in the K_s-band. Secondly the offset in the peculiar velocity derived from the "total" TF relation mostly disappears when the isophotal TF relation is applied (see also Chapter 4). The low scatter and reasonable peculiar velocity values show the high feasibility of peculiar velocity and flow field analysis in the ZoA.

Because the galaxy axial ratio is an important parameter in the TF relation relation, the effect of foreground dust extinction on the shape of galaxies has been discussed. I studied this effect through three different methods. The first method is based on a sample of 54 spiral galaxies derived from the 2MASS (LGA), the second method is based on a sample of simulated galaxies using IRAF and the last method is based on a sample of 82 galaxies observed from deep and shallow surveys. The three independent methods find that, galaxies appear rounder with increasing levels of obscuration. The effect of dust is stronger for highly-inclined galaxies than for less-inclined galaxies. Preliminary models to correct for this effect in the J, H, and K_s-bands have been discussed. These correction models have been tested and show the ability to reproduce the intrinsic axial ratio from the observed value up to extinction level of $A_J = 3$ mag.

Preliminary peculiar velocities of 178 spirals in the southern ZoA are derived in Chapter 4 using the newly calibrated isophotal TF relation, and are compared to total TF values for the same sample. Considerable improvement of the scatter and the systematic offset of the derived peculiar velocities in the ZoA is achieved when the "isophotal" TF relation is applied. The new calibrated relation combined with the HI and NIR data open new possibilities to trace the matter distribution in the ZoA. After excluding the small and less-inclined galaxies from the southern ZoA sample, 120 galaxies are used to construct a preliminary flow field map in the southern ZoA. The preliminary result shows infall from both sides into the Puppis region ($l \sim 240°$) at about 3000 km/s. Another clear infall into the GA and a suggestion of backside infall can be seen. The backside infall into the GA cannot be quantified with the existing data set, which is limited to $v_{hel} \leq 6000$ km/s.

5.2 Future work

The success of this pilot project shows the feasibility of extending peculiar velocity surveys into the ZoA. The isophotal NIR TF relation derived in this thesis, has various cosmological applications in the ZoA. In the following I suggest a few steps for future work.

The selection of galaxies with $v_{obs} \leq 6000$ km/s limits our ability to quantify the backside infall toward the GA, as well as the overall flow towards the much more remote Shapley Concentration (SC). The data set has therefore been extended to include all the HIZoA galaxies within $v_{obs} \leq 9000$ km/s. This will enable us to test muti-attractor models, such as the Great Attractor plus the Shapley Concentration and maybe fit both the position and mass of those superclusters. We also aim to expand our peculiar velocity survey to include galaxies in the northern ZoA. This will provide a peculiar velocity coverage over the full 360°-circle of the ZOA. Combining our data with that from 2MTF can provide a much more complete all-sky peculiar velocity survey.

In the near future, surveys like the Widefield ASKAP L-band Legacy All-sky Blind surveY (WALLABY), which is the ASKAP HI all-sky survey, will dramatically improve the situation. WALLABY aims to cover 75% of the sky ($-90° < \delta < +30°$) and measure the HI properties of $\sim 500,000$ galaxies (Koribalski & López-Sánchez 2009). The mean redshift of the WALLABY survey ~ 0.05 (Duffy et al. 2012) is ideal for peculiar velocity surveys to minimize the error in the measured distances.

A larger sample of galaxies will be used to accurately construct a global correction model to correct for the effect of dust on the shape of spirals. The inclination correction can also be extended by using statistical analysis. A large number of galaxies can be used to statistically quantify the effect of dust on the number of galaxies used in the peculiar velocity surveys.

Bibliography

Aaronson, M., Huchra, J., & Mould, J. 1979, ApJ , 229, 1

Aaronson, M. & Mould, J. 1983, ApJ , 265, 1

Arce, H. G. & Goodman, A. A. 1999, ApJL , 512, L135

Balkowski, C., Bottinelli, L., Chamaraux, P., Gouguenheim, L., & Heidmann, J. 1974, A&A, 34, 43

Balkowski, C. & Kraan-Korteweg, R. C., eds. 1994, Astronomical Society of the Pacific Conference Series, Vol. 67, Unveiling large-scale structures behind the Milky Way

Barnes, D. G., Staveley-Smith, L., de Blok, W. J. G., Oosterloo, T., Stewart, I. M., Wright, A. E., Banks, G. D., Bhathal, R., Boyce, P. J., Calabretta, M. R., Disney, M. J., Drinkwater, M. J., Ekers, R. D., Freeman, K. C., Gibson, B. K., Green, A. J., Haynes, R. F., te Lintel Hekkert, P., Henning, P. A., Jerjen, H., Juraszek, S., Kesteven, M. J., Kilborn, V. A., Knezek, P. M., Koribalski, B., Kraan-Korteweg, R. C., Malin, D. F., Marquarding, M., Minchin, R. F., Mould, J. R., Price, R. M., Putman, M. E., Ryder, S. D., Sadler, E. M., Schröder, A., Stootman, F., Webster, R. L., Wilson, W. E., & Ye, T. 2001, MNRAS , 322, 486

Bilicki, M. 2012, ArXiv e-prints

Bilicki, M., Chodorowski, M., Jarrett, T., & Mamon, G. A. 2011, ApJ , 741, 31

Bilicki, M. & Chodorowski, M. J. 2010, MNRAS , 406, 1358

Bottinelli, L., Gouguenheim, L., Paturel, G., & Teerikorpi, P. 1986, A&A, 156, 157

Bouché, N. & Schneider, S. E. 2000, in Astronomical Society of the Pacific Conference Series, Vol. 218, Mapping the Hidden Universe: The Universe behind the Mily Way - The Universe in HI, ed. R. C. Kraan-Korteweg, P. A. Henning, & H. Andernach, 111

Burstein, D. 1990, Reports on Progress in Physics, 53, 421

Burstein, D., Haynes, M. P., & Faber, M. 1991, Nature , 353, 515

Burstein, D. & Heiles, C. 1982, AJ , 87, 1165

Cambrésy, L., Jarrett, T. H., & Beichman, C. A. 2005, A&A, 435, 131

Cameron, L. M. 1990, A&A, 233, 16

Cardelli, J. A., Clayton, G. C., & Mathis, J. S. 1989, ApJ , 345, 245

Catinella, B., Haynes, M. P., & Giovanelli, R. 2005, AJ , 130, 1037

Charlier, C. V. L. 1922, Arkiv för Mat. Astron. Fys. 16, 1

Courteau, S. 1993, in Astronomical Society of the Pacific Conference Series, Vol. 51, Observational Cosmology, ed. G. L. Chincarini, A. Iovino, T. Maccacaro, & D. Maccagni, 165

Courteau, S., Faber, S. M., Dressler, A., & Willick, J. A. 1993, ApJL , 412, L51

Courtois, H. M. & Tully, R. B. 2012, Astronomische Nachrichten, 333, 436

da Costa, L. N., Freudling, W., Wegner, G., Giovanelli, R., Haynes, M. P., & Salzer, J. J. 1996, ApJL , 468, L5

dell'Antonio, I. P., Geller, M. J., & Bothun, G. D. 1996, AJ , 112, 1780

Djorgovski, S. & Davis, M. 1987, ApJ , 313, 59

Donley, J. L., Staveley-Smith, L., Kraan-Korteweg, R. C., Islas-Islas, J. M., Schröder, A., Henning, P. A., Koribalski, B., Mader, S., & Stewart, I. 2005, AJ , 129, 220

Dressler, A. 1987, ApJ , 317, 1

Dreyer, J. L. E. 1888, MmRAS, 49, 1

Driver, S. P., Popescu, C. C., Tuffs, R. J., Liske, J., Graham, A. W., Allen, P. D., & de Propris, R. 2007, MNRAS , 379, 1022

Duffy, A. R., Kay, S. T., Battye, R. A., Booth, C. M., Dalla Vecchia, C., & Schaye, J. 2012, MNRAS , 420, 2799

Epchtein, N. 1997, in Astrophysics and Space Science Library, Vol. 210, The Impact of Large Scale Near-IR Sky Surveys, ed. F. Garzon, N. Epchtein, A. Omont, B. Burton, & P. Persi, 15

Epchtein, N. 1998, in Astrophysics and Space Science Library, Vol. 230, The Impact of Near-Infrared Sky Surveys on Galactic and Extragalactic Astronomy, ed. N. Epchtein, 3

Erdoˇgdu,P., Huchra, J. P., Lahav, O., Colless, M., Cutri, R. M., Falco, E., George, T., Jarrett, T., Jones, D. H., Kochanek, C. S., Macri, L., Mader, J., Martimbeau, N., Pahre, M., Parker, Q., Rassat, A., & Saunders, W. 2006a, MNRAS , 368, 1515

Erdoğdu, P., Lahav, O., Huchra, J. P., Colless, M., Cutri, R. M., Falco, E., George, T., Jarrett, T., Jones, D. H., Macri, L. M., Mader, J., Martimbeau, N., Pahre, M. A., Parker, Q. A., Rassat, A., & Saunders, W. 2006b, MNRAS , 373, 45

Faber, S. M. & Burstein, D. 1988, Motions of galaxies in the neighborhood of the local group, ed. V. C. Rubin & G. V. Coyne, 115–167

Faber, S. M. & Jackson, R. E. 1976, ApJ , 204, 668

Fairall, A. P., ed. 1998, Large-scale structures in the universe

Fairall, A. P. & Woudt, P. A., eds. 2005, Astronomical Society of the Pacific Conference Series, Vol. 329, Nearby Large-Scale Structures and the Zone of Avoidance

Fixsen, D. J., Cheng, E. S., Gales, J. M., Mather, J. C., Shafer, R. A., & Wright, E. L. 1996, ApJ , 473, 576

Fouque, P. & Paturel, G. 1983, A&AS, 53, 351

—. 1985, A&A, 150, 192

Freedman, W. L. 1990, ApJL , 355, L35

Freudling, W., da Costa, L. N., Wegner, G., Giovanelli, R., Haynes, M. P., & Salzer, J. J. 1995, AJ , 110, 920

Giovanelli, R., Haynes, M. P., Freudling, W., da Costa, L. N., Salzer, J. J., & Wegner, G. 1998, ApJL , 505, L91

Giovanelli, R., Haynes, M. P., Herter, T., Vogt, N. P., da Costa, L. N., Freudling, W., Salzer, J. J., & Wegner, G. 1997a, AJ , 113, 53

Giovanelli, R., Haynes, M. P., Herter, T., Vogt, N. P., Wegner, G., Salzer, J. J., da Costa, L. N., & Freudling, W. 1997b, AJ , 113, 22

Giovanelli, R., Haynes, M. P., Salzer, J. J., Wegner, G., da Costa, L. N., & Freudling, W. 1994, AJ , 107, 2036

Han, M. 1992a, ApJ , 391, 617

—. 1992b, ApJ , 395, 75

Henning, P. A., Kraan-Korteweg, R. C., & Staveley-Smith, L. 2005, in Astronomical Society of the Pacific Conference Series, Vol. 329, Nearby Large-Scale Structures and the Zone of Avoidance, ed. A. P. Fairall & P. A. Woudt, 199

Henning, P. A., Springob, C. M., Day, F., Minchin, R., Momjian, E., Catinella, B., Muller, E., Koribalski, B., Masters, K., Pantoja, C., Putman, M., Rosenberg, J. L., Schneider, S., & Staveley-Smith, L. 2008, in American Institute of Physics Conference Series, Vol. 1035, The Evolution of Galaxies Through the Neutral Hydrogen Window, ed. R. Minchin & E. Momjian, 246–248

Henning, P. A., Springob, C. M., Minchin, R. F., Momjian, E., Catinella, B., McIntyre, T., Day, F., Muller, E., Koribalski, B., Rosenberg, J. L., Schneider, S., Staveley-Smith, L., & van Driel, W. 2010, AJ , 139, 2130

Henning, P. A., Staveley-Smith, L., Ekers, R. D., Green, A. J., Haynes, R. F., Juraszek, S., Kesteven, M. J., Koribalski, B., Kraan-Korteweg, R. C., Price, R. M., Sadler, E. M., & Schröder, A. 2000, AJ , 119, 2686

Herschel, J. 1864, Philosophical Transactions

Holmberg, E. 1958, Meddelanden fran Lunds Astronomiska Observatorium Serie II, 136, 1

Holwerda, B. W., Keel, W. C., Williams, B., Dalcanton, J. J., & de Jong, R. S. 2009, AJ , 137, 3000

Hong, T., Staveley-Smith, L., Masters, K., Springob, C., Macri, L., Koribalski, B., Jones, H., & Jarrett, T. 2013a, in IAU Symposium, Vol. 289, IAU Symposium, ed. R. de Grijs, 312–315

Hong, T., Staveley-Smith, L., Masters, K. L., Springob, C. M., Macri, L. M., Koribalski, B. S., Jones, D. H., Jarrett, T. H., & Crook, A. C. 2013b, MNRAS , 432, 1178

Hubble, E. P. 1925, ApJ , 62, 409

—. 1929, ApJ , 69, 103

—. 1936, Realm of the Nebulae

Huchra, J., Jarrett, T., Skrutskie, M., Cutri, R., Schneider, S., Macri, L., Steining, R., Mader, J., Martimbeau, N., & George, T. 2005, in Astronomical Society of the Pacific Conference Series, Vol. 329, Nearby Large-Scale Structures and the Zone of Avoidance, ed. A. P. Fairall & P. A. Woudt, 135

Huchra, J. P., Macri, L. M., Masters, K. L., Jarrett, T. H., Berlind, P., Calkins, M., Crook, A. C., Cutri, R., Erdoˇgdu, P., Falco, E., George, T., Hutcheson, C. M., Lahav, O., Mader, J., Mink, J. D., Martimbeau, N., Schneider, S., Skrutskie, M., Tokarz, S., & Westover, M. 2012, ApJS , 199, 26

Hudson, M. J. & Lynden-Bell, D. 1991, MNRAS , 252, 219

Jarrett, T. 2004, PASA , 21, 396

Jarrett, T. H., Chester, T., Cutri, R., Schneider, S., Skrutskie, M., & Huchra, J. P. 2000, AJ , 119, 2498

Jarrett, T. H., Chester, T., Cutri, R., Schneider, S. E., & Huchra, J. P. 2003, AJ , 125, 525

Karachentsev, I. D., Mitronova, S. N., Karachentseva, V. E., Kudrya, Y. N., & Jarrett, T. H. 2002, A&A, 396, 431

Kerp, J., Winkel, B., Ben Bekhti, N., Flöer, L., & Kalberla, P. M. W. 2011, Astronomische Nachrichten, 332, 637

Kogut, A., Lineweaver, C., Smoot, G. F., Bennett, C. L., Banday, A., Boggess, N. W., Cheng, E. S., de Amici, G., Fixsen, D. J., Hinshaw, G., Jackson, P. D., Janssen, M., Keegstra, P., Loewenstein, K., Lubin, P., Mather, J. C., Tenorio, L., Weiss, R., Wilkinson, D. T., & Wright, E. L. 1993, ApJ , 419, 1

Kolatt, T., Dekel, A., & Lahav, O. 1995, MNRAS , 275, 797

Koribalski, B. S. & López-Sánchez, Á. R. 2009, MNRAS , 400, 1749

Koribalski, B. S., Staveley-Smith, L., Kilborn, V. A., Ryder, S. D., Kraan-Korteweg, R. C., Ryan-Weber, E. V., Ekers, R. D., Jerjen, H., Henning, P. A., Putman, M. E., Zwaan, M. A., de Blok, W. J. G., Calabretta, M. R., Disney, M. J., Minchin, R. F., Bhathal, R., Boyce, P. J., Drinkwater, M. J., Freeman, K. C., Gibson, B. K., Green, A. J., Haynes, R. F., Juraszek, S., Kesteven, M. J., Knezek, P. M., Mader, S., Marquarding, M., Meyer, M., Mould, J. R., Oosterloo, T., O'Brien, J., Price, R. M., Sadler, E. M., Schröder, A., Stewart, I. M., Stootman, F., Waugh, M., Warren, B. E., Webster, R. L., & Wright, A. E. 2004, AJ , 128, 16

Kraan-Korteweg, R. C. 2005, in Reviews in Modern Astronomy, Vol. 18, Reviews in Modern Astronomy, ed. S. Röser, 48–75

Kraan-Korteweg, R. C., Cameron, L., & Tammann, G. A. 1986, in NATO ASIC Proc. 180: Galaxy Distances and Deviations from Universal Expansion, ed. B. F. Madore & R. B. Tully, 65–72

Kraan-Korteweg, R. C., Cameron, L. M., & Tammann, G. A. 1988, ApJ , 331, 620

Kraan-Korteweg, R. C., Henning, P. A., & Andernach, H., eds. 2000, Astronomical Society of the Pacific Conference Series, Vol. 218, Mapping the Hidden Universe: The Universe behind the Milky Way - The Universe in HI

Kraan-Korteweg, R. C., Henning, P. A., & Schröder, A. C. 2002, A&A, 391, 887

Kraan-Korteweg, R. C. & Jarrett, T. 2005, in Astronomical Society of the Pacific Conference Series, Vol. 329, Nearby Large-Scale Structures and the Zone of Avoidance, ed. A. P. Fairall & P. A. Woudt, 119

Kraan-Korteweg, R. C. & Lahav, O. 2000, A&A Rev., 10, 211

Kraan-Korteweg, R. C., Shafi, N., Koribalski, B. S., Staveley-Smith, L., Buckland, P., Henning, P. A., & Fairall, A. P. 2008, Outlining the Local Void with the Parkes HI ZOA and Galactic Bulge Surveys, ed. B. S. Koribalski & H. Jerjen, 13

Kraan-Korteweg, R. C., Staveley-Smith, L., Donley, J., Koribalski, B., & Henning, P. A. 2005, in IAU Symposium, Vol. 216, Maps of the Cosmos, ed. M. Colless, L. Staveley-Smith, & R. A. Stathakis, 203

Kraan-Korteweg, R. C., Woudt, P. A., Cayatte, V., Fairall, A. P., Balkowski, C., & Henning, P. A. 1996, Nature , 379, 519

Lagattuta, D. J., Mould, J. R., Staveley-Smith, L., Hong, T., Springob, C. M., Masters, K. L., Koribalski, B. S., & Jones, D. H. 2013, ApJ , 771, 88

Lahav, O. 1994, in Astronomical Society of the Pacific Conference Series, Vol. 67, Unveiling Large-Scale Structures Behind the Milky Way, ed. C. Balkowski & R. C. Kraan-Korteweg, 7

Lahav, O., Fisher, K. B., Hoffman, Y., Scharf, C. A., & Zaroubi, S. 1994, ApJL , 423, L93

Loeb, A. & Narayan, R. 2008, MNRAS , 386, 2221

Macri, L. M. 2001, PhD thesis, Harvard University

Majewski, S. R., Zasowski, G., & Nidever, D. L. 2011, ApJ , 739, 25

Malhotra, S., Spergel, D. N., Rhoads, J. E., & Li, J. 1996, ApJ , 473, 687

Masters, K. L. 2005, PhD thesis, Cornell University, New York, USA

Masters, K. L. 2008, in Astronomical Society of the Pacific Conference Series, Vol. 395, Frontiers of Astrophysics: A Celebration of NRAO's 50th Anniversary, ed. A. H. Bridle, J. J. Condon, & G. C. Hunt, 137

Masters, K. L., Giovanelli, R., & Haynes, M. P. 2003, AJ , 126, 158

Masters, K. L., Nichol, R., Bamford, S., Mosleh, M., Lintott, C. J., Andreescu, D., Edmondson, E. M., Keel, W. C., Murray, P., Raddick, M. J., Schawinski, K., Slosar, A., Szalay, A. S., Thomas, D., & Vandenberg, J. 2010, MNRAS , 404, 792

Masters, K. L., Springob, C. M., Haynes, M. P., & Giovanelli, R. 2006, ApJ , 653, 861

Masters, K. L., Springob, C. M., & Huchra, J. P. 2008, AJ , 135, 1738

Meyer, M. J., Zwaan, M. A., Webster, R. L., Staveley-Smith, L., Ryan-Weber, E., Drinkwater, M. J., Barnes, D. G., Howlett, M., Kilborn, V. A., Stevens, J., Waugh, M., Pierce, M. J., Bhathal, R., de Blok, W. J. G., Disney, M. J., Ekers, R. D., Freeman, K. C., Garcia, D. A., Gibson, B. K., Harnett, J., Henning, P. A., Jerjen, H., Kesteven, M. J., Knezek, P. M., Koribalski, B. S., Mader, S., Marquarding, M., Minchin, R. F., O'Brien, J., Oosterloo, T., Price, R. M., Putman, M. E., Ryder, S. D., Sadler, E. M., Stewart, I. M., Stootman, F., & Wright, A. E. 2004, MNRAS , 350, 1195

Mould, J. R., Akeson, R. L., Bothun, G. D., Han, M., Huchra, J. P., Roth, J., & Schommer, R. A. 1993, ApJ , 409, 14

Nagayama, T., Woudt, P. A., Nagashima, C., Nakajima, Y., Kato, D., Kurita, M., Nagata, T., Nakaya, H., Tamura, M., Sugitani, K., Wakamatsu, K., & Sato, S. 2004, MNRAS , 354, 980

Nidever, D. L., Zasowski, G., & Majewski, S. R. 2012, ApJS , 201, 35

Park, C.-G. & Park, C. 2006, ApJ , 637, 1

Pastrav, B. A., Popescu, C. C., Tuffs, R. J., & Sansom, A. E. 2013a, A&A, 553, A80

—. 2013b, ArXiv e-prints

Paturel, G., Fouque, P., Lauberts, A., Valentijn, E. A., Corwin, H. G., & de Vaucouleurs, G. 1987, A&A, 184, 86

Peletier, R. F. & Willner, S. P. 1991, ApJ , 382, 382

—. 1993, ApJ , 418, 626

Pierce, M. J. & Tully, R. B. 1988, ApJ , 330, 579

—. 1992, ApJ , 387, 47

Pizagno, J., Prada, F., Weinberg, D. H., Rix, H.-W., Pogge, R. W., Grebel, E. K., Harbeck, D., Blanton, M., Brinkmann, J., & Gunn, J. E. 2007, AJ , 134, 945

Poggianti, B. M. 1997, A&AS, 122, 399

Proctor, R. 1878, The Universe of Stars, Longmans, Green and Co., London, 41

Ramatsoku, M. 2012, MSc thesis, University of Cape Town

Riad, I. F., Kraan-Korteweg, R. C., & Woudt, P. A. 2010, MNRAS , 401, 924

Rothberg, B., Saunders, W., Tully, R. B., & Witchalls, P. L. 2000, ApJ , 533, 781

Sakai, S., Mould, J. R., Huchra, J. P., Hughes, S., Macri, L. M., & Kennicutt, Jr., R. C. 2000, in Astronomical Society of the Pacific Conference Series, Vol. 201, Cosmic Flows Workshop, ed. S. Courteau & J. Willick, 129

Schlegel, D. J., Finkbeiner, D. P., & Davis, M. 1998, ApJ , 500, 525

Schröder, A. C., Kraan-Korteweg, R. C., & Henning, P. A. 2009, A&A, 505, 1049

Schröder, A. C., Kraan-Korteweg, R. C., Mamon, G. A., & Woudt, P. A. 2005, in Astronomical Society of the Pacific Conference Series, Vol. 329, Nearby Large-Scale Structures and the Zone of Avoidance, ed. A. P. Fairall & P. A. Woudt, 167

Schröder, A. C., Mamon, G. A., Kraan-Korteweg, R. C., & Woudt, P. A. 2007, A&A, 466, 481

Shafi, N. 2008, MSc thesis, University of Cape Town

Shapley, H. 1961, Galaxies.

Shapley, H. & Curtis, H. D. 1921, Bulletin of the National Research Council, Vol. 2, Part 3, No. 11, p. 171-217, 2, 171

Skrutskie, M. F., Cutri, R. M., Stiening, R., Weinberg, M. D., Schneider, S., Carpenter, J. M., Beichman, C., Capps, R., Chester, T., Elias, J., Huchra, J., Liebert, J., Lonsdale, C., Monet, D. G., Price, S., Seitzer, P., Jarrett, T., Kirkpatrick, J. D., Gizis, J. E., Howard, E., Evans, T., Fowler, J., Fullmer, L., Hurt, R., Light, R., Kopan, E. L., Marsh, K. A., McCallon, H. L., Tam, R., Van Dyk, S., & Wheelock, S. 2006, AJ , 131, 1163

Sorce, J. G., Courtois, H. M., Tully, R. B., Seibert, M., Scowcroft, V., Freedman, W. L., Madore, B. F., Persson, S. E., Monson, A., & Rigby, J. 2013, ApJ , 765, 94

Springob, C. M., Haynes, M. P., Giovanelli, R., & Kent, B. R. 2005, ApJS , 160, 149

Springob, C. M., Masters, K. L., Haynes, M. P., Giovanelli, R., & Marinoni, C. 2007, ApJS , 172, 599

Theureau, G., Rauzy, S., Bottinelli, L., & Gouguenheim, L. 1998, A&A, 340, 21

Trumpler, R. J. 1930, PASP , 42, 214

Tuffs, R. J., Popescu, C. C., Völk, H. J., Kylafis, N. D., & Dopita, M. A. 2004, A&A, 419, 821

Tully, R. B. & Fisher, J. R. 1977, A&A, 54, 661

Tully, R. B. & Pierce, M. J. 2000, ApJ , 533, 744

Tully, R. B., Pierce, M. J., Huang, J.-S., Saunders, W., Verheijen, M. A. W., & Witchalls, P. L. 1998, AJ , 115, 2264

Tully, R. B., Shaya, E. J., Karachentsev, I. D., Courtois, H. M., Kocevski, D. D., Rizzi, L., & Peel, A. 2008, ApJ , 676, 184

Valentijn, E. A. 1990, Nature , 346, 153

van Driel, W., Schneider, S. E., Kraan-Korteweg, R. C., & Monnier Ragaigne, D. 2009, A&A, 505, 29

Williams, W. L. 2011, MSc thesis, University of Cape Town

Williams, W. L., Woudt, P. A., & Kraan-Korteweg, R. C. 2011, Ten years of Infrared Survey Facility and the Future, eds. T. Nagayama, S. Sato, and K. Wakamatsu, 98 (arXiv:1107.1096)

Willick, J. A., Courteau, S., Faber, S. M., Burstein, D., & Dekel, A. 1995, ApJ , 446, 12

Willick, J. A., Courteau, S., Faber, S. M., Burstein, D., Dekel, A., & Kolatt, T. 1996, ApJ , 457, 460

Woudt, P. A. 1998, PhD thesis, , Univ. of Cape Town, South Africa, (1998)

Woudt, P. A., Kraan-Korteweg, R. C., & Fairall, A. P. 1999, A&A, 352, 39

York, D. G., Adelman, J., Anderson, Jr., J. E., Anderson, S. F., Annis, J., Bahcall, N. A., Bakken, J. A., Barkhouser, R., Bastian, S., Berman, E., Boroski, W. N., Bracker, S., Briegel, C., Briggs, J. W., Brinkmann, J., Brunner, R., Burles, S., Carey, L., Carr, M. A., Castander, F. J., Chen, B., Colestock, P. L., Connolly, A. J., Crocker, J. H., Csabai, I., Czarapata, P. C., Davis, J. E., Doi, M., Dombeck, T., Eisenstein, D., Ellman, N., Elms, B. R., Evans, M. L., Fan, X., Federwitz, G. R., Fiscelli, L., Friedman, S., Frieman, J. A., Fukugita, M., Gillespie, B., Gunn, J. E., Gurbani, V. K., de Haas, E., Haldeman, M., Harris, F. H., Hayes, J., Heckman, T. M., Hennessy, G. S., Hindsley, R. B., Holm, S., Holmgren, D. J., Huang, C.-h., Hull, C., Husby, D., Ichikawa, S.-I., Ichikawa, T., Ivezić, Ž., Kent, S., Kim, R. S. J., Kinney, E., Klaene, M., Kleinman, A. N., Kleinman, S., Knapp, G. R., Korienek, J., Kron, R. G., Kunszt, P. Z., Lamb, D. Q., Lee, B., Leger, R. F., Limmongkol, S., Lindenmeyer, C., Long, D. C., Loomis, C., Loveday, J., Lucinio, R., Lupton, R. H., MacKinnon, B., Mannery, E. J., Mantsch, P. M., Margon, B., McGehee, P., McKay, T. A., Meiksin, A., Merelli, A., Monet, D. G., Munn, J. A., Narayanan, V. K., Nash, T., Neilsen, E., Neswold, R., Newberg, H. J., Nichol, R. C., Nicinski, T., Nonino, M., Okada, N., Okamura, S., Ostriker, J. P., Owen, R., Pauls, A. G., Peoples, J., Peterson, R. L., Petravick, D., Pier, J. R., Pope, A., Pordes, R., Prosapio, A., Rechenmacher, R., Quinn, T. R., Richards, G. T., Richmond, M. W., Rivetta, C. H., Rockosi, C. M., Ruthmansdorfer, K., Sandford, D., Schlegel, D. J., Schneider, D. P., Sekiguchi, M., Sergey, G., Shimasaku, K., Siegmund, W. A., Smee, S., Smith, J. A., Snedden, S., Stone, R., Stoughton, C., Strauss, M. A., Stubbs, C., SubbaRao, M., Szalay, A. S., Szapudi, I., Szokoly, G. P., Thakar, A. R., Tremonti, C., Tucker, D. L., Uomoto, A., Vanden Berk, D., Vogeley, M. S., Waddell, P., Wang, S.-i., Watanabe, M., Weinberg, D. H., Yanny, B., Yasuda, N., & SDSS Collaboration. 2000, AJ , 120, 1579

Zasowski, G., Majewski, S. R., Indebetouw, R., Meade, M. R., Nidever, D. L., Patterson, R. J., Babler, B., Skrutskie, M. F., Watson, C., Whitney, B. A., & Churchwell, E. 2009, ApJ , 707, 510